

Stellingen

behorende bij het proefschrift "Analysis of soil penetration"

P. van den Berg

1. De gradiënt van de conusweerstand ter plaatse van een laagovergang wordt in hoge mate bepaald door de verhouding tussen de stijfheden van beide lagen.

dit proefschrift, paragraaf 4.5

2. Het geldigheidsgebied van de 4D-8D methode om het draagvermogen van palen te berekenen dient nader onderzocht te worden.

dit proefschrift, paragraaf 4.5

3. De kwaliteit van een grondmonster wordt sterk bepaald door de mate van schuifspanningsoverdracht tussen het monster en het steekapparaat. Bij relatief kleine steekhoeken speelt de area-ratio geen grote rol.

dit proefschrift, hoofdstuk 5

4. Om de nauwkeurigheid vast te stellen van de oplossing van een niet-lineaire eindige-elementen analyse is de definitie van het convergentie-criterium even belangrijk als de grootte ervan.

Bijnagte, J.L., van den Berg, P., Havinga, H., "3-dimensional analysis of locally corroded sheet pile walls", XIII ICSMFE, January 1994, New Delhi, India.

5. Op de verdere ontwikkeling en toepassing van ALE-modellen binnen de geotechniek kunnen nog velen afstuderen en promoveren.

6. Het is frustrerend om te zien dat oplossingen die vanuit de wetenschap worden aangedragen pas meer dan een generatie later door de politiek serieus worden genomen.

stelling 1 over ondergronds bouwen, proefschrift "statics and kinematics in the failable zone of a granular material", G. de Josselin de Jong, 1959.

7. Omdat het aantal wetenschappelijke specialisten in Nederland klein is, dient de samenwerking tussen de technologische instituten en de universiteiten te worden bevorderd.
8. Een christen dient in de volle breedte van de maatschappij het beeld van zijn Naamgever te vertonen.
9. Door de moderne communicatiemiddelen zijn we er bijna in geslaagd van de wereld één groot dorp te maken.
10. De sterke gelijkenis tussen snelwegen en open riolen pleit voor ondergrondse aanleg van zowel de kleine als de grote infrastructuur.
11. Fietspaden bestaande uit 30 bij 30 (cm) tegels en gesitueerd naast provinciale wegen dienen ogenblikkelijk verlegd en van een andere bestrating te worden voorzien.
12. Het is geen best teken als een jonge vader veel gezien wordt met een stropdas. Het dragen van dit kledingstuk en het omgaan met kinderen gaan niet samen.
13. Het feit dat iemand aangebrand of van de kook kan zijn wekt de indruk dat de mens veel weg heeft van een aardappel.

TR diss
2406

352305
2186354
TR diss 2406

Analysis of soil penetration

Analysis of soil penetration

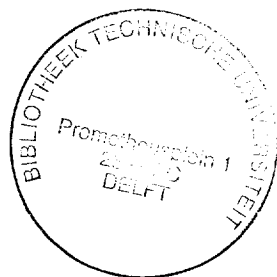
PROEFSCHRIFT

ter verkrijging van de graad van doctor
aan de Technische Universiteit Delft,
op gezag van de Rector Magnificus Prof. ir. K.F. Wakker,
in het openbaar te verdedigen ten overstaan van een commissie,
door het College van Dekanen aangewezen,
op maandag 27 juni 1994 te 16.00 uur

door

Pieter van den BERG

geboren te Gouda,
civiel ingenieur



Dit proefschrift is goedgekeurd door de promotoren:

Prof.dr.ir. A. Verruijt
Prof.dr.ir. R. de Borst

Published and distributed by:

Delft University Press
Stevinweg 1
2628 CN Delft
The Netherlands

Telephone +31 15 783254
Fax +31 15 781661

CIP-DATA KONINKLIJKE BIBLIOTHEEK, DEN HAAG

Berg, Pieter van den

Analysis of soil penetration / Pieter van den Berg. - Delft : Delft University Press. - III.
Thesis Delft University of Technology. - With ref. - With summary in Dutch.
ISBN 90-407-1004-X
NUGI 841
Subject headings: soil penetration

Copyright c 1994 by P. van den Berg

All rights reserved.

No part of the material protected by this copyright notice may be reproduced or utilized in any form or by any means, electronic or mechanical, including photocopying, recording or by any information storage and retrieval system, without permission from the publisher: Delft University Press, Stevinweg 1, 2628 CN Delft, The Netherlands.

Printed in The Netherlands

Acknowledgements

The research reported in this thesis has been carried out at the Strategic Research Department of Delft Geotechnics. I would like to express my sincere gratitude to the Board of Directors of Delft Geotechnics and to prof. Frans Barends, head of my department, who gave me the opportunity to do this work.

I wish to thank my colleagues for their support, in particular dr. Hans Teunissen for the stimulating discussions during the study. I also wish to express my gratitude to Suzanne van Eekelen (sample disturbance) and to André Opstal and Paul Schaminee (experimental work).

The models described in this thesis have been incorporated in the DIEKA finite element program of the Mechanical Department of the University of Twente. The collaboration with the enthusiastic DIEKA group, especially with prof. Han Huétink and Gerrit Rekers, is highly appreciated.

I would also like to acknowledge my promotors, prof. Arnold Verruijt and prof. René de Borst for their stimulating and fruitful discussions.

Large parts of the work were supported financially by the Dutch Ministry of Public Works. I am very much indebted for the regular meetings with Peter van Driel, Jelle de Vries, Ed Troost, Jaap Lindenberg, Henk Bakker and Harry Dekker and for the commission of that contract.

However, without the support of my wife Bertina I would never have come this far. Thank you for your encouragements, patience and reminding me of the world beyond my work.

Contents

1. Introduction	1
2. Penetration models	3
2.1 Introduction	3
2.2 State of the art in modelling penetration	3
2.2.1 Bearing capacity models	3
2.2.2 Cavity expansion models	5
2.2.3 Flow models	6
2.2.4 Finite element models	8
2.3 Evaluation of existing models	11
2.3.1 Penetration mechanism	11
2.3.2 Soil behaviour	11
2.3.3 Layered soil profile	12
2.3.4 In conclusion	12
2.3.5 Example	13
2.4 Scope of the work	15
3. Arbitrary Lagrangean-Eulerean model	17
3.1 Stress and strain at finite deformation	17
3.1.1 Introduction	17
3.1.2 1D truss bar	20
3.1.3 Cauchy stress rate and objectivity	22
3.2 Finite element formulation	25
3.3 Eulerean approach of layered systems	32
3.3.1 Introduction	32
3.3.2 Model	32
3.3.3 Applications	35
3.4 Constitutive behaviour	42
3.4.1 General elasto-plastic framework	42
3.4.2 On the Mohr-Coulomb model	46
3.4.3 Constant volume at enlarged shear strain	53
3.4.4 Contact-frictional interface behaviour	56
3.4.5 Soil as a two-phase medium	58
3.5 Validation of the model	63
3.5.1 Introduction	63
3.5.2 Application to circular footing	63
3.5.3 In conclusion	70
Appendix 3.A: Non-linear elasticity	71
Appendix 3.B: On the critical state of sand	72
Appendix 3.C: Potential field around a circular line-source	74

4. Analysis of cone penetration	77
4.1 Introduction	77
4.2 Numerical model	78
4.2.1 Eulerean approach of penetration process	78
4.2.2 Finite elements	79
4.2.3 Initial stresses and material parameters	79
4.2.4 Validation of the model	80
4.3 Penetration in clay	87
4.3.1 Introduction	87
4.3.2 Numerical analysis	91
4.3.3 Conclusions	95
4.4 Penetration in sand	96
4.4.1 Introduction	96
4.4.2 Numerical analysis	100
4.4.3 Conclusions	120
4.5 Penetration in layered soil	121
4.5.1 Introduction	121
4.5.2 Numerical analysis of layered systems	125
4.5.3 Experiments	131
4.5.4 Conclusions	141
5. Sampling disturbances in soft clay	145
5.1 Introduction	145
5.2 Delft Continuous Sampler	145
5.3 Numerical analysis of sampling process	147
5.4 Experiments	151
5.5 Conclusions	157
References	159
List of symbols	167
Summary	171
Samenvatting	173
Curriculum Vitae	175

1. Introduction

Penetration of a steel cylindrical bar into the subsoil seems to be one of the simplest geotechnical problems. However, the large number of researchers who spent their time on the analysis of this problem shows the opposite. Soil penetration is a complicated mechanical process, since very large local deformations are involved. Soil initially located underneath the tip is pushed away to make room for the cylinder. Another complication is related to the fact that the subsoil is not homogeneous, but consists of layered deposits.

Some 50 years ago, the cone penetration test (CPT) or Dutch cone was developed in the Netherlands. A steel cylindrical bar with a diameter of 36 mm and a cone shaped tip is pushed into the soil at a constant penetration rate of 2 cm per sec. During penetration the tip resistance is measured. Originally, CPT was developed as a direct scale model of a pile, in order to determine the bearing capacity of foundation piles. Nowadays, in many countries this testing method is a widely accepted and useful tool for in-situ site investigation and geotechnical design. For many years, investigators have tried to model the cone penetration process. Their most important intention was to establish a theoretical relation between the cone resistance and stiffness and strength parameters of the soil. Chapter 2 summarizes the basic ideas behind the models as well as their capabilities and limitations. As all of the models described are not sufficiently equipped to model steady state penetration in a layered soil profile accurately, an alternative formulation of the problem is followed.

The numerical model is described in chapter 3. The finite element program DIEKA (University of Twente) is extended in the sense that penetration of rigid devices into frictional material can be simulated as well as penetration into a layered soil profile. Results of the application of the model to CPT in homogeneous clay, homogeneous sand and layered media are given in chapter 4. Model tests have been performed in the laboratory under controlled conditions in order to validate the results of the numerical model. Chapter 5 presents the outcome of a numerical and experimental study towards sampling disturbances in clay.

2. Penetration models

2.1 Introduction

Frequently, engineers working in geotechnical practice get measured CPT data as cone resistance (q_c), skin friction (f_s) and pore water pressure (u) and need mechanical soil parameters such as Young's modulus (E), undrained cohesion (c_u) and friction angle (ϕ) to be used for their deformation and stability analyses. Therefore, a large number of investigators introduced a considerable number of different models. Generally speaking, the existing models can be subdivided into four categories: those based on bearing capacity theory, those based on cavity expansion theory, models based on a flow approach and numerical models based on finite element theory. This chapter summarizes the basic ideas behind the models as well as their capabilities and limitations.

Furthermore, a large number of empirical approaches exist, in which correlations are proposed which relate the cone resistance to the relative density, for instance, or the deformation characteristics of the soil. By definition empirical approaches lack a sound theoretical background. For an extensive survey of correlations the reader is referred to Sanglerat (1972) or Baligh (1975).

2.2 State of the art in modelling penetration

2.2.1 Bearing capacity models

The bearing capacity theory is based on the original work by Prandtl (1921). In this approach, also referred to as the stress characteristics method, the cone penetration problem is considered as an incipient failure of a rigid plastic material. Assuming a specific failure mode, a plastic collapse calculation is performed and the resulting vertical pressure is identified as the bearing capacity. The solutions of Prandtl were first applied to deep foundations under plane strain conditions by Caquot (1934) and Buisman (1935). After them a large number of investigators obtained different solutions for the bearing capacity of deep foundations depending on the assumed shape and location of the failure zone. Well-known solutions for axi-symmetric conditions are those published by Meyerhoff (1951, 1961) and Cox et al. (1961). Failure patterns according to a large number of solutions have been investigated by Vesic (1967) and are presented in figure 2.1.

According to Caquot (1934), Buisman (1935) and others, the ultimate bearing capacity of deep foundations $p(z)$ can be presented in the following general form:

$$p(z) = s_c c N_c + s_q \sigma_{v,0}(z) N_q + s_\gamma \left(\frac{1}{2} \gamma B\right) N_\gamma \quad (2.1)$$

where:

- c cohesion
- $\sigma_{v,0}(z)$ initial vertical stress at depth z ($= \gamma z$)
- γ volumetric weight of soil
- z depth
- B width of foundation (or: diameter of cone)
- N_i bearing capacity factors ($i = c, q, \gamma$)
- s_i shape factors ($i = c, q, \gamma$).

When this formula is applied to cone penetration, $p(z)$ is identical to the cone resistance q_c at a depth z (i.e. the average vertical stress at the cone tip). The total resistance is composed by summation of three terms, representing cohesion, surcharge loading and soil weight effects, respectively.

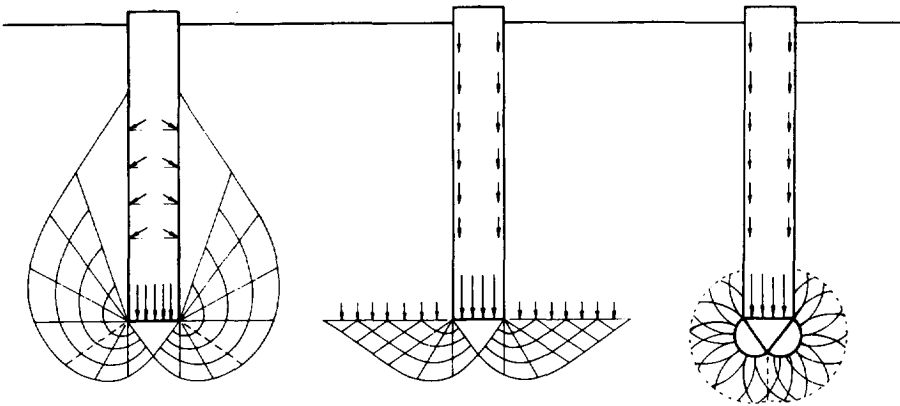


Figure 2.1 Failure patterns under deep foundations (Vesic, 1967).

Equation (2.1) can be reduced for deep cone penetration in purely cohesive soils:

$$q_c(z) = N_c^* c + \sigma_{v,0}(z) \quad (2.2)$$

and in cohesionless soils:

$$q_c(z) = N_q^* \sigma_{v,0}(z) \quad (2.3)$$

in which $s_c N_c$ and $s_q N_q$ are replaced by N_c^* and N_q^* respectively. The transformation from eqn. (2.1) to these simple relations can be achieved, since the third term in eqn. (2.1) is negligible for deep penetration and N_q^* is equal to unity for purely cohesive material. In the literature relations (2.2) and (2.3) are widely accepted, so that the penetration resistance is characterized by one single factor: the so-called cone factor N_c^* for cohesive soils and the so-called bearing capacity factor N_q^* for cohesionless soils.

However, Baligh (1975) and Smits (1977) argue that the penetration process is controlled by at least two fundamental properties of the soil: the shear strength at a certain depth and the compressibility of the soil. For instance, the horizontal stress build-up around the tip and the shaft of the cone depends on the deformation characteristics of the soil. Since the bearing capacity theory cannot take account of soil compressibility, a growing number of investigators have favoured other approaches over the last twenty years.

2.2.2 Cavity expansion models

A method which does account for soil compressibility is the cavity expansion theory. The theory was first developed for application to metal indentation problems (Hill, 1950). The introduction and application of the theory to geotechnical problems came later (Gibson and Anderson, 1961). General solutions associated to cavity expansion in a $c-\phi$ (Mohr-Coulomb) material are presented by Vesic (1972), who extended the model by allowing for the possibility that the volumetric strain in the plastic region is not zero. He treated both the case of expanding a spherical cavity and a cylindrical cavity in an infinite soil mass. Figure 2.2 gives a general picture of the expansion of a cavity. Around the expanding cavity there is a plastic region, indicated by c,ϕ .

Based on his previous work, Vesic (1975) suggested that the pressure around the tip of a cone can be estimated by determining the limit pressure required during the expansion of a spherical cavity. In the case of elasto-plastic material behaviour the cone resistance becomes a function of both the compressibility and the shear strength of the soil. The cavity expansion theory leads to the conclusion that soil compressibility reduces bearing capacity.

As an alternative to the spherical cavity solution, the penetration process can also be modelled by a cylindrical expansion approach. A vertical line is radially expanded until a cylinder has been created with a diameter equal to the cone diameter. Especially if one is interested in the radial stresses around the shaft of the cone, this model can provide useful information.

Another phenomenon which reduces the bearing capacity is the curvature of the Mohr-Coulomb envelope at higher isotropic stress levels. Since the point resistance

in granular media exceeds the stress level ordinarily encountered in geotechnical applications, the response of the soil at elevated stress levels has to be considered. In that case the actual angle of internal friction decreases, i.e. the failure envelope is not straight but convex. Baligh (1975) introduced the envelope curvature in the cavity expansion theory.

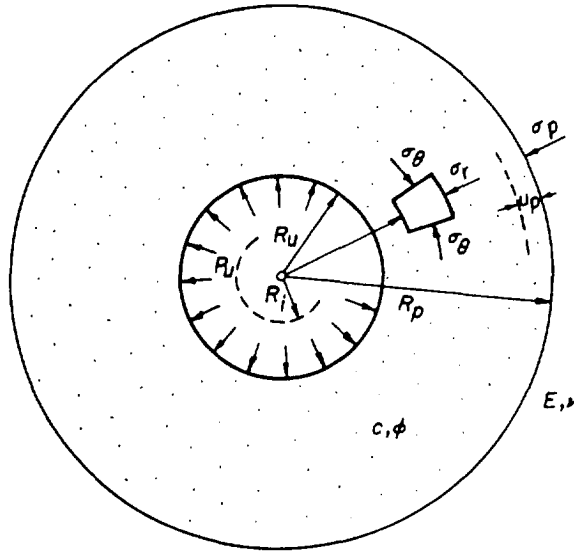


Figure 2.2 Expanding a cavity in an infinite soil mass (Vesic, 1972).

More recently, Luger (1982a) and Carter et al. (1986) presented analytical solutions for limit pressures due to expansion in a non-associated Mohr-Coulomb material. Yu and Houlsby (1991) extended this theory by introducing large strains in the plastic region, whereas the elastic region is treated by a small-strain approach.

One of the latest developments is the combination of critical state models and cavity expansion models. Collins et al. (1992) present analytical solutions for the expansion of spherical and cylindrical cavities in sand using a constitutive model based on critical state theory (Been and Jefferies (1985) and Been et al. (1991)).

2.2.3 Flow models

Steady state model

It is obvious that the penetration process is not identical to the expansion of a spherical or cylindrical cavity. Therefore it has been tried to combine the bearing capacity theory and the cavity expansion theory. For instance, Baligh (1975) interpreted the total cone resistance as a combination of the work required to give the tip of the

cone a virtual vertical displacement (bearing capacity theory) and the work done to expand the soil around the shaft of the cone into the horizontal direction (cylindrical cavity expansion theory). Smits (1977) has introduced a similar model in which both theories are used together.

However, an ordinary summation of both contributions cannot be entirely correct. The assumption that behind the tip of the cone, a "re-newed" cylindrical expansion of soil from zero radius takes place, causes an overestimation of the total work required and thus leads to an overestimation of the cone resistance.

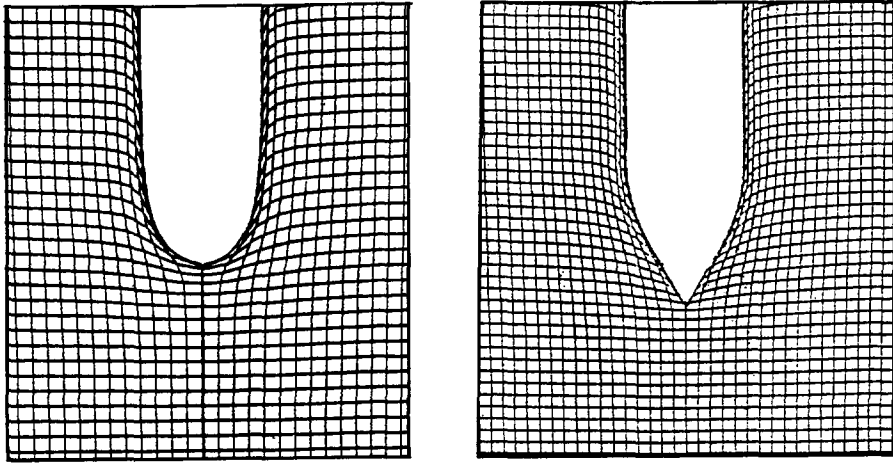
Strain path method

A promising approach accounting for large deformations is the "strain path method" as proposed by Baligh (1985). In this approach, in a first step, soil deformations are considered in terms of a steady flow of soil around a cone. Approximate velocity fields are estimated and differentiated with respect to the spatial coordinates in order to obtain strain rates. Integration of these strain rates along the streamlines defines the strain paths (histories) for individual soil elements around the cone. Finally, a constitutive model is introduced, equilibrium is required and the corresponding stress field around the cone is calculated. Based on the original work done by Baligh, an improved understanding of the strain field during penetration in clay is presented by Acar and Tumay (1986). A further development is to couple this approach with a finite element model. The assumed strain (deformation) field is introduced into a finite element model as the initial situation. In a second step, the equilibrium and corresponding stress field is calculated by the finite element model. Based on this, results for penetration in clay are presented by Teh and Houlsby (1991). From publications it is not clear whether the application may be successful for penetration in frictional material.

A kinematic model, which can be used as initial deformation field for a strain path approach, is the "simple pile model", originally defined by Baligh (1975). The steady state deformation field around the cone according to this approach is visualized in figure 2.3a. The idea behind the simple pile model is adopted from fluid mechanics. The velocity field of expanding a spherical cavity is identical to the velocity field of a point source at a fixed location in a fluid at rest. A sound theoretical base is given by Harder (1989), for instance. When, in addition, this point source moves through the fluid with a constant velocity, then the material coming from the moving point source forms a cylindrical shape with a kind of tip inside the fluid at rest. This shape can be seen as an approximation of the shape of a cone.

Another, rather similar model, has been developed by Levadoux (1980). This model, referred to as the "simple cone model", approximates the shape of the cone tip somewhat more accurately. This is shown in figure 2.3b. He uses a number of sources and sinks to define the kinematics of his model. However, the difference in outcome of

both models is small. The position of each soil particle after the cone has passed is identical (Baligh, 1985 and Harder, 1989).



a.

b.

Figure 2.3 Steady state deformation field around penetrating cone; simple pile model (a) and simple cone model (b).

2.2.4 Finite element models

Small-strain models

The problem of cone penetration has also been analysed by models based on the finite element method. The first computations, in which use was made of a small-strain finite element formulation, were performed by de Borst (1982), Sloan and Randolph (1982) and Griffiths (1982). The results were obtained for purely cohesive material.

In these analyses the cone has, in fact, been introduced into a "pre-bored" hole, with the surrounding soil still in its in-situ stress state. An incremental plastic collapse calculation is carried out and the collapse value identified as the indentation pressure. This interpretation is of course an approximation. During the real penetration of the cone, high lateral and vertical stresses develop adjacently to the shaft of the cone. Building up of stresses around the shaft of the cone results into higher cone penetration pressures than are predicted by an analysis of a cone in a pre-bored hole. There

may be an important difference between a plastic collapse solution and a stress state caused by steady-state penetration. This will be investigated in the present work.

In order to introduce correct initial conditions a large deformation analysis is needed, since a displacement must be simulated of at least several times the diameter of the cone. Such a large penetrating distance is required to give a realistic build up of the shaft pressure due to the effect of cavity expansion. For pressure-dependent (frictional) material behaviour, modelling this effect is necessary to get reliable results. However, for purely cohesive material the difference between the resistance derived from a small-strain (de Borst, 1982) and a large-strain approach (van den Berg, 1991a), remains modest.

Large-strain models

One of the first developments in the field of large-strain finite element analyses was published by Hibbit et al. (1970). Improvements were made by Bathe, Ramm and Wilson (1975) and McMeeking and Rice (1975) who introduced Updated Lagrangean approaches. A Lagrangean approach implies that the nodal points of the finite element discretization are coupled with the material points. Updated Lagrangean means that after each calculation step the mesh is modified. To obtain the new coordinates of the nodal points, the incremental nodal point displacements from the previous step are added to the previous coordinates of the nodes. This method suffers from the disadvantage that if very large local deformations occur, elements will be distorted too much or even turned inside out, causing highly inaccurate solutions or even divergence of the solution procedure.

Presently, publications start to emerge in which the penetration problem is simulated by an Updated Lagrangean model. Budhu and Wu (1991, 1992) have presented a model and some results of penetration of a hollow cylinder in clayey soils. Cividini and Gioda (1988) have presented some results of penetration into a frictional material (Drucker-Prager). They have used zero-thickness elements to model the frictional interface behaviour between the cone and the soil. In their analyses the smoothness of the cone-soil interface is varied. Also Kioussis, Voyiadjis and Tumay (1988) have presented a model and some results of penetration of a smooth cone. Algorithms for a large-strain Updated Lagrangean Camclay model are worked out by Simo and Meschke (1992).

All these models have in common that after each calculation step the new location of the boundary-nodes has to be evaluated ("is a nodal point on the tip or on the shaft of the cone?") and the boundary conditions have to be modified if necessary. When friction between cone and soil is taken into account, the procedure is even more complicated. The procedure proposed by Cividini and Gioda (1988) is shown in figure 2.4. A vertical displacement increment δ_1 is imposed to the cone, equilibrium is

required and the nodal coordinates are modified. The deformed shape is shown in figure 2.4b. Up to here it is a conventional Updated Lagrangean calculation.

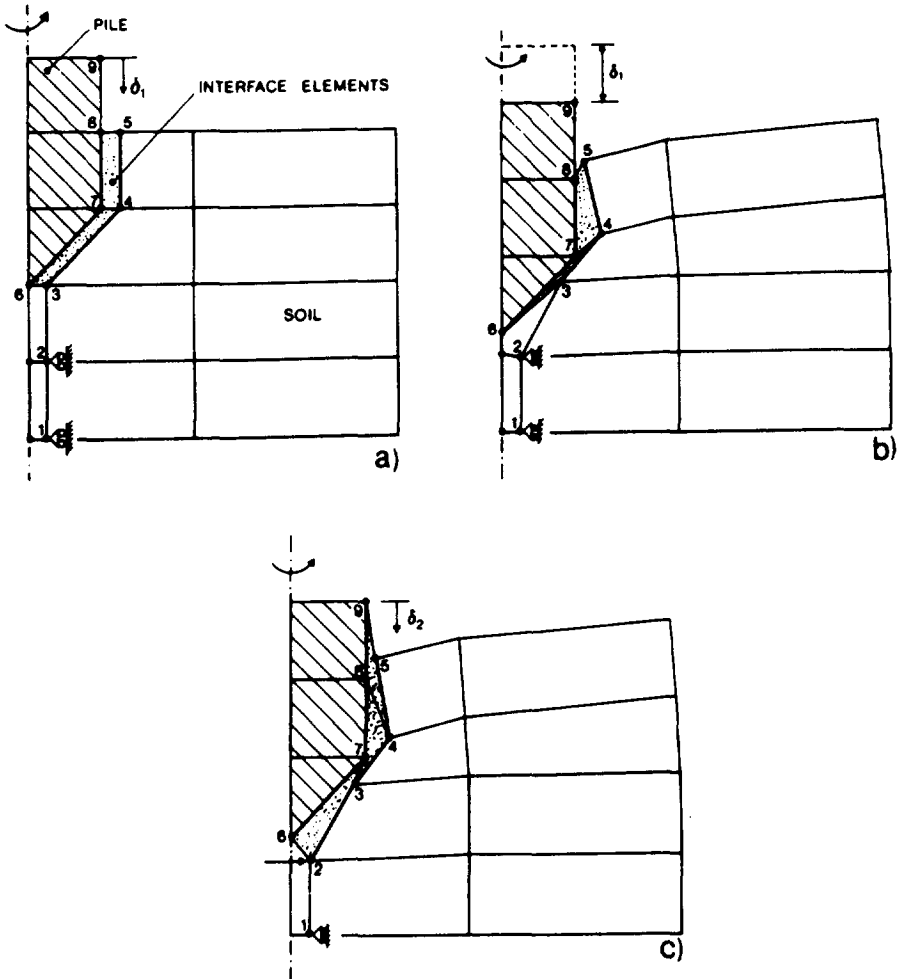


Figure 2.4 Schematization of Updated Lagrangean finite element model to simulate cone penetration including interface friction (Cividini and Gioda, 1988).

The additional step is shown in figure 2.4c: the indices (location) of the interface elements are updated in order to avert numerical problems due to element distortion. The stress-strain states in the new elements are evaluated on the basis of the results of the previous step, and the forces acting on the nodes of the new and old set of interface elements are determined. The difference between the two force vectors is applied to the modified mesh and equilibrium is re-established. Finally, the horizontal

constraint of the first node below the tip of the cone is eliminated. However, the robustness of this way of solving the penetration problem it is not very clear.

2.3 Evaluation of existing models

In the preceding paragraph a number of different approaches to model the cone penetration process has been presented. In this paragraph the advantages and drawbacks of the models are classified under three different headers: a) penetration mechanism, b) soil behaviour and c) layered soil profile. To be able to simulate a real cone penetration test, each of these items has to be considered.

2.3.1 Penetration mechanism

Cone penetration testing is a steady state process. The cone is pushed into the soil at a constant penetration rate. Soil initially located underneath the tip of the cone is pushed aside to make room for the cone. Obviously, this is a large-deformation process. During penetration horizontal stresses are being build up around the shaft.

Therefore a small-strain approach, in which the cone is placed into a pre-bored hole (stresses around the cone equal to in-situ stresses in the soil), followed by an incremental plastic collapse calculation, is not capable to simulate the penetration process properly. This disadvantage not only holds for small-strain finite element models, but, in fact, also for models based on bearing capacity theory. However, a tremendous amount of experience has been put into those models, which often can be used adequately in engineering practice. Cavity expansion models suffer from the fact that the geometry of the cone cannot be modelled adequately. Although a number of parallels can be drawn, cone penetration is not identical to expanding a sphere or cylinder inside a soil mass. A cylinder seems to be a rather good approximation of a cone, but cylindrical expansion only models horizontal (radial) movements. Especially around the tip of the cone vertical soil displacements cannot be neglected. In order to overcome those drawbacks, the strain path method has been developed. The most important idea behind this type of models is "to model the penetration mechanism correctly". Soil initially located underneath the tip of the cone streams upwards along the shaft. Also large-strain finite element models are in essence sufficiently equipped to simulate penetrating distances of several cone diameters and thus modelling real penetration.

2.3.2 Soil behaviour

In a model based on the bearing capacity theory, the constitutive behaviour is limited to rigid plastic models. For clay a purely cohesive Tresca-model is mostly utilized,

whereas for drained behaviour of sand a Mohr-Coulomb model with an associated flow-rule can be applied. Two important disadvantages are:

- The stress build-up around the tip and the shaft of the cone depends on the deformation characteristics of the soil and therefore influences the cone resistance and skin friction.
- An associated flow-rule overestimates the volume change. Especially in confined regions, like the area around the cone tip, this may result in too high bearing capacities (de Borst and Vermeer, 1984).

In cavity expansion models both drawbacks mentioned above do not occur. Elastoplasticity can be introduced into those models, even using a large-strain definition (Yu and Houlsby, 1991) and non-associated flow-rules including strain-softening (Collins and al., 1992). At present, the application of the strain path method is restricted to purely cohesive material. Introducing friction and dilatancy in such a model is very complicated. Results of models in which the strain path method is successfully applied to cone penetration in frictional material cannot be found in literature. In a finite element approach there is no basic limitation upon the constitutive behaviour and sophisticated models as rate-dependent double hardening elastoplasticity can be employed.

2.3.3 Layered soil profile

The geology of the subsoil generally consists of layered deposits. Especially in the upper, say, 20 - 30 meters of the Western part of the Netherlands, interchanging soft cohesive and stiffer frictional layers are found. A large number of investigators have tried to introduce a layered soil profile into a bearing capacity model. Considering a two-layer $c-\phi$ material, the reader is referred to Vesic (1975), Myslivec (1978) and Satyanarayana and Garg (1980), for instance. In order to introduce a second layer into the model, the number of assumptions regarding the failure mechanism increases. In a cylindrical cavity expansion model, in which only horizontal displacements occur, introducing two or more vertical layers is meaningless, since a lower layer will never enter the cone. Modelling two layers in a spherical cavity expansion model around the tip of a cone seems more promising. But again, this requires additional assumptions. The strain path method is by definition a steady state solution. Entering a lower layer and subsequently penetrating it, cannot be simulated. The same drawback holds for a small-strain finite element model. On the other hand, a large-strain approach is sufficiently equipped to describe the mechanics of penetration into another layer.

2.3.4 In conclusion

Table 2.1 summarizes the advantages and drawbacks of the various models. Evaluating the contents of this table, it is concluded that a large-strain finite element

approach is the most versatile approach. In theory, this approach satisfies all our requirements. However, when interest is restricted to penetration in homogeneous clay, the strain path method can also be used adequately.

	penetration mechanism	soil behaviour		layered profile
		sand	clay	
bearing capacity theory	-	+/-	+/-	+/-
cavity expansion theory	-	+	+	-
strain path method	+	-	+	-
finite element model				
- small-strain approach	-	+	+	-
- large-strain approach	+	+	+	+

Table 2.1 Advantages and disadvantages of the models.

2.3.5 Example

In structural mechanics Lagrangean type finite element models are most commonly used. The material is coupled to the nodal points of the finite element discretization. After each increment the deformed (current) configuration is taken as the reference geometry for the next step. In this paragraph an example of the application of an Updated Lagrangean model will be presented to illustrate the possibilities and limitations of this approach when applied to cone penetration in layered media. The finite element mesh at the start of the calculation is presented in figure 2.5a. A smooth cone penetrates out of one layer into another layer. The elastic properties of both layers are identical. The undrained shear strength (Von Mises) of the upper layer is 20% of the strength of the other layer. No initial stresses due to the soil weight are introduced into the model. The material properties adopted in the calculation are summarized in table 2.2.

	layer 1	layer 2
E (kN/m ²)	2000	2000
ν (-)	0.49	0.49
c_u (kN/m ²)	20	100

Table 2.2 Material properties adopted in Updated Lagrangean calculation.

Vertical displacement increments are prescribed and the resulting load-displacement curve is presented in figure 2.6. After a total displacement of about three cone diameters the numerical procedure diverges. The current finite element mesh at that

point is shown in figure 2.5b. A number of elements is largely distorted. Obviously, an Updated Lagrangean approach is not a proper way to solve the problem.

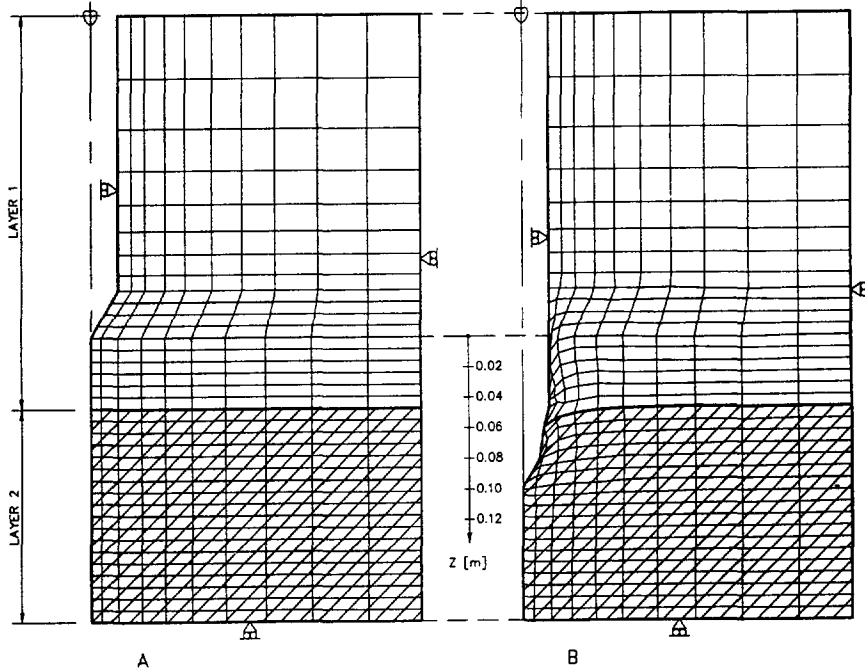


Figure 2.5 Finite element discretization at the start (a) and at the end (b) of the calculation.

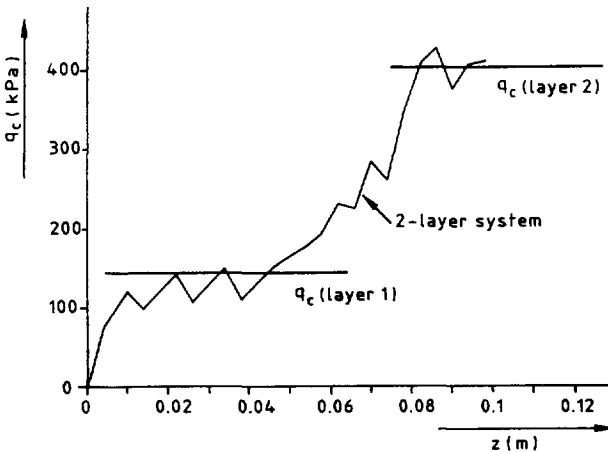


Figure 2.6 Load-displacement curve calculated.

More-over, in the example presented, no frictional interface behaviour between cone and soil was taken into account and the numerically easy to handle Von Mises model was applied rather than the much more sensitive Mohr-Coulomb model with non-associative plasticity.

2.4 Scope of the work

To overcome these drawbacks, a Eulerean approach will now be followed. In contrast to an (Updated) Lagrangean model, the material displacements are uncoupled from the nodal point displacements. In fact, the material streams through the finite element mesh and the geometry of all elements is fixed.

The Arbitrary Lagrangean Eulerean (ALE) formulation has been adopted as a starting point for the present work. This approach was originally introduced by Hughes et al. (1981) and Donea (1983) in the field of fluid mechanics. They introduced Lagrangean, geometrical, boundaries in the simulation of fluid problems, formulated in Eulerean, spatial, coordinates. Liu et al. (1986) extended the same idea to solid material (path dependent behaviour). All those authors started their work at the Eulerean side of the formulation. Over the last ten years, models have started to emerge in which the Updated Lagrangean description is used as a starting point. One of the first models in which an approach is formulated in terms of an extension of an Updated Lagrangean formulation, has been published by Huetink (1982, 1986). He introduced convective terms proportional to the relative displacement increments into the formulation. The finite element program DIEKA, developed during that research work, is used as a base for the present work.

The specific aim of the work is to improve the understanding of the mechanisms associated to penetration in clayey, sandy and layered soil. For that purpose two major extensions of the program were necessary: (1) the implementation of constitutive models for the behaviour of frictional material and (2) the combination of a "Lagrangean" boundary between two layers and a fixed "Eulerean" finite element mesh.

To model the constitutive behaviour of sand, pressure dependent models (Drucker-Prager and Mohr-Coulomb) have been implemented. Hardening/softening rules have been introduced based on a critical density approach. A soil specimen subjected to large shear deformation tends to reach a state of constant density. To model this phenomenon the friction and dilatancy angles are defined as a function of the generated plastic strain. Especially in regions in which large shear strains occur, such as the zone around the tip of a penetrating cone, it is necessary to use this type of models.

In a Eulerean model, material moves through the fixed finite element mesh. Since in the original model the constitutive behaviour of the material was coupled to the fixed elements, the method could only be used for homogeneous material throughout the complete finite element discretization. Hence, since the geology of the subsoil generally consists of layered deposits, the suitability of the model in geotechnical practice was limited. To overcome these problems the model has been extended in the sense that the material properties stream through the mesh as well or, better, the material particle including its constitutive behaviour moves through the fixed finite element mesh.

The model is used to improve the understanding and interpretation of results measured by cone penetration testing. A sensitivity analysis has been performed, results are presented and are compared to other models. The analysis is subdivided into three parts: penetration in homogeneous clay, in homogeneous sand and in layered media. Based on this a number of directives is given to improve the interpretation of measured data. In addition, model tests have been performed to validate the results of the model. In these tests a cone lengthwise cut in half is pushed along a glass plate into the soil. During penetration the deformation pattern around the cone was recorded. A regular CPT has been performed in the center of the testing facility to determine q_c , f_s and u . Tests have been carried out in a layered soil profile.

Chapter 3 gives the theoretical background of the numerical model, whereas chapter 4 presents the results of the application of the model to cone penetration. The model can also be applied to other problems, as it is a general tool to analyse penetration of rigid devices into soil. Chapter 5 presents the results of a numerical and experimental study towards sampling disturbances in clayey soils. For an extensive overview of this work, the reader is referred to van Eekelen (1991) and van Eekelen and van den Berg (1994). The model has also been applied to simulate penetration of driven piles to determine the bearing capacity of a piled foundation (van den Berg, 1992b).

3. Arbitrary Lagrangean-Eulerean model

3.1 Stress and strain at finite deformation

3.1.1 Introduction

The kinematics of a continuous body undergoing finite deformations have been discussed by numerous authors (see for instance: Becker and Burger, 1975). Two basically different approaches can be chosen: a Lagrangean formulation in which stresses and strains are defined with respect to a fixed coordinate system (reference state) and an Eulerean formulation based on a convected coordinate system (current state).

Consider a body A and a point p_A of this body. The configuration A is called the reference configuration and the position vector of p_A relative to a fixed point O is $\underline{\xi}$ (figure 3.1). This body deforms in such a way, that the configuration A changes into the configuration B. This configuration is referred to as the current configuration. The material point p_A corresponds to the point p_B in the deformed state, whereas the element $d\xi_1 d\xi_2$ transforms into $dx_1 dx_2$.

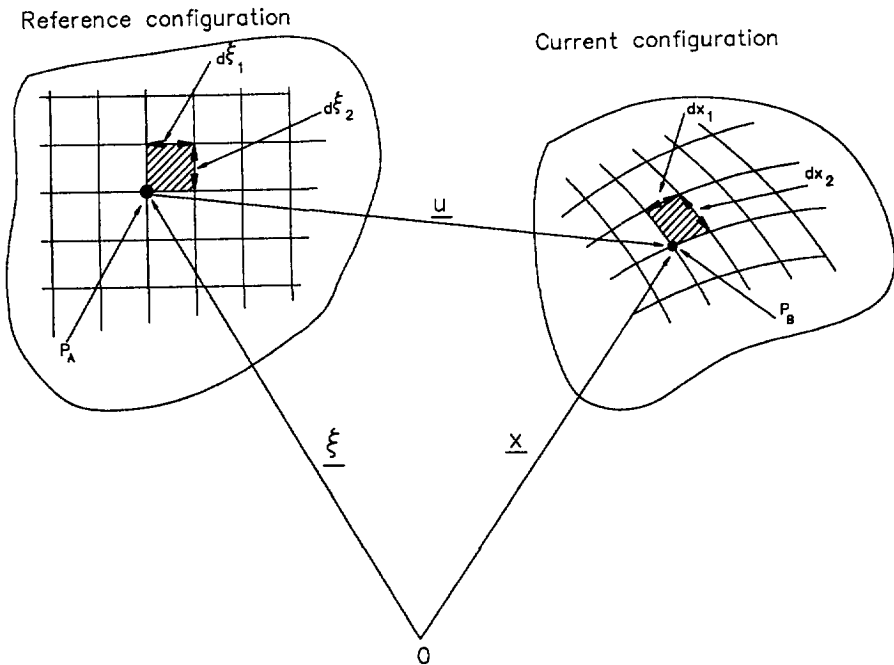


Figure 3.1 Reference and current state.

The deformation gradient tensor F transforms an arbitrary vector $d\underline{\xi}$ into $d\underline{x}$:

$$d\underline{x} = F d\underline{\xi} \quad (3.1a)$$

$$d\underline{\xi} = F^{-1} d\underline{x} \quad (3.1b)$$

Denoting the length of $d\underline{x}$ by dx and the length of $d\underline{\xi}$ by $d\xi$, then the scalar $(dx^2 - d\xi^2)$ can be defined as a measure for the amount of deformation.

$$dx^2 - d\xi^2 = d\underline{x}^T d\underline{x} - d\underline{\xi}^T d\underline{\xi} \quad (3.2)$$

The vectors $d\underline{\xi}$ and $d\underline{x}$ can be eliminated from eqn. (3.2) by using eqn. (3.1a) and (3.1b):

$$dx^2 - d\xi^2 = d\underline{\xi}^T (F^T F - I) d\underline{\xi} \quad (3.3a)$$

$$dx^2 - d\xi^2 = d\underline{x}^T (I - (F^{-1})^T (F^{-1})) d\underline{x} \quad (3.3b)$$

This leads to the definition of two strain tensors:

$$\gamma = \frac{1}{2} (F^T F - I) \quad (3.4a)$$

$$\epsilon = \frac{1}{2} (I - (F^{-1})^T (F^{-1})) \quad (3.4b)$$

The tensor γ relates a vector $d\underline{\xi}$ of the reference state to the strain measure $(dx^2 - d\xi^2)$, while the tensor ϵ relates the vector $d\underline{x}$ of the current state to the same strain measure. The tensor γ is called the Green-Lagrange strain tensor and ϵ the Eulerean (or Euler-Almansi) strain tensor. The Lagrangean and Eulerean strain are related as follows:

$$\gamma = F^T \epsilon F \quad (3.5a)$$

$$\epsilon = (F^{-1})^T \gamma (F^{-1}) \quad (3.5b)$$

Just as with the strain tensors, the stress tensors can also be defined with respect to a fixed (reference) coordinate system and with respect to a deforming (current) system. The 2nd Piola-Kirchhoff stress τ is defined with respect to the reference system, whereas the Cauchy stress σ (or true stress) is defined with reference to the current system.

$$\tau = J (F^{-1})^T \sigma (F^{-1}) \quad (3.6a)$$

$$\sigma = \frac{1}{J} F^T \tau F \quad (3.6b)$$

with:

$$J = \det (F) = \frac{\rho_0}{\rho} \quad (3.7)$$

ρ_0 being the initial density (reference state) and ρ the actual density (current state).

To get a proper description of stresses and strains it is necessary to use a conjugate pair of stress and strain measures (Hill, 1968). This means that the double contraction of a stress and its conjugate strain tensor represents work. The 2nd Piola-Kirchhoff stress is conjugate with the Green-Lagrange strain. The Cauchy stress is conjugate with the Euler-Almansi strain tensor. The Cauchy stress and the Euler-Almansi strain are symmetric tensors as are the 2nd Piola-Kirchhoff stress and the Green-Lagrange strain.

However, using a conjugate pair of stress and strain measures is not a guarantee for a correct large-strain analysis. It is imperative that also the constitutive relation is a "conjugate large-strain" relation. Thus, using Cauchy stress and Euler-Almansi strain the constitutive relation has to be defined in the deformed (current) state too. If large strains occur it is also meaningless to use the 2nd Piola-Kirchhoff stress and the Green-Lagrange strain definitions, for instance, and to maintain a small-strain constitutive relation. This is illustrated by the following one-dimensional example.

3.1.2 1D truss bar

A truss bar is loaded by a force F . The initial length of the bar is l_0 (reference state) and the current length is l_n . The elongation is u . This is graphically shown in figure 3.2.

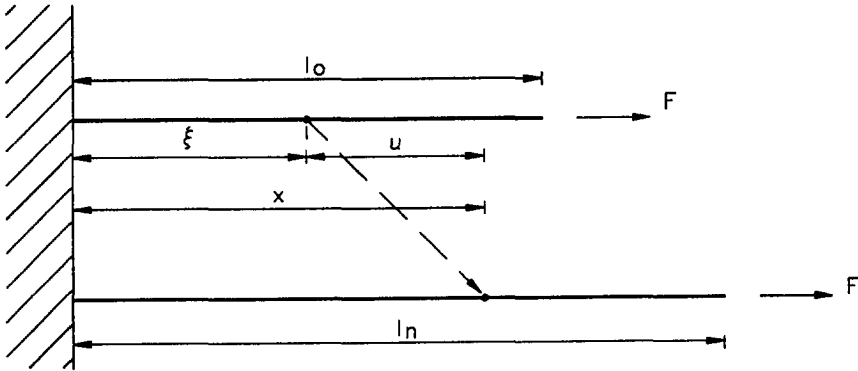


Figure 3.2 1D truss bar (reference and current state).

Using the general notation as presented before, the reference and current configuration can be related by:

$$x = \xi + u \quad (3.8a)$$

$$\xi = x - u \quad (3.8b)$$

The deformation gradient F becomes:

$$F = \frac{dx}{d\xi} = 1 + \frac{du}{d\xi} \quad (3.9a)$$

$$F^{-1} = \frac{d\xi}{dx} = 1 - \frac{du}{dx} \quad (3.9b)$$

Introducing eqn. (3.9a) into eqn. (3.4a) yields the Green-Lagrange strain γ :

$$\gamma = \frac{du}{d\xi} + \frac{1}{2} \left[\frac{du}{d\xi} \right]^2 \quad (3.10)$$

$$\gamma = \frac{l_n - l_0}{l_0} + \frac{1}{2} \frac{(l_n - l_0)^2}{l_0^2} \quad (3.11)$$

On the other hand, combination of eqn. (3.9b) and eqn. (3.4b) gives us the Eulerian strain ϵ :

$$\epsilon = \frac{du}{dx} - \frac{1}{2} \left[\frac{du}{dx} \right]^2 \quad (3.12)$$

$$\epsilon = \frac{l_n - l_0}{l_n} - \frac{1}{2} \frac{(l_n - l_0)^2}{l_n^2} \quad (3.13)$$

After introduction of the constitutive model, the relation between the force F and the elongation u has been defined. This relation will be worked out for a constant value of Young's modulus E . Using the conjugate pair γ and τ gives:

$$F = \tau A_0 = E \gamma A_0 = E A_0 \left[\frac{u}{l_0} + \frac{1}{2} \left(\frac{u}{l_0} \right)^2 \right] \quad (3.14)$$

On the other hand, using ϵ and the conjugate stress σ yields:

$$F = \sigma A_n = E \epsilon A_n = E A_n \left[\frac{u}{l_n} - \frac{1}{2} \left(\frac{u}{l_n} \right)^2 \right] \quad (3.15)$$

Both relations are graphically presented in figure 3.3. In this example E , A_0 and l_0 are taken equal to unity and conservation of volume is assumed. This implies that $A_0 l_0$ is equal to $A_n l_n$. It is clear that both curves only coincide for small-strain levels. So, although both sets of conjugate stress and strain measures are, in essence, sufficiently equipped to describe large deformations, it is also necessary to define a conjugate

constitutive relation in terms of large-strains. The combination with experimental work is essential in order to get a proper description. In the present study, Hooke's law will be used in terms of small-strains to define the elastic part of the constitutive behaviour. Rotations, displacements and plastic strains may be finite.

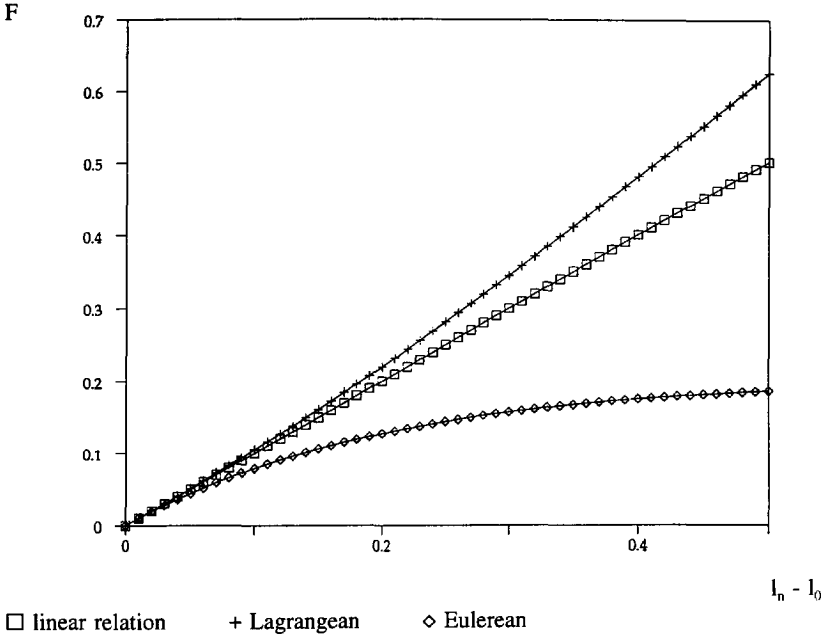


Figure 3.3 F-u relation for truss bar with constant stiffness (Lagrangean and Eulerian approach).

3.1.3 Cauchy stress rate and objectivity

The Eulerian approach will be followed in the present study. Nevertheless, the same set of resulting equations can be obtained by using the Green-Lagrange strain and the 2nd Piola-Kirchhoff stress (Huétink, 1986). For an Eulerian description, it is most common to characterize the deformation process in terms of velocity \underline{v} using the velocity gradient $v_{i,j}$ (see for instance: Johnson and Bamman, 1984 and Stolle and Schad, 1992). The notation "j" implies differentiation with respect to x_j , the j-coordinate of the spatial (or Eulerian) coordinates. The velocity gradient is related to the deformation gradient tensor F :

$$\frac{\partial \underline{v}}{\partial \underline{x}} = \frac{\partial \underline{v}}{\partial \underline{\xi}} \frac{\partial \underline{\xi}}{\partial \underline{x}} = \dot{F} F^{-1} \tag{3.16a}$$

and in component form:

$$v_{i,j} = \frac{\partial v_i}{\partial x_j} \quad (3.16b)$$

The velocity gradient can be decomposed by using the Euler-Cauchy-Stokes decomposition into a symmetric part (rate of deformation or rate of stretching) and a skew-symmetric part (the spin or vorticity tensor):

$$v_{i,j} = d_{ij} + \omega_{ij} \quad (3.17)$$

with:

$$d_{ij} = \frac{1}{2} (v_{i,j} + v_{j,i}) \quad (3.18)$$

$$\omega_{ij} = \frac{1}{2} (v_{i,j} - v_{j,i}) \quad (3.19)$$

The strain rate tensor is associated with the straining of the material, while the spin tensor is associated to the rotation of the material.

Starting from a thermo-dynamical point of view, the stress state in a material is a function of deformation, density, time and temperature (Besseling, 1985). When thermal and time-dependent effects are not taken into account, the stress state in a material only depends on the deformation and the density of the material. Therefore, the constitutive equation for elasto-plastic material can be written in the following general rate-type formulation:

$$\dot{\sigma}_{ij}^o = \frac{\dot{\rho}}{\rho} \sigma_{ij} + D_{ijkl} d_{kl} \quad (3.20)$$

in which D_{ijkl} is a fourth order tensor depending on material parameters. The term with ρ (mass density) results from the natural reference theory (Besseling, 1985).

In finite deformation analyses an objective stress rate, $\dot{\sigma}_{ij}^o$, is needed in the definition of the constitutive model. Such stress rates ensure for instance that rigid body motions do not influence the stress state in the material. Several definitions of objective stress rates can be found in literature (Johnson and Bammann, 1984; Szabo and Balla, 1989). A widely used stress rate satisfying objectivity is the Jaumann stress rate:

$$\dot{\sigma}_{ij}^o = \dot{\sigma}_{ij} + \sigma_{ik} \omega_{kj} - \omega_{ik} \sigma_{kj} \quad (3.21)$$

In eqns. (3.20) and (3.21) σ_{ij} and $\dot{\sigma}_{ij}$ are the Cauchy stress and its rate, respectively. The Jaumann stress rate includes rotational effects. Although a large number of objective stress rate definitions exist, it is important to recognize that, whichever formulation is adopted, identical results must be obtained if the constitutive law for each description is properly developed, proper consideration is given with respect to the finite rotation effects during the numerical integration of constitutive equations and the virtual-work principle is used properly to set up the finite element equations (Stolle and Schad, 1992). At this time it is not really clear which objective stress rate is most appropriate. Direct use of the Jaumann stress rate leads to spurious oscillations in simple shear, when kinematic hardening is used (Nagtegaal en de Jong, 1981). A recent overview on the various rates, including advantages and drawbacks, is given by Cheng and Tsui (1992).

Combining eqn. (3.20) and (3.21) yields the Cauchy stress rate $\dot{\sigma}_{ij}$:

$$\dot{\sigma}_{ij} = D_{ijkl} d_{kl} - \sigma_{ik} \omega_{kj} + \omega_{ik} \sigma_{kj} - \sigma_{ij} d_{kk} \quad (3.22)$$

in which:

$$d_{kk} = - \frac{\dot{\rho}}{\rho} \quad (3.23)$$

The same expression may be obtained by taking the material time derivative of the 2nd Piola Kirchhoff stress and allowing the reference configuration to coincide with the current configuration (Stolle and Schad, 1992). This objective rate is called the Truesdell stress rate. Except for the divergence term, the Truesdell rate has the same form as the Jaumann rate.

3.2 Finite element formulation

The basic equation to express the equilibrium condition is the equation of virtual power. This reads:

$$\delta W = \int_V \sigma_{ij} \delta d_{ij} dV - \int_V \rho F_i \delta v_i dV - \int_S T_i \delta v_i dS = 0 \quad (3.24)$$

where:

- V current volume of the material
- σ_{ij} (true) Cauchy stress
- δd_{ij} virtual rate of deformation
- ρ mass density
- F_i force per unit mass
- δv_i virtual velocity
- S current boundary surface
- T_i surface force per unit area

The virtual rate of deformation depends on the virtual velocity:

$$\delta d_{ij} = \frac{1}{2} (\delta v_{i,j} + \delta v_{j,i}) \quad (3.25)$$

In order to obtain an expression in which the relation between the stress rate and the deformation rate can be substituted the material time derivative of the virtual power has to be taken:

$$\frac{d}{dt} \delta W = \frac{d}{dt} \int_V \sigma_{ij} \delta d_{ij} dV - \frac{d}{dt} \int_V \rho F_i \delta v_i dV - \frac{d}{dt} \int_S T_i \delta v_i dS = 0 \quad (3.26)$$

If the integration area V would be constant, as for instance accepted in a small-strain approach, then the material rate of change could be introduced "inside the integrals" and a rather simple relation would occur. However, in a large (Eulerean) deformation analysis the integration area is not constant, so the material rate of change of an integral with changing integration area has to be considered. In a general form this reads:

$$\frac{d}{dt} \left[\int_V f dV \right] = \int_V [\dot{f} + f v_{k,k}] dV \quad (3.27)$$

Introducing this into eqn. (3.26) the material time derivative of the virtual power can be expressed in the following form:

$$\begin{aligned} (\delta \dot{W}) &= \int_V [\dot{\sigma}_{ij} \delta d_{ij} + \sigma_{ij} (\delta \dot{d}_{ij}) + \sigma_{ij} \delta d_{ij} d_{kk}] dV + \\ &- \int_V [(\rho \dot{F}_i) \delta v_i + \rho F_i \delta v_i d_{kk}] dV + \\ &- \int_S [\dot{T}_i \delta v_i + T_i \delta v_i v_{\alpha,\alpha}] dS = 0 \end{aligned} \quad (3.28)$$

The indices α denote that the surface components of the velocity are considered. The terms containing the time derivative of the virtual rate of deformation and the time derivative of the virtual velocity vanish (Atzema, 1994). Introducing eqn. (3.22) into eqn. (3.28) has as a result:

$$\begin{aligned} (\delta \dot{W}) &= \int_V [\delta d_{ij} (D_{ijkl} d_{kl} - \sigma_{ik} \omega_{kj} + \omega_{ik} \sigma_{kj} - \sigma_{ij} d_{kk}) + \sigma_{ij} \delta d_{ij} d_{kk}] dV + \\ &- \int_V [(\rho \dot{F}_i) \delta v_i + \rho F_i \delta v_i d_{kk}] dV + \\ &- \int_S [\dot{T}_i \delta v_i + T_i \delta v_i v_{\alpha,\alpha}] dS = 0 \end{aligned} \quad (3.29)$$

Using eqns. (3.17), (3.18) and (3.19) and the relation:

$$(\rho \dot{F}_i) = \rho \dot{F}_i + \dot{\rho} F_i = \rho \dot{F}_i - \rho F_i d_{kk} \quad (3.30)$$

yields:

$$\begin{aligned} (\delta \dot{W}) &= \int_V [D_{ijkl} d_{kl} \delta d_{ij} - 2 \sigma_{kj} d_{ik} \delta d_{ij} + \sigma_{ij} v_{k,j} \delta v_{k,i}] dV + \\ &- \int_V [\rho \dot{F}_i \delta v_i] dV - \int_S [\dot{T}_i \delta v_i + T_i \delta v_i v_{\alpha,\alpha}] dS = 0 \end{aligned} \quad (3.31)$$

The finite element method is applied to solve the set of resulting equations. Iso-parametric elements with Gaussian numerical integration have been applied. The velocity field within an element is expressed in the nodal point velocities:

$$v_i = \sum_N \psi_i^N \cdot v_i^N \quad (3.32)$$

$$\delta v_i = \sum_M \psi_i^M \cdot \delta v_i^M \quad (3.33)$$

Here ψ_i^N is the interpolation function related to nodal point N of element e, which depends on local natural coordinates. The rate of deformation d_{ij} , which is the symmetric part of the velocity gradient, can be defined as follows:

$$d_{kl} = \sum_N B^N \cdot v_i^N \quad (3.34)$$

in which B^N is the strain operator which is a third order tensor for each nodal point. This operator can be written as:

$$B^N = \frac{1}{2} [L \cdot \psi_i^N + L \cdot \psi_j^N] \quad (3.35)$$

where L is a matrix containing differential operators, since it relates a displacement field to a strain field. The virtual rate of deformation is calculated in the same way:

$$\delta d_{kl} = \sum_M B^M \cdot \delta v_i^M \quad (3.36)$$

This leads to the following discretized form of eqn. (3.31):

$$(\delta \dot{W}) = \sum_{N,M} [\delta v_i^M (S_1^{MN} + S_2^{MN}) v_i^N] - \sum_M \delta v_i^M \dot{k}^M \quad (3.37)$$

where:

$$S_1^{MN} = \int_V \left[(\mathbf{B}^M)^T \left[\mathbf{D}_{ijkl} - 2\sigma_{ij} \right] \mathbf{B}^N \right] dV + \int_V \left[(L \psi_i^M) \sigma_{ij} (L \psi_i^N) \right] dV \quad (3.38)$$

$$S_2^{MN} = - \int_S \left[\psi_i^M T_i (L \psi_i^N) \right] dS \quad (3.39)$$

$$\dot{k}^M = \int_V (\psi_i^M \rho \dot{F}_i) dV + \int_S (\psi_i^M \dot{T}_i) dS \quad (3.40)$$

Requiring that eqn. (3.37) is equal to zero for arbitrary values of the virtual nodal velocities yields the following set of equations:

$$S^{MN} \cdot v^N = \dot{k}^M \quad (3.41)$$

where:

$$S^{MN} = S_1^{MN} + S_2^{MN} \quad (3.42)$$

The stiffness matrix S^{MN} may be non-symmetric. The matrix S_1^{MN} is symmetric for associated plasticity and non-symmetric for non-associated plasticity. The matrix S_2^{MN} is non-symmetric and only appears if surface forces are present.

If at a time t the shape, state of stress and boundary conditions are known, the nodal point velocities can be solved. Within a time increment Δt the material displacement increments of the nodal points are approximated by:

$$\Delta u_i^N = v_i^N \cdot \Delta t \quad (3.43)$$

So far the method is identical to the Updated Lagrangean approach. In the case of an Updated Lagrangean method the nodal points are coupled with the material points. So, to achieve the new coordinates and total displacements, Δu_i^N has to be added to

the initial coordinates and total displacements at the beginning of the step. This method was introduced by Bathe, Ramm and Wilson (1975) and by McMeeking and Rice (1975). The Updated Lagrangean method has some disadvantages. Especially if very large local deformations occur, elements can be distorted too much or even turned inside out. The problems due to element distortion can be avoided in two different ways. Remeshing or mesh-rezoning was introduced by Gelten et al. (1982). After performing an Updated Lagrangean incremental step, stresses and strains are taken from the old mesh and introduced into a new one. However, in cases of very localized deformation, very frequent re-meshing is required. Another approach is uncoupling nodal point displacements and velocities and material displacements and velocities. This implies that the material can flow through the elements. This approach is called an Arbitrary Lagrangean Eulerean formulation of the problem.

Uncoupling of material and nodal point displacements implies that in addition convection has to be taken into account in order to be able to update the state at the nodal points. A method to calculate this convection has been presented by Huétink (1982, 1986). The basic idea is the introduction of additional continuous stress and strain fields by interpolating of nodal point stresses and strains. The convective terms are calculated as a product of gradients of these additional continuous fields and the displacement increments.

The basic idea will be illustrated for a one-dimensional example. The velocity of a material particle (x^m) at a spatial location x and at time t in a one-dimensional configuration is v^m .

$$v^m = \frac{dx^m}{dt} \quad (3.44)$$

The velocity of a nodal point (x^n) can be expressed as:

$$v^n = \frac{dx^n}{dt} \quad (3.45)$$

The material rate of change of a stress measure σ^m is:

$$\dot{\sigma}^m = \left(\frac{d\sigma}{dt} \right)^m = \frac{\partial \sigma}{\partial t} + v^m \frac{\partial \sigma}{\partial x} \quad (3.46)$$

And the rate of change of the same stress measure in a nodal point can be expressed as:

$$\dot{\sigma}^n = \left(\frac{d\sigma}{dt} \right)^n = \frac{\partial \sigma}{\partial t} + v^n \frac{\partial \sigma}{\partial x} \quad (3.47)$$

Eliminating the spatial rate of the stress from eqn. (3.46) and (3.47), yields:

$$\dot{\sigma}^n = \dot{\sigma}^m + (v^n - v^m) \frac{\partial \sigma}{\partial x} \quad (3.48)$$

Using a fixed mesh, i.e. a mesh in which all nodal points are fixed in space, eqn. (3.48) can be reduced to:

$$\dot{\sigma}^n = \dot{\sigma}^m - v^m \frac{\partial \sigma}{\partial x} \quad (3.49)$$

So, the stress σ in a point with a fixed location x after a time increment Δt can be written as follows (for a simple one-dimensional situation):

$$\sigma^n(x, t + \Delta t) = \sigma^n(x, t) + \dot{\sigma}^m \Delta t - (v^m \Delta t) \frac{\partial \sigma}{\partial x} \quad (3.50)$$

This is graphically shown in figure 3.4, in which location A is a fixed nodal point and Δu the incremental horizontal displacement of point A.

From eqn. (3.50) it is found that the gradient of the stress field has to be determined. Probably, the most simple approach to assess the convective increment is to use a linear interpolation function between integration point values. However, when using elements with linear interpolation of the displacement, the strain gradient vanishes, which implies that the convective increment disappears. Huétink (1986) suggests to use a combined "local-global" smoothing procedure. First local smoothing is applied to translate integration point values to nodal point values. In four node elements a mean value of the four integration points is taken. Subsequently, nodal point values are calculated by taking average nodal values from all elements that are connected to a particular node. Interpolation of these mean nodal point values gives a continuous field over the complete finite element discretization. It was observed that these

simple interpolation fields showed numerical instabilities depending on the size of the displacement increments. To obtain a stable algorithm global smoothing was added (Huétink, 1986). The accuracy of this procedure strongly depends on the problem under consideration and has been worked out extensively by Huétink and van der Helm (1992).

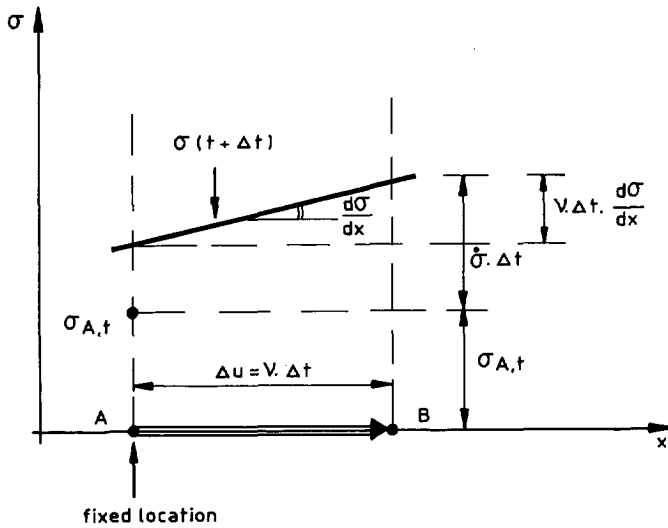


Figure 3.4 Update of stress state at fixed nodal point.

3.3 Eulerean approach of layered systems

3.3.1 Introduction

As elaborated at the end of paragraph 3.2, the consequence of adding convective terms is that nodal point values as stresses and strains "stream" through the finite element mesh or, better, a material particle moves through the mesh. However, since in the model the constitutive behaviour of the material is coupled to the fixed elements, the method is capable of giving reasonable results only for homogeneous material throughout the complete finite element discretization. Hence, since the geology of the subsoil generally consists of layered deposits, the suitability of the model in geotechnical practice is limited. To overcome these problems the model is extended in the sense that the material properties stream through the mesh as well or, better, the material particle including its constitutive behaviour moves through the fixed finite element mesh.

3.3.2 Model

In order to follow the physical path of a material particle, convection is applied to the total displacements of the nodal points. This procedure yields "convected total displacements", analogous to the convected stresses and strains introduced in paragraph 3.2. Considering the same 1D-example given in that paragraph, the convected total displacement of a fixed nodal point, u^n , is calculated by:

$$u^n(x, t + \Delta t) = u^n(x, t) + \Delta u^m - \Delta u^m \frac{\partial \Delta u^m}{\partial x} \quad (3.51)$$

in which the superscript n refers to a fixed nodal point, while the superscript m refers to a material related quantity. This formula is completely analogous to eqn. (3.50). From eqn. (3.51) it is clear that the gradient of the incremental displacement field is required to get the total convected displacement at a fixed nodal point. To derive a smooth continuous field the same "local-global" smoothing procedure is applied as introduced in the derivation of the stress and strain fields. Eqn. (3.51) can also be written in a slightly different form:

$$u^n(x, t + \Delta t) = u^n(x, t) + \left(1 - \frac{\partial \Delta u^m}{\partial x}\right) v^m \Delta t \quad (3.52)$$

From this equation it is clear that if the gradient of the incremental displacement field is equal to zero, the total convected displacement at a fixed nodal point is equal to the summation of the incremental nodal point displacements over the total number of incremental steps. Extension of the model to two dimensions requires convected displacements both in x- and y-direction. These quantities at a fixed location P can be denoted as x_{conv}^P and y_{conv}^P respectively (see figure 3.5).

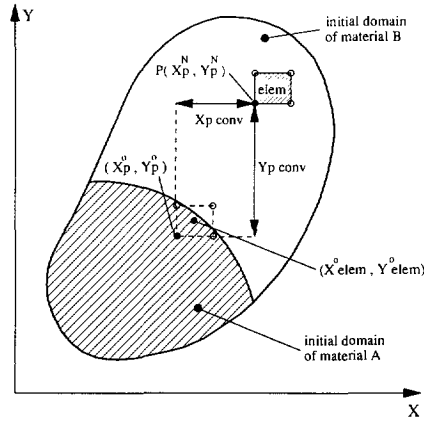


Figure 3.5 Some definitions for moving material front through fixed finite element mesh.

The next step in the calculation procedure is sub-tracting the convected total displacements from the coordinates of the fixed (nodal) point P, in order to derive the original location of the material particle which now has been arrived at point P:

$$x_P^O = x_P^N - x_{conv}^P \tag{3.53}$$

$$y_P^O = y_P^N - y_{conv}^P$$

where:

$$x_{conv}^P = \sum_{i=1}^{nincr} \Delta u_x^P(i) \left[1 - \frac{\partial \Delta u_x^P(i)}{\partial x} \right] \tag{3.54}$$

$$y_{conv}^P = \sum_{i=1}^{nincr} \Delta u_y^P(i) \left[1 - \frac{\partial \Delta u_y^P(i)}{\partial y} \right]$$

where x_p^N and y_p^N are the coordinates of the fixed nodal point P and $nincr$ is the total number of incremental steps.

In order to get an element related quantity the average value of x_j^O and y_j^O of all nodal points connected to the element are calculated:

$$x_{elem}^O = \frac{\sum_{j=1}^{nnod} x_j^O}{nnod} \tag{3.55}$$

$$y_{elem}^O = \frac{\sum_{j=1}^{nnod} y_j^O}{nnod}$$

in which $nnod$ is the total number of nodes per element.

After that it is checked whether the point (x_{elem}^O, y_{elem}^O) is located inside the original domain of material A or inside the original domain of material B (see figure 3.5). Depending on the outcome, the material properties are chosen according to those of material A or material B. If the material index of an element changes from A to B during an incremental step, then the boundary between the materials passes the element under consideration. The material parameters of the element are modified. The modified parameters are subsequently used both in the definition of the new tangent stiffness matrix and in the stress correction routines.

It is noted that this way of parameter adjustment may cause sudden unbalances in the numerical iteration procedure. This implies that in practice the difference between both sets of material parameters is limited, depending on the element size, the stress conditions and the total number of elements. The stability of the iteration procedure can be improved by re-definition of the procedure in the sense that parameter sets are modified per integration point instead of per element.

A fully smooth transition can be achieved by defining the constitutive behaviour of an element in terms of an overlay model (see paragraph 3.4.5) when the boundary between two materials is located inside that element. Depending on the exact location of the boundary, the total material behaviour is composed by a certain percentage of material A and a complementary percentage of material B.

The accuracy of this parameter modification procedure depends on the gradients of the incremental displacement field in relation to the element size, and depends therefore strongly on the problem under consideration. Since use is made of the same pro-

cedures as introduced in the derivation of the convected stresses and strains, the accuracy is fully comparable to the one described extensively by Huétink and van der Helm (1992).

3.3.3 Applications

Two applications are presented in this paragraph to demonstrate the possibilities of a Eulerean approach of layered systems: a 1D and a 2D example.

1D example

A (1D) cylinder consisting of two materials is simultaneously subjected to a steady increasing axial stress (σ) and a material flow in axial direction (u), such that:

$$\sigma = 6.15 u \tag{3.56}$$

Linear elastic material behaviour is assumed. The stiffness of both materials is identical ($E = 100 \text{ kPa}$), while Poissons' ratio differs: ν in the right half of the material is 0.49, whereas this quantity for the other half is equal to 0.0. This implies that, depending on the material, the horizontal stress build-up is either almost equal to the axial stress ($\nu = 0.49$) or equal to zero ($\nu = 0.0$).

The finite element discretization is shown in figure 3.6. The mesh consists of ten square 4-noded axi-symmetric one by one meter elements.

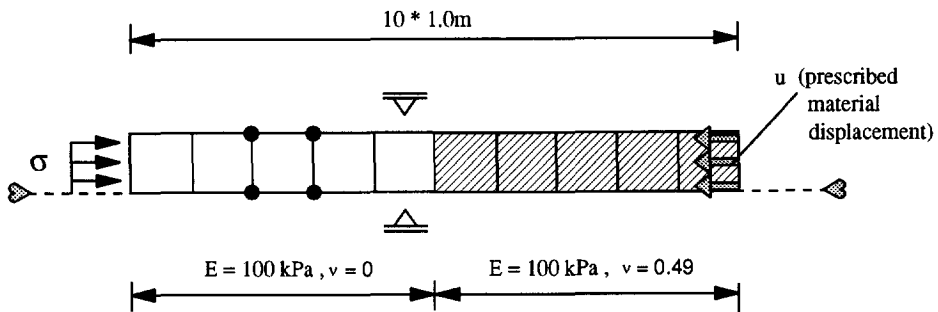


Figure 3.6 Finite element mesh 1D example layered system.

Two cases are considered: one without adjustment of parameters according to paragraph 3.3.2, i.e. the original non-layered version of the program, and the other one

with parameter modification depending on the position of the material front. For both cases the results of four incremental steps are presented: $u = 0.5, 1.0, 1.5$ and 2.0 meter.

Figure 3.7 presents the horizontal stress distribution in the cylinder for the "non-layered" calculation: although the material streams through the mesh, the material properties remain at their original position. Initially, the numerical and analytical solution are in full agreement. Due to local smoothing the horizontal stress at $x = 5$ m is equal to half the value at $x = 4$ m and half the value at $x = 6$ m. At increasing material flow, however, the numerical front stays more and more behind the analytical solution. This can be explained by the fact that the additional horizontal stress build-up, caused by the axial stress increments, only takes place inside the original domain of the material with $v = 0.49$.

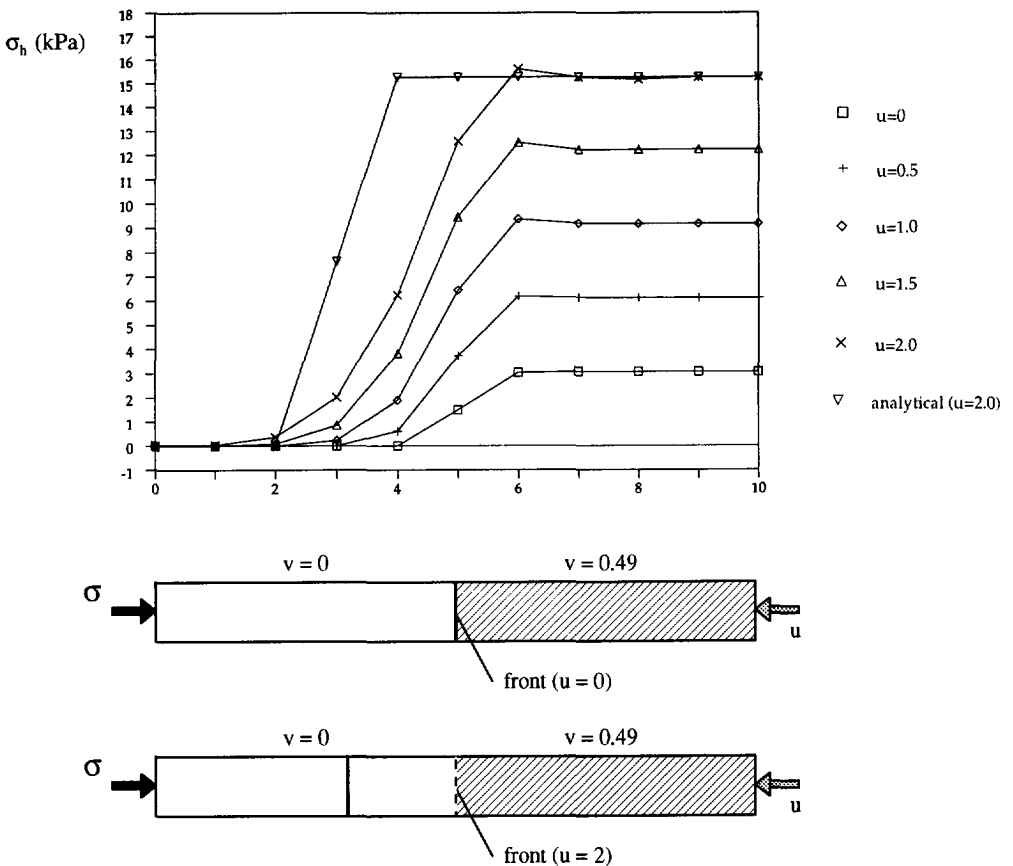


Figure 3.7 Horizontal stress in cylinder: "non-layered" numerical result and analytical solution.

Figure 3.8 presents the result according to the "layered" version of the Eulerian model. The moment the material front passes half the element-width, the material properties are modified. As can be seen, now the numerically derived stress front properly follows the theoretical solution. The difference between the theoretical and numerical distribution is caused by some numerical diffusion associated to the smoothing procedure in determining the convective stress increment.

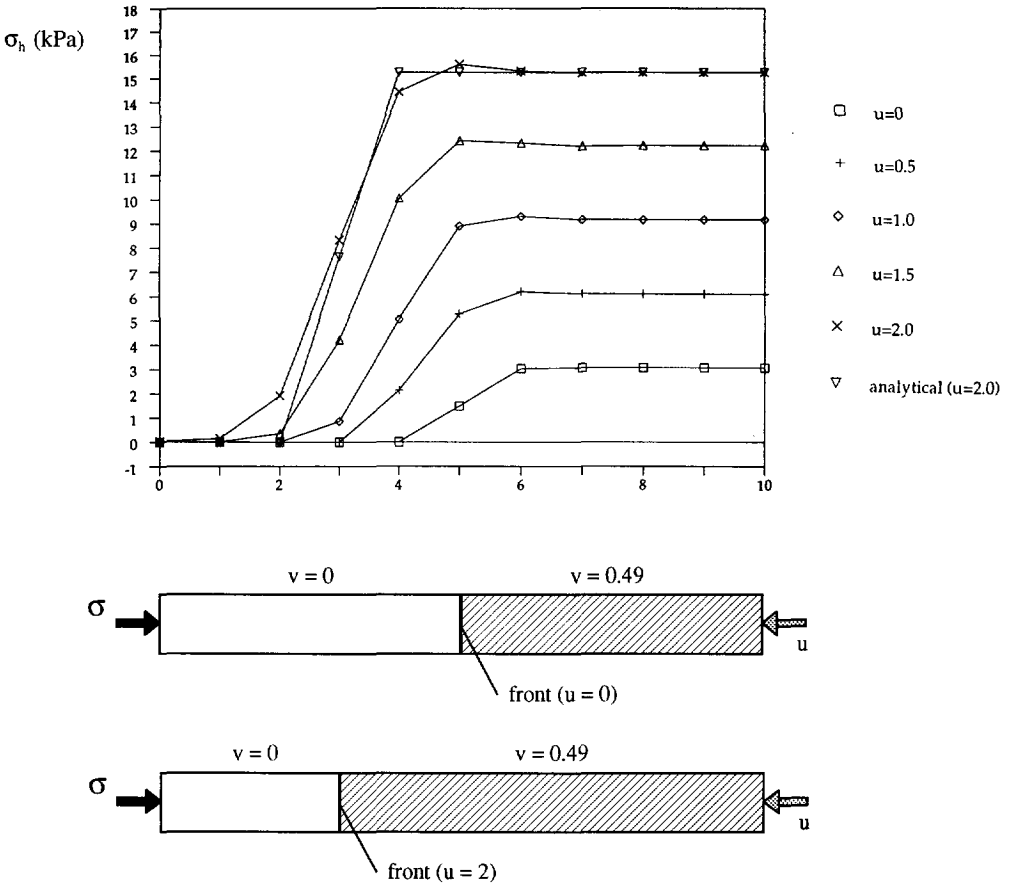


Figure 3.8 Horizontal stress in cylinder: "layered" numerical result and analytical solution.

2D example

A phenomenon widely known in geotechnical engineering practice is that during pile driving underneath the tip of the pile soil coming from upper layers penetrates with the pile into the deeper layers. As will be shown in the second example, the layered Eulerian model is sufficiently equipped to simulate this phenomenon.

The finite element discretization consisting of 478 four-noded square axi-symmetric elements is given in figure 3.9. Initially, the elements are subdivided into two different material groups separated by a horizontal boundary. The lowest row of elements represents material 1, while all the other elements have material properties according to material 2. The material parameters are summarized in table 3.1. No initial stresses are introduced into the model and the constitutive behaviour of both materials is modelled by the von Mises yield criterion.

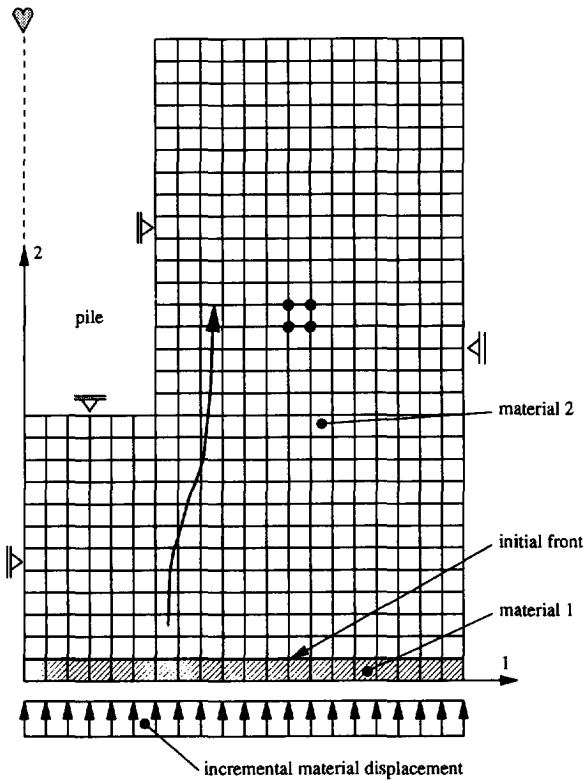


Figure 3.9 Finite element mesh and boundary conditions "pile penetration in layered soil".

	material 1	material 2
E (kPa)	1000	5000
ν (-)	0.49	0.49
c_u (kPa)	10	50

Table 3.1 Material parameters "pile penetration in layered soil".

The pile is modelled as a fixed boundary at the upper left part of the model. The pile is assumed to be smooth, i.e. no shear stress transfer is allowed between pile and soil. Penetration is simulated by adding material at the bottom of the mesh (properties according to material 1). The material streams upward and leaves the mesh at the top. The position of the material front during different stages of the analysis is shown in figure 3.10, in which the shaded area represents material 1, whereas the white region corresponds to material 2. It can be clearly seen that some material of the upper layer (material 2) remains at a position underneath the tip of the pile, while the pile penetrates into the deeper layer (material 1).

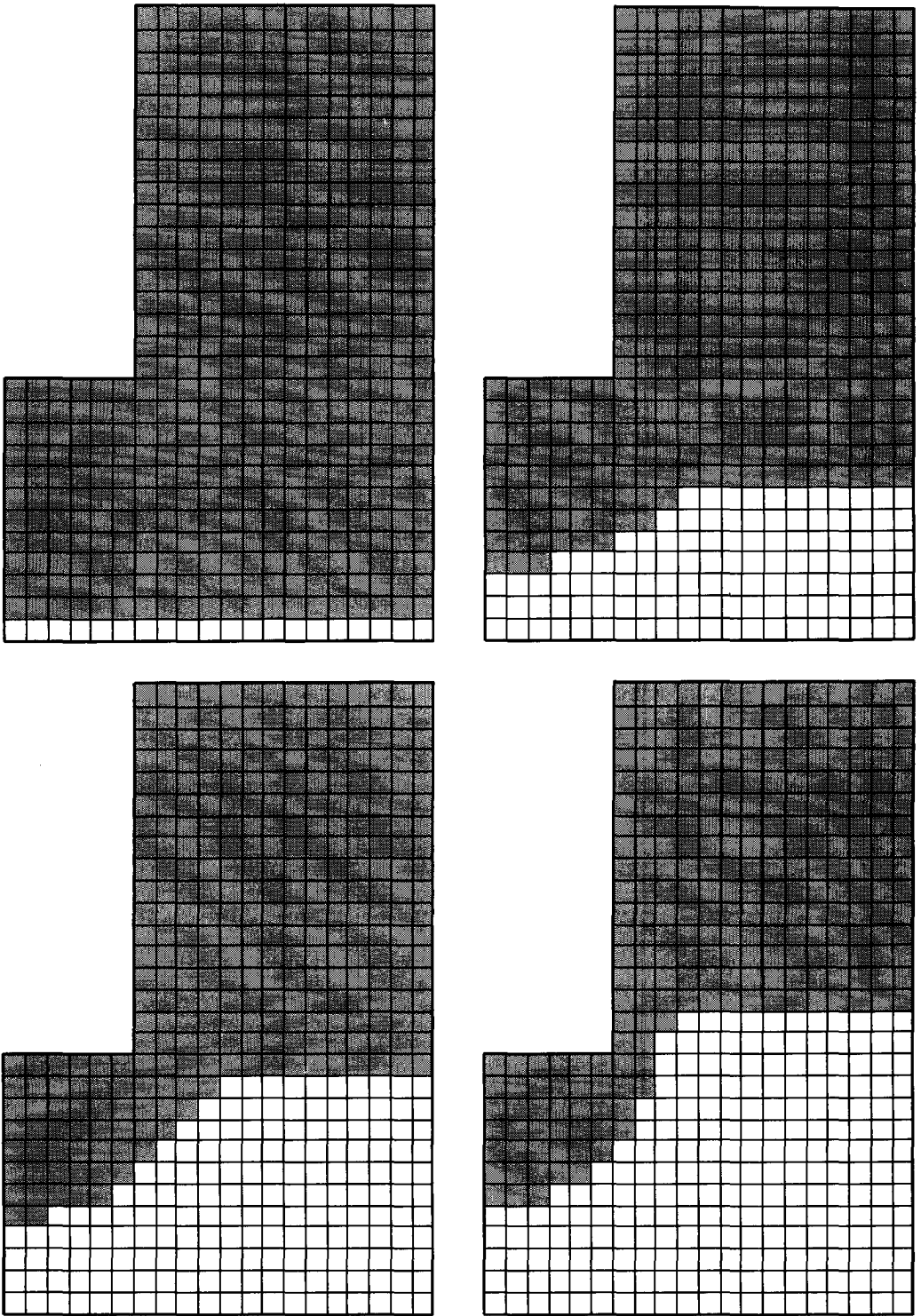


Figure 3.10a Material front during pile penetration in layered soil.

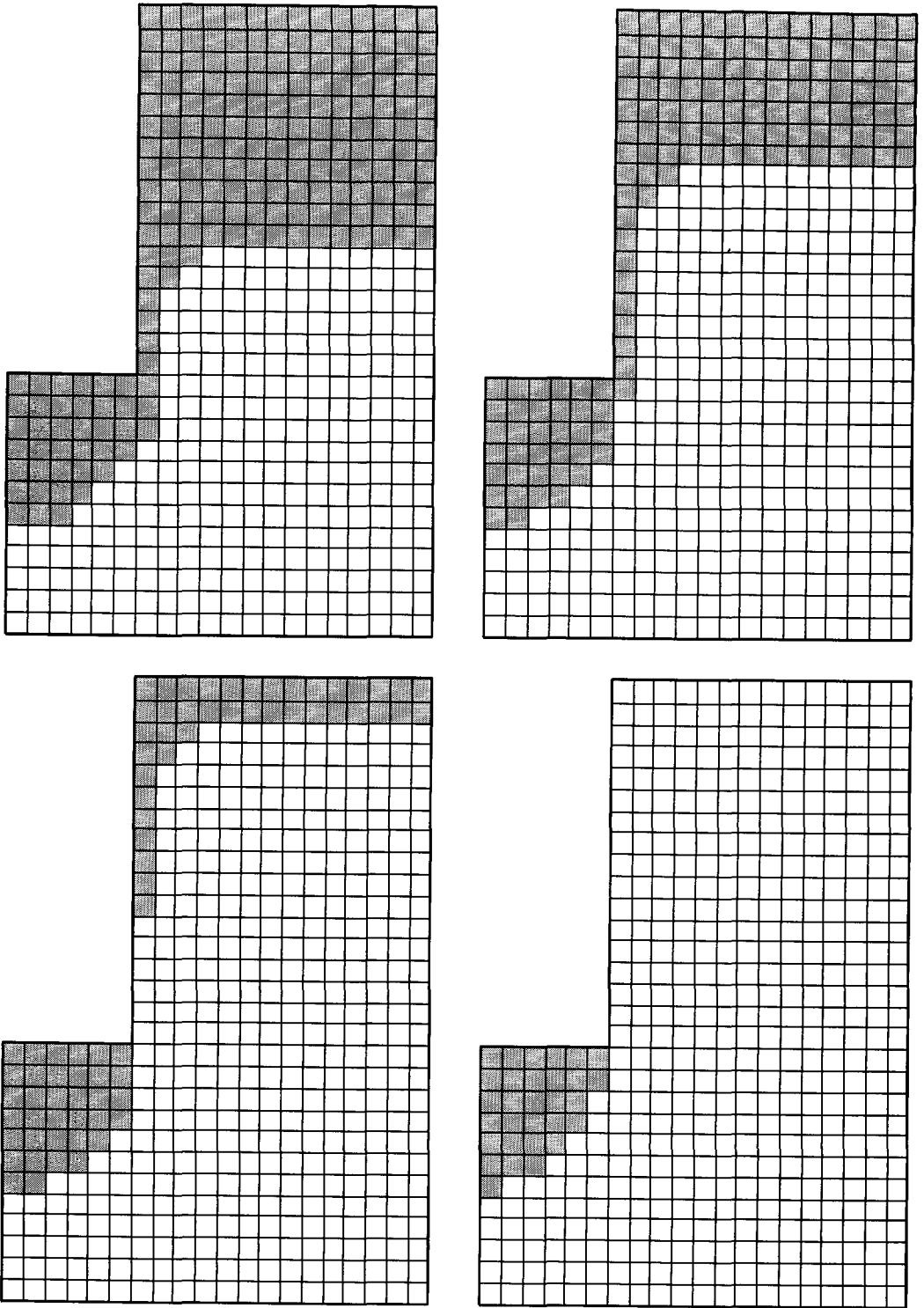


Figure 3.10b Material front during pile penetration in layered soil (continued).

3.4 Constitutive behaviour

3.4.1 General elasto-plastic framework

The constitutive stress rate $\dot{\sigma}_{ij}^c$ is defined as that part of the Cauchy stress rate that depends on the material behaviour and thus can be written as a part of eqn. (3.22) as follows:

$$\dot{\sigma}_{ij}^c = D_{ijkl} d_{kl} \quad (3.57)$$

The spatial rate of deformation can be additively decomposed into an elastic and a plastic part (Nemat-Nasser, 1979; Needleman, 1985):

$$d_{ij} = d_{ij}^{el} + d_{ij}^{pl} \quad (3.58)$$

where d_{ij}^{el} is the elastic component of the strain rate tensor. In the present study Hooke's law will be used in terms of small strains to define the elastic part of the constitutive behaviour. So:

$$\dot{\sigma}_{ij}^c = E_{ijkl} (d_{kl} - d_{kl}^{pl}) = E_{ijkl} d_{kl}^{el} \quad (3.59)$$

where:

$$E_{ijkl} = G (\delta_{il} \delta_{jk} + \delta_{ik} \delta_{jl} + \frac{2\nu}{1-2\nu} \delta_{ij} \delta_{kl}) \quad (3.60)$$

in which δ_{ij} is the Kronecker delta tensor, G is the elastic shear modulus and ν is Poisson's ratio. Although it is known that the elastic behaviour of soil depends on the stress level (for a brief overview see Appendix 3.A), in the present study G and ν are assumed to be constant, for the sake of simplicity.

A similar type of relation as given in eqn. (3.60) can be applied for finite-strain elasticity. Then the Kronecker delta tensor δ_{ij} has to be replaced by terms including the spatial derivatives of the deformed base vectors, usually referred to as the metric tensor in the deformed state. In other words: in finite elastic strain problems the

geometrical changes of the base vectors dx_i (see figure 3.1) have to be taken into account.

For elasto-plastic behaviour, eqn. (3.57) can be written in the following general form:

$$\dot{\sigma}_{ij}^c = (E_{ijkl} - Y_{ijkl}) d_{kl} \quad (3.61)$$

where Y_{ijkl} is a fourth order tensor accounting for plasticity effects, including hardening and/or softening. This term can be determined by introducing the yield function f , which depends on the state of stress and an internal variable H , which is a function of the plastic strain history:

$$f = f(\sigma_{ij}, H) \quad (3.62)$$

and,

$$H = f(d_{ij}^{pl}) \quad (3.63)$$

In this study the following definition has been employed for the history of plastic deformation H :

$$H = \tilde{\epsilon}_{pl} = \int \sqrt{\left(\frac{2}{3} d_{ij}^{pl} d_{ij}^{pl}\right)} dt \quad (3.64)$$

where $\tilde{\epsilon}_{pl}$ is the equivalent plastic strain. The factor $2/3$ is convenient for the evaluation of uniaxial tests: using this factor the equivalent plastic strain coincides with the uniaxial plastic strain in case of isochoric plastic flow.

For plastic yielding an element needs to be in a plastic state ($f=0$) and to remain in a plastic state ($\dot{f}=0$). The first requirement gives:

$$f(\sigma_{ij}, H) = 0 \quad (3.65)$$

while the second condition yields:

$$\frac{\partial f}{\partial \sigma_{ij}} \dot{\sigma}_{ij}^c + \frac{\partial f}{\partial H} \dot{H} = 0 \quad (3.66)$$

Introducing eqn. (3.63) into (3.66) yields:

$$\frac{\partial f}{\partial \sigma_{ij}} \dot{\sigma}_{ij}^c + \frac{\partial f}{\partial H} \frac{\partial H}{\partial \epsilon_{ij}^{pl}} d_{ij}^{pl} = 0 \quad (3.59)$$

The plastic deformation rate is assumed to be:

$$d_{ij}^{pl} = \lambda \frac{\partial g}{\partial \sigma_{ij}} \quad (3.68)$$

with λ a non-negative multiplier if plastic loading occurs ($f=0$ and $\dot{f}=0$) and g the plastic potential function. Combining eqns. (3.58), (3.61), (3.67) and (3.68) yields the plasticity matrix Y_{ijkl} . This matrix can be written as follows:

$$Y_{ijkl} = \frac{E_{ijkl} \frac{\partial g}{\partial \sigma_{kl}} \frac{\partial f}{\partial \sigma_{ij}}^T E_{ijkl}}{h + \frac{\partial f}{\partial \sigma_{ij}}^T E_{ijkl} \frac{\partial g}{\partial \sigma_{kl}}} \quad (3.69)$$

with:

$$h = - \frac{\partial f}{\partial H} \frac{\partial H}{\partial d_{ij}^{pl}} \frac{\partial g}{\partial \sigma_{ij}} \quad (3.70)$$

So, the tangential relation between the stress rate and strain rate becomes:

$$\dot{\sigma}_{ij}^c = \left[E_{ijkl} - \frac{E_{ijkl} \frac{\partial g}{\partial \sigma_{kl}} \frac{\partial f}{\partial \sigma_{ij}}^T E_{ijkl}}{h + \frac{\partial f}{\partial \sigma_{ij}}^T E_{ijkl} \frac{\partial g}{\partial \sigma_{kl}}} \right] d_{kl} \quad (3.71)$$

For the integration of eqn. (3.71) different integration schemes can be used. Here use is made of the implicit Euler backward algorithm (de Borst, 1987). In the predictor phase the material is assumed to behave fully elastically. So, a trial stress σ_{ij}^t is computed:

$$\sigma_{ij}^t = \sigma_{ij}^{old} + E_{ijkl} \Delta d_{kl} \quad (3.72)$$

where σ_{ij}^{old} is the stress at the beginning of the loading step. Correction for inelastic behaviour is made in a corrector phase. Using a single point numerical integration rule and evaluating the gradients to the yield function and the plastic potential function for σ_{ij}^t , we arrive at the following equation for the constitutive stress increment.

$$\Delta \sigma_{ij}^c = \Delta \sigma_{ij}^t - \frac{f(\sigma_{ij}^t) E_{ijkl} \frac{\partial g}{\partial \sigma_{kl}}}{h + \frac{\partial f}{\partial \sigma_{ij}}^T E_{ijkl} \frac{\partial g}{\partial \sigma_{kl}}} \quad (3.73)$$

This integration method is suitable for single-surface yield criteria. An example of such a yield criterion is the Drucker-Prager model (see figure 3.11). The yield function f and the plastic potential g are defined as follows:

$$f = \sqrt{3J_2} + \alpha p + k \quad (3.74)$$

$$g = \sqrt{3J_2} + \beta p \quad (3.75)$$

with:

$$J_2 = s_{xx}s_{yy} + s_{yy}s_{zz} + s_{zz}s_{xx} + s_{xy}^2 + s_{yz}^2 + s_{zx}^2$$

$$p = \frac{1}{3} [\sigma_{xx} + \sigma_{yy} + \sigma_{zz}]$$

$$\alpha = \frac{6 \sin \phi}{3 - \sin \phi}, \quad \beta = \frac{6 \sin \psi}{3 - \sin \psi}$$

$$k = \frac{6c \cos \phi}{3 - \sin \phi}$$

where s_{ij} is the deviatoric part of the stresses, c is the cohesion, ϕ is the friction angle and ψ is the dilatancy angle.

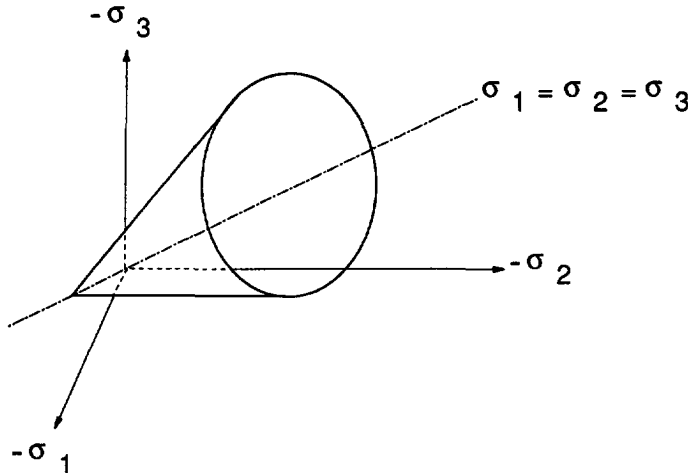


Figure 3.11 Drucker-Prager model.

Introducing the perfectly plastic Drucker-Prager model ($h=0$) into eqn. (3.73), it appeared that for any arbitrary stress increment a direct return mapping to the yield surface is ensured. Comparison of this integration method to a mean normal integration rule, for instance, indicated that the application of a fully implicit method decreases computer run-time substantially. It is remarked that the Drucker-Prager model has to be written in the form of eqn. (3.74) to provide a rigorous return to the yield surface. A quadratic form of the model, as sometimes found in literature, does not give a direct return and internal iterations are necessary.

For $\phi = \psi = 0$, the model reduces to the von Mises model, often referred to as the J_2 -plasticity theory.

3.4.2 On the Mohr-Coulomb model

The yield function f and the corresponding plastic potential function g according to the Mohr-Coulomb failure criterion can be written as follows:

$$f = \frac{1}{2}(\sigma_3 - \sigma_1) + \frac{1}{2}(\sigma_3 + \sigma_1) \sin \phi - c \cos \phi \quad (3.76)$$

$$g = \frac{1}{2}(\sigma_3 - \sigma_1) + \frac{1}{2}(\sigma_3 + \sigma_1) \sin \psi \quad (3.77)$$

with:

$$\sigma_3 \geq \sigma_2 \geq \sigma_1$$

where σ_1 , σ_2 and σ_3 are principle stresses, c is the cohesion, ϕ is the friction angle and ψ is the dilatancy angle. The Mohr-Coulomb model is visualized in figure 3.12.

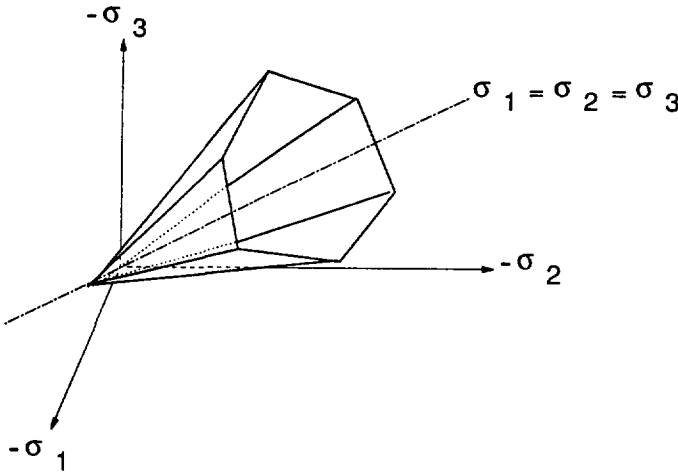


Figure 3.12 Mohr-Coulomb model.

The theoretical framework presented in paragraph 3.4.1 is suitable for single-surface yield criteria. Application of Mohr-Coulomb's failure criterion implies that discontinuities are introduced and two yield functions can be active at the same time. To handle these singularities exactly, an adequate algorithm is presented by de Borst (1987) and de Borst et al. (1991). Assuming that, for instance, two yield functions f_1 and f_2 are active, the rate equation becomes:

$$\dot{\sigma}_{ij}^c = \left[E_{ijkl} - \frac{E_{ijkl} [M_{ijkl} - N_{ijkl}] E_{ijkl}}{\mu_1 \mu_4 - \mu_2 \mu_3} \right] d_{kl} \quad (3.78)$$

with:

$$M_{ijkl} = \mu_1 \frac{\partial g_2}{\partial \sigma_{ij}} \left[\frac{\partial f_2}{\partial \sigma_{kl}} \right]^T + \mu_4 \frac{\partial g_1}{\partial \sigma_{ij}} \left[\frac{\partial f_1}{\partial \sigma_{kl}} \right]^T$$

$$N_{ijkl} = \mu_2 \frac{\partial g_1}{\partial \sigma_{ij}} \left[\frac{\partial f_2}{\partial \sigma_{kl}} \right]^T + \mu_3 \frac{\partial g_2}{\partial \sigma_{ij}} \left[\frac{\partial f_1}{\partial \sigma_{kl}} \right]^T$$

$$\mu_1 = \left[-\frac{\partial f_1}{\partial H} \frac{\partial H}{\partial \epsilon_{ij}^{pl}} + E_{ijkl} \left[\frac{\partial f_1}{\partial \sigma_{kl}} \right]^T \right] \frac{\partial g_1}{\partial \sigma_{ij}}$$

$$\mu_2 = \left[-\frac{\partial f_1}{\partial H} \frac{\partial H}{\partial \epsilon_{ij}^{pl}} + E_{ijkl} \left[\frac{\partial f_1}{\partial \sigma_{kl}} \right]^T \right] \frac{\partial g_2}{\partial \sigma_{ij}}$$

$$\mu_3 = \left[-\frac{\partial f_2}{\partial H} \frac{\partial H}{\partial \epsilon_{ij}^{pl}} + E_{ijkl} \left[\frac{\partial f_2}{\partial \sigma_{kl}} \right]^T \right] \frac{\partial g_1}{\partial \sigma_{ij}}$$

$$\mu_4 = \left[-\frac{\partial f_2}{\partial H} \frac{\partial H}{\partial \epsilon_{ij}^{pl}} + E_{ijkl} \left[\frac{\partial f_2}{\partial \sigma_{kl}} \right]^T \right] \frac{\partial g_2}{\partial \sigma_{ij}}$$

Using a single point numerical integration rule and evaluating the gradients to the yield function and the plastic potential function for σ_{ij}^t (eqn. (3.72)), we arrive at the following equation for the constitutive stress increment:

$$\Delta \sigma_{ij}^c = \Delta \sigma_{ij}^t - m E_{ijkl} \frac{\partial g_1}{\partial \sigma_{kl}} - n E_{ijkl} \frac{\partial g_2}{\partial \sigma_{kl}} \quad (3.79)$$

with:

$$m = \frac{\mu_4 f_1(\sigma_{ij}^t) - \mu_2 f_2(\sigma_{ij}^t)}{\mu_1 \mu_4 - \mu_2 \mu_3}$$

$$n = \frac{\mu_1 f_2(\sigma_{ij}^t) - \mu_3 f_1(\sigma_{ij}^t)}{\mu_1 \mu_4 - \mu_2 \mu_3}$$

For the Mohr-Coulomb criterion, one can derive an expression analytically indicating whether one or two yield functions are active. For smooth parts of the curve (one yield function is active) eqn. (3.73) has to be used to determine the constitutive stress increment, whereas for corner regions (two functions are active) eqn. (3.79) has to be applied. In figure 3.13 the Mohr-Coulomb criterion is visualized in the π -plane. Inside the shaded areas, two yield functions are active at the same time. In the next sections indicators are developed for distinguishing between smooth parts, triaxial compression corners (in figure 3.13 indicated by A) and triaxial extension corners (indicated by B).

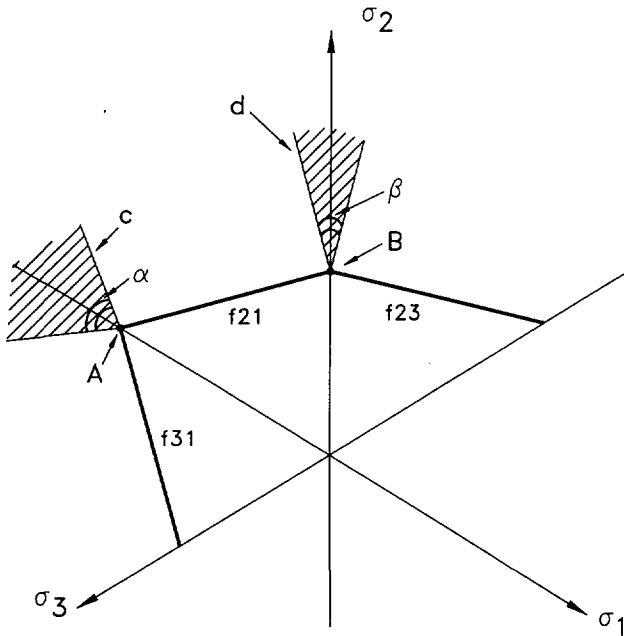


Figure 3.13 Mohr-Coulomb criterion; areas in which one or two yield functions (shaded area) are active.

Triaxial compression stress state

The first direction of the intersection-plane (indicated by c in figure 3.13) is a line in the 3-dimensional stress space at which two yield functions are zero at the same time (i.e. a ridge of the Mohr-Coulomb model, figure 3.12). Suppose f_{21} and f_{31} are zero:

$$f_{21} = \frac{1}{2} (\sigma_2 - \sigma_1) + \frac{1}{2} (\sigma_2 + \sigma_1) \sin \phi - c \cos \phi = 0 \quad (3.80a)$$

$$f_{31} = \frac{1}{2} (\sigma_3 - \sigma_1) + \frac{1}{2} (\sigma_3 + \sigma_1) \sin \phi - c \cos \phi = 0 \quad (3.80b)$$

The second vector of the intersection-plane, is the return mapping direction:

$$E_{ykl} \frac{\partial g_{21}}{\partial \sigma_{kl}} \quad (3.81)$$

The plane spanned by these two vectors separates between the areas: at one side of the plane two yield functions are active and at the other side only one yield function is active. The analytical expression for this plane is:

$$f_{31} - h_c (\sigma_2 - \sigma_3) = 0 \quad (3.82)$$

in which:

$$h_c = \frac{(2\nu \sin \psi) (\sin \phi + 1) + (\sin \phi - 1) (\sin \psi + 2\nu - 1)}{(1 - 2\nu) + (1 - 2\nu) \sin \psi}$$

Triaxial extension stress state

For a triaxial extension stress state, the intersection-plane is indicated by the plane d (see figure 3.13). The first direction can be found by intersecting the yield functions f_{21} and f_{23} :

$$f_{21} = \frac{1}{2} (\sigma_2 - \sigma_1) + \frac{1}{2} (\sigma_2 + \sigma_1) \sin \phi - c \cos \phi = 0 \quad (3.83a)$$

$$f_{23} = \frac{1}{2}(\sigma_2 - \sigma_3) + \frac{1}{2}(\sigma_2 + \sigma_3) \sin \phi - c \cos \phi = 0 \quad (3.83b)$$

The second vector of the plane, is the return mapping direction:

$$E_{\eta kl} \frac{\partial g_{21}}{\partial \sigma_{kl}} \quad (3.84)$$

The plane spanned by these two vectors now becomes:

$$f_{23} - h_e (\sigma_1 - \sigma_3) = 0 \quad (3.85)$$

in which:

$$h_e = \frac{(2\nu \sin \psi)(\sin \phi - 1) + (\sin \phi + 1)(\sin \psi - 2\nu + 1)}{-(1 - 2\nu) + (1 - 2\nu) \sin \psi}$$

In figure 3.14 the intersection-planes are visualized for different sets of parameters. As can be seen in this figure, for ψ is equal to zero, the angles α and β are identical and do not depend on Poisson's ratio. However, when dilatancy plays a role, the angles α and β become different. The size of the angles is controlled by the parameters ν and ψ . For the extreme case that $\nu \rightarrow 0.5$, both α and β are equal to zero, independent of ϕ and ψ .

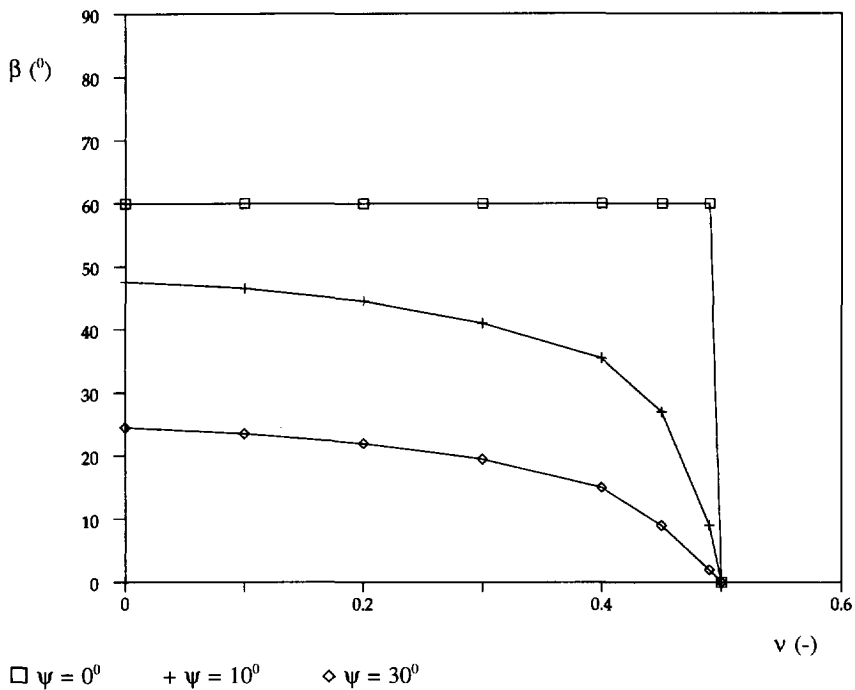
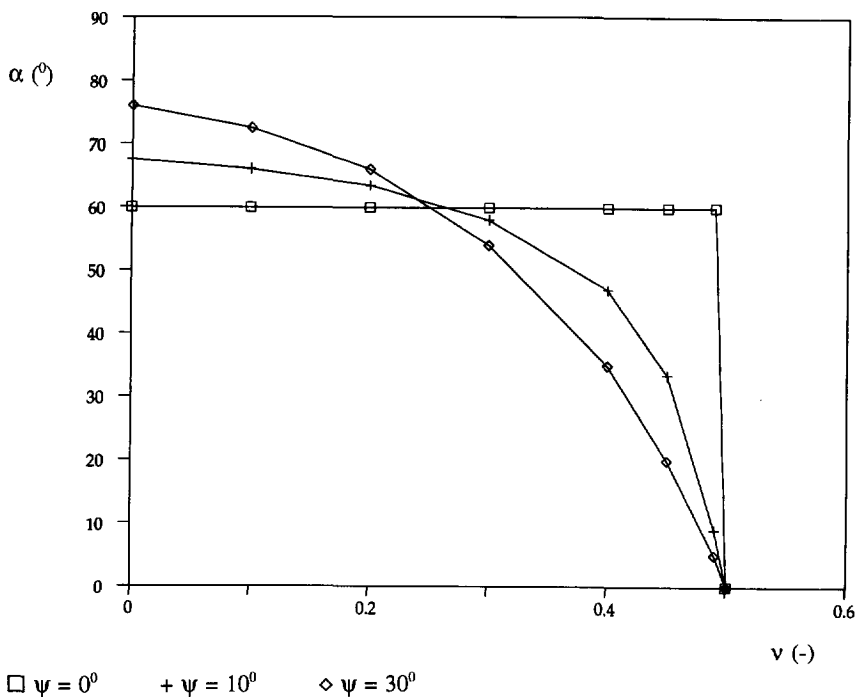


Figure 3.14 Angles α and β (for the definition see figure 3.13) as a function of ν and ψ (for $\phi=30^\circ$).

3.4.3 Constant volume at enlarged shear strain

Introduction

Shear dilatancy of a dense sand specimen, i.e. volume increase associated with shear distortion, was first discussed by Reynolds (1885). Bent Hansen (1958) introduced the dilatancy angle ψ , which can be defined as the ratio of plastic volume change over generated plastic shear strain. In the perfectly plastic models as discussed before, the dilatancy angle has a constant value and is independent of the shear strain. Especially in regions where shear deformations are concentrated, this may lead to un-realistic "volume-growth". In confined regions, for instance around the tip of a deep penetrating cone, this may lead to un-realistic stress build-up (de Borst and Vermeer, 1984). In reality, at enlarged shear deformation, volumetric effects will disappear step by step and the density of the sand specimen tends to go to a constant value. Typical test-results are presented in figure 3.15.

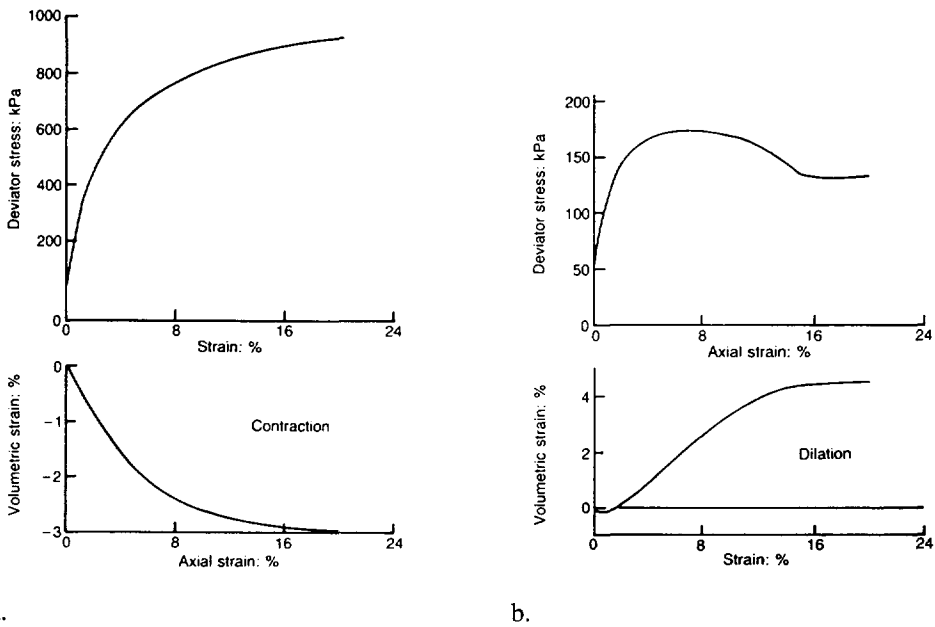


Figure 3.15 Typical test results (Been, Jefferies, Hackey, 1991); a. loose sample and b. dense sample.

For a loose sample contraction occurs (figure 3.15a), while for a dense sample dilatancy (figure 3.15b) occurs. In both cases, at a certain deformation level, a state of constant volume will be reached, defined as the state at which the soil continues to

deform at constant stress and constant void ratio. In Appendix 3.B a brief overview is given of the work carried out on the critical state of sand.

Introduction into constitutive model

In spite of all this interesting work the existence of a critical void ratio is still a point of discussion. Questions, for instance, about the relation between the critical void ratio and the loading history, have not yet been answered conclusively. However, whether it is a critical state or not, it is undoubtedly true that the density of sand tends to go to a constant value at enlarged shear deformation. This effect can be captured into a number of constitutive models, for instance Cam clay type models (Atkinson and Bransby (1978)). In this type of models the yield function and the plastic potential function coincide. Plastic deformation therefore obeys an associated flow rule.

An alternative justification of a flow rule is provided by the stress-dilatancy theory, originally developed by Rowe (1962). He worked out the expression which states that, for a soil being sheared, the ratio of the work done by the driven stress in any strain increment should be constant. Rowe's stress-dilatancy theory has met with greatest success in describing the behaviour of sand (Wood, 1990). Up to now, this approach is favoured above "Cam clay type" models. Experimental results can be reproduced more accurately (Stroud, 1971) and Rowe (1971)). However, for loose sands (Pastor et al., 1990) and within certain limits for the stress ratio (q/p) (Wood, 1990), the critical state theory can be applied too. Here we will follow Rowe's stress-dilatancy theory.

Experimental results, like those presented in figure 3.15, can be approximated by introducing an exponential relation between the dilatancy angle and the equivalent plastic strain $\tilde{\epsilon}_{pl}$ (see eqn. (3.64)):

$$\sin \psi^* = \sin \psi_0 e^{-\frac{\tilde{\epsilon}_{pl}}{\xi}} \quad (3.86)$$

in which ψ^* is the actual dilatancy angle, decreasing from an initial value (ψ_0) to zero and ξ is a softening parameter. Following the stress-dilatancy theory of Rowe (1962), the friction angle is related to the dilatancy angle as follows:

$$\sin \phi^* = \frac{\sin \phi_{cv} + \sin \psi^*}{1 + \sin \psi^* \sin \phi_{cv}} \quad (3.87)$$

in which ϕ^* is the actual friction angle, decreasing from an initial (or: peak) value to ϕ_{cv} (the friction angle at constant volume). After introduction of eqn. (3.86) into (3.87) $\sin(\phi^*)$ becomes a function of the equivalent plastic strain:

$$\sin \phi^* = \frac{\sin \phi_{cv} + \sin \psi_0 e^{-\frac{\bar{\epsilon}_{pl}}{\xi}}}{1 + \sin \psi_0 \sin \phi_{cv} e^{-\frac{\bar{\epsilon}_{pl}}{\xi}}} \quad (3.88)$$

Now the hardening modulus h as defined in eqn. (3.70) can be elaborated. This modulus can also be described in the following form:

$$h = - \frac{\partial f}{\partial \bar{\epsilon}_{pl}} \frac{\partial \bar{\epsilon}_{pl}}{\partial d_{ij}^{pl}} \frac{\partial g}{\partial \sigma_{ij}} \quad (3.89)$$

Using the Mohr-Coulomb failure criterion for the definition of f yields:

$$\frac{\partial f}{\partial \bar{\epsilon}_{pl}} = \frac{1}{3} (\sigma_1 + \sigma_2) \frac{\partial \sin \phi^*}{\partial \bar{\epsilon}_{pl}} - c \frac{\partial \cos \phi^*}{\partial \bar{\epsilon}_{pl}} \quad (3.90)$$

and working out the second part of eqn. (3.89) for the Mohr-Coulomb failure criterion gives:

$$\frac{\partial \bar{\epsilon}_{pl}}{\partial d_{ij}^{pl}} \frac{\partial g}{\partial \sigma_{ij}} = \sqrt{\left[\frac{1}{3} [1 + \sin^2 \psi^*] \right]} \quad (3.91)$$

Introducing eqn. (3.90) and (3.91) into eqn. (3.89) yields:

$$h = - \sqrt{\left[\frac{1}{3} [1 + \sin^2 \psi^*] \right]} \left[\frac{1}{2} (\sigma_1 + \sigma_3) \frac{\partial \sin \phi^*}{\partial \bar{\epsilon}_{pl}} - c \frac{\partial \cos \phi^*}{\partial \bar{\epsilon}_{pl}} \right] \quad (3.92)$$

Introducing this softening approach into a Mohr-Coulomb or Drucker-Prager model results in the following set of total six parameters: Young's modulus E , Poisson's ratio ν , cohesion c , friction angle at constant volume ϕ_{cv} , initial dilatancy angle ψ_0 and the hardening/softening parameter ξ .

At the moment it is commonly accepted, that ϕ_{cv} varies between, say, 28° and 35° , although there is a large amount of scatter. (Been et al. (1991) and Collins et al. (1992)).

The softening parameter ξ can be derived from the results of large deformation tri-axial tests, presented in graphs like figure 3.15. Evaluating a large number of test results, it seems to be reasonable to assume that, after reaching a level of 5 % shear strain, $\sin(\psi^*)$ has decreased to 50 % of $\sin(\psi_0)$. Introducing this into eqn. (3.86), the parameter ξ becomes equal to 0.072.

3.4.4 Contact-frictional interface behaviour

In soil-structure-interaction analyses, it is important to model the behaviour at the interface between construction and soil correctly. Two mechanisms can be distinguished at the interface: the contact-gapping mechanism and the frictional shearing mechanism.

In geotechnical engineering practice, roughly speaking, three ways of modelling interface behaviour can be distinguished. The simplest approach models the interaction by elastic or elasto-plastic node-to-node springs. Another approach is to consider the soil-structure interface as a thin continuum layer, while the third approach replaces the interface zone with a bi-dimensional constitutive relation (Boulon, 1989 and van Langen and Vermeer, 1990)). Following this approach the interface behaviour between construction and soil is described in terms of a relation between the normal and shear tractions, t_n and t_s , and the normal and shear relative displacements across the interface, Δu_n and Δu_s . In geomechanics, when the stresses are within the elastic region, the normal and shear relations are generally assumed to be independent:

$$\begin{bmatrix} t_n \\ t_s \end{bmatrix} = \begin{bmatrix} D_{11} & 0 \\ 0 & D_{22} \end{bmatrix} \begin{bmatrix} \Delta u_n \\ \Delta u_s \end{bmatrix} \quad (3.93)$$

In this matrix D_{11} stands for the relation between normal traction and normal relative displacement: the contact-gapping mechanism. D_{11} resembles an elastic spring stiffness, a very stiff spring to simulate contact up to a specified maximum normal trac-

tion. If the normal traction exceeds this value a discrete gap arises between construction and soil and the normal traction reduces to zero. To model un-loading, or closure of the gap, correctly, it is essential to store the gap-width.

Generally, the friction mechanism, D_{22} , is described as follows: up to a specified shear stress, depending on the normal stress at the interface, elastic shear-behaviour is assumed. If the shear stress exceeds this threshold, plastic slip deformation occurs at the interface. If the shear stress exceeds this level (τ_{pl} in figure 3.16) plastic, irreversible, slip deformation occurs. This shear stress level τ_{pl} is defined by the Coulomb friction model:

$$\tau_{pl} = a + \sigma_n \tan \delta \tag{3.94}$$

where a is the adhesion between construction and soil, σ_n is the normal stress at the interface and δ is the interface friction angle.

Up to an ultimate maximum shear stress τ_{max} , τ_{pl} depends on the normal stress at the interface (figure 3.16). So:

$$\tau_{pl} \leq \tau_{max} \tag{3.95}$$

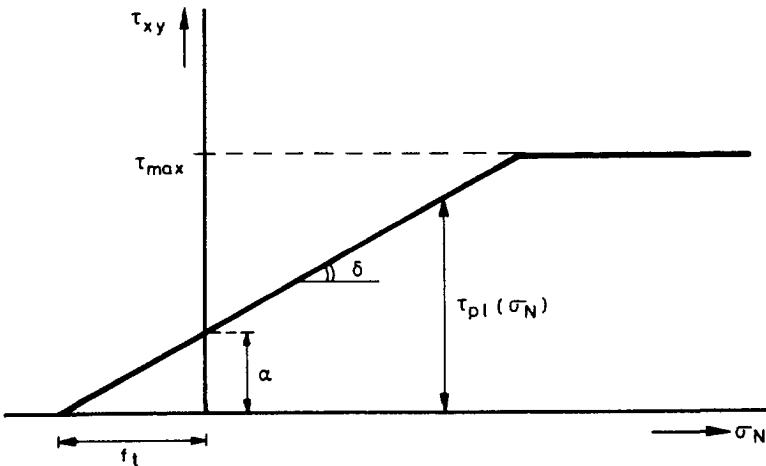


Figure 3.16 Interface behaviour between construction and soil.

For an extensive overview of the numerical procedure and advantages and drawbacks of various interface elements and integration schemes the reader is referred to Schellekens (1992).

3.4.5 Soil as a two-phase medium

Introduction

The material soil consists of a grain skeleton and pores, full of water and/or air. Beneath the ground water table, usually, two phases are taken into account: grains and water. However, it is remarked that a small amount of air strongly influences compressibility (Barends, 1980; Teunissen, 1982).

Following Terzaghi the total soil stress σ_{ij} can be subdivided into effective stress σ'_{ij} and pore water pressure p :

$$\sigma_{ij} = \sigma'_{ij} + p \delta_{ij} \quad (3.96)$$

The two-phase character of the soil can be accounted for in a number of different ways. The most complete approach is a fully coupled analysis, in which the interaction between deformation and pore water pressure is integrated in the resulting equations. The total linearized set of equations for the coupled problem of soil - pore fluid interaction is given by (Zienkiewicz et al., 1988), amongst others. The definition of this set of equations in a finite element formulation can be found in van den Berg and Visschedijk (1991b). This approach will not be followed in the present work.

Overlay model

Under purely undrained conditions soil can be modelled by a so-called overlay (or: fraction) model. Besseling (1958) introduced this kind of models to simulate hysteresis effects of metals due to cyclic loading. An overlay model can be represented by a parallel chain of a number of sub-models (see figure 3.17). Each of the sub-models stands for a certain percentage of the material.

The constitutive behaviour of the pore water part of the soil is modelled by a linear elastic model (shear modulus negligible and bulk modulus equal to K_w). The change of the pore water pressure can be calculated as follows:

$$\Delta p = K_w \frac{\Delta V_p}{V_p} = \frac{K_w}{n} \frac{\Delta V_p}{V} \approx \frac{K_w}{n} \delta_{kl} \Delta \epsilon_{kl} \quad (3.97)$$

in which n is the porosity, V is the total volume and V_p is the volume of the pores.

To determine the effective stress increment any constitutive model for the effective stress can be used without changes to the formulation (Teunissen, 1991). So:

$$\Delta \sigma'_{ij} = D_{ijkl} \Delta \epsilon_{kl} \quad (3.98)$$

Combination of equation (3.98) and (3.99) yields the total stress increment:

$$\Delta \sigma_{ij} = D_{ijkl} \Delta \epsilon_{kl} + \frac{K_w}{n} \delta_{ij} \delta_{kl} \Delta \epsilon_{kl} = [D_{ijkl} + D_{ijkl}^w] \Delta \epsilon_{kl} \quad (3.99)$$

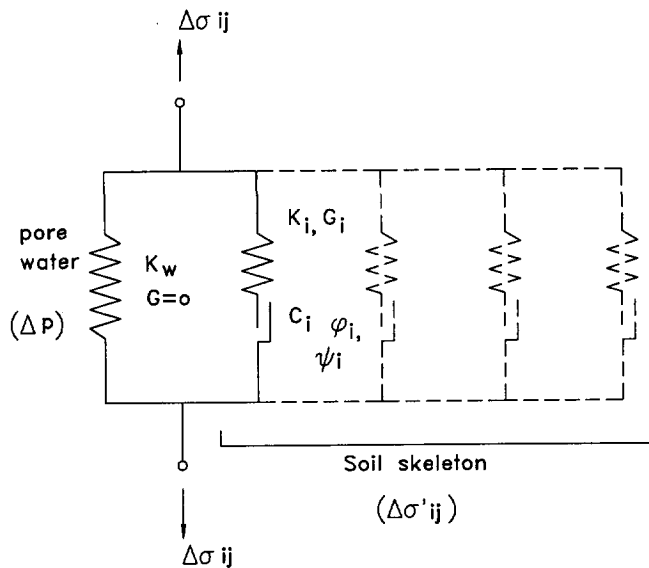


Figure 3.17 Overlay model to model undrained soil behaviour.

It is noted that the sub-model representing the behaviour of the soil skeleton can be sub-divided once more into a number of different sub-models (see figure 3.17), each of them representing a part of the soil skeleton. For instance: a parallel chain of a number of perfectly plastic models with progressive strength may be used to model strain hardening effects. However, it appeared that this approach can only be applied to constant volume plasticity: since the strain of all sub-models is forced to be equal, dilatant behaviour in one of the sub-models causes enlargement of volume in the other elements too, which leads to un-loading in elastic sub-models.

Uncoupled analysis

An uncoupled analysis can be performed in order to derive a first order estimate of the generated pore water pressure. Following this approach, initially, deformations are calculated by a conventional effective stress finite element analysis. Based on the

deformation field calculated, the corresponding pore water pressures are determined in a separate groundwater flow analysis. Originally, this approach was developed by Koning at Delft Geotechnics about 20 years ago. It is noted that the smaller the permeability of the material the larger the difference to a fully coupled analysis.

When applied to the cone penetration problem the following steps can be distinguished.

step 1: An effective stress finite element calculation is carried out using the hardening/softening Mohr-Coulomb model introduced in paragraph 3.4.3. The result of each incremental step is that the volumetric strain increment is known in each integration point and after extrapolation also in each nodal point j : $\Delta \epsilon_{vol,j}$.

step 2: The average volumetric strain increment in each element i is calculated by taking the mean value of the nodal points:

$$\Delta \bar{\epsilon}_{vol}(i) = \frac{\sum_{j=1}^{nnode} \Delta \epsilon_{vol,j}}{nnode} \quad (3.100)$$

in which $nnode$ is the number of nodes per element.

step 3: The volume change of element i in cubic meters is determined by multiplying the volumetric strain increment by the volume of the element (for the definitions see figure 3.18).

$$\Delta V(i) = \Delta \bar{\epsilon}_{vol}(i) b_i h_i 2\pi R_i \quad (3.101)$$

step 4: The volume change of element i per unit time (in cubic meters per second) is calculated by multiplying the volume change by the penetrating velocity and dividing by the vertical displacement increment (see figure 3.18).

$$Q(i) = \frac{\Delta V(i) v}{\delta} \quad (3.102)$$

step 5: In the center of each (axi-symmetric) element a circular line-source or a circular line-sink around the penetrating cone is assumed. A source when the volume of the element increases (dilatant behaviour) and a sink when the volume decreases (compactive behaviour). The rate of discharge of each

line-source or -sink is equal to the volume change per unit time of the element under consideration as derived in step 4.

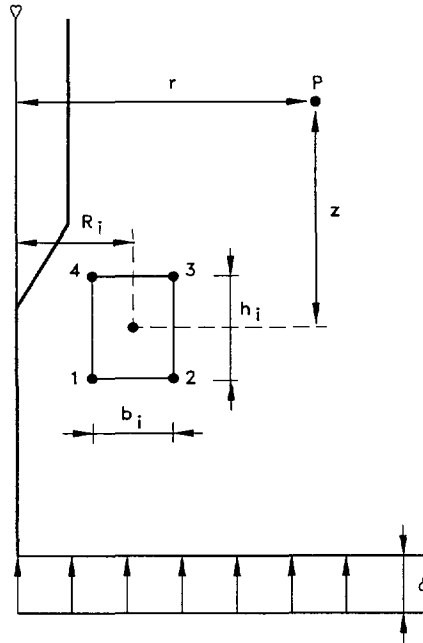


Figure 3.18 Some definitions for uncoupled analysis of cone penetration.

The potential height h (or: hydraulic head) in an arbitrary point P with coordinates (r,z) , see figure 3.18, caused by a circular line-source/sink, is worked out analytically in Appendix 3.C, and can be written as:

$$h(r,z) = \frac{Q}{2\pi^2 k} \frac{1}{\sqrt{(R+r)^2 + z^2}} K(m) \quad (3.103)$$

with:

$$K(m) = \int_{\xi=0}^{\frac{\pi}{2}} (1 - m \sin^2 \xi)^{-\frac{1}{2}} d\xi \quad (3.104)$$

and:

$$m = \frac{4rR}{r^2 + z^2 + 2rR + R^2} \quad (3.105)$$

The integral $K(m)$ can be approximated by (Abramowitz and Stegun, 1970):

$$K(m) = A(m) + B(m) \ln\left(\frac{1}{1-m}\right) + \epsilon(m) \quad (3.106)$$

where:

$$A(m) = a_0 + a_1(1-m) + a_2(1-m)^2 + a_3(1-m)^3 + a_4(1-m)^4 \quad (3.107)$$

$$B(m) = b_0 + b_1(1-m) + b_2(1-m)^2 + b_3(1-m)^3 + b_4(1-m)^4 \quad (3.108)$$

Introducing the following values for the coefficients a_i and b_i , the error $\epsilon(m)$ is less than 2.10^{-8} :

a_0 :	1.38629436112	b_0 :	0.5
a_1 :	0.09666344259	b_1 :	0.12498593597
a_2 :	0.03590092383	b_2 :	0.06880248576
a_3 :	0.03742563713	b_3 :	0.03328355346
a_4 :	0.01451196212	b_4 :	0.00441787012

step 6: Finally, the potential height in an arbitrary point P around the cone can be derived by summation of the influences of all sources and/or sinks:

$$h(r,z) = \sum_{i=1}^{nelem} \frac{Q(i)}{2\pi^2 k} \frac{1}{\sqrt{(R(i)+r)^2 + z^2}} K(m(i)) \quad (3.109)$$

in which $nelem$ is the total number of elements.

3.5 Validation of the model

3.5.1 Introduction

The Eulerian finite element model is applied to analyze the load-displacement behaviour of a footing subjected to a vertical loading. For associated Mohr-Coulomb plasticity there are analytical solutions for the bearing capacity of the footing. For plane strain conditions the limit load is given by Prandtl (1921) and for axi-symmetric conditions by Cox et al. (1961). In this paragraph the application of the model is restricted to axi-symmetry (a circular footing) and linear elastic perfectly plastic Mohr-Coulomb constitutive behaviour.

3.5.2 Application to circular footing

The finite element mesh consists of 72 elements (figure 3.19). Four-noded elements are used, in which the constant volume condition is imposed for the average deformation of the element rather than for all four Gaussian points (Nagtegaal et al., 1974; Hughes, 1987; Teunissen, 1991). In that case the number of incompressibility constraints per element reduces from four to one. This type of elements, also called enhanced B elements, is closely related to elements with selective reduced integration, in which the volumetric strain is integrated using one-point quadrature, in the isoparametric center of the element. This type of elements gives reliable results with respect to the limit load, at least for constant volume conditions (Teunissen, 1991).

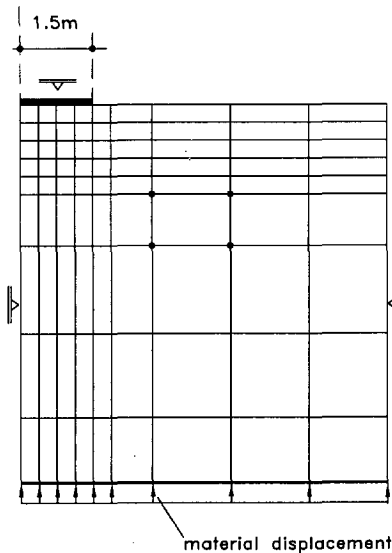


Figure 3.19 Finite element mesh for circular footing.

The footing is modelled by a fixed boundary at the top of the mesh. The vertical displacement of the footing is suppressed while the horizontal displacement is free. A global unbalance criterion is used equal to 0.1 %, whereas the calculation is carried out using a tangential stiffness approach, updated before each iteration. Since the material behaviour is non-associative, a non-symmetric stiffness matrix occurs and has to be solved. As a consequence of a Eulerean approach, in which the material streams through the mesh, the loading consists of a prescribed material displacement at the bottom of the mesh.

The linear elastic perfectly plastic Mohr-Coulomb model is used to model the constitutive behaviour of the soil. Twelve runs have been carried out, characterized in table 3.2. In addition to the columns containing material properties and initial stress conditions, the final column contains an "E" for an Eulerean type calculation and an "L" for an Updated Lagrangean approach.

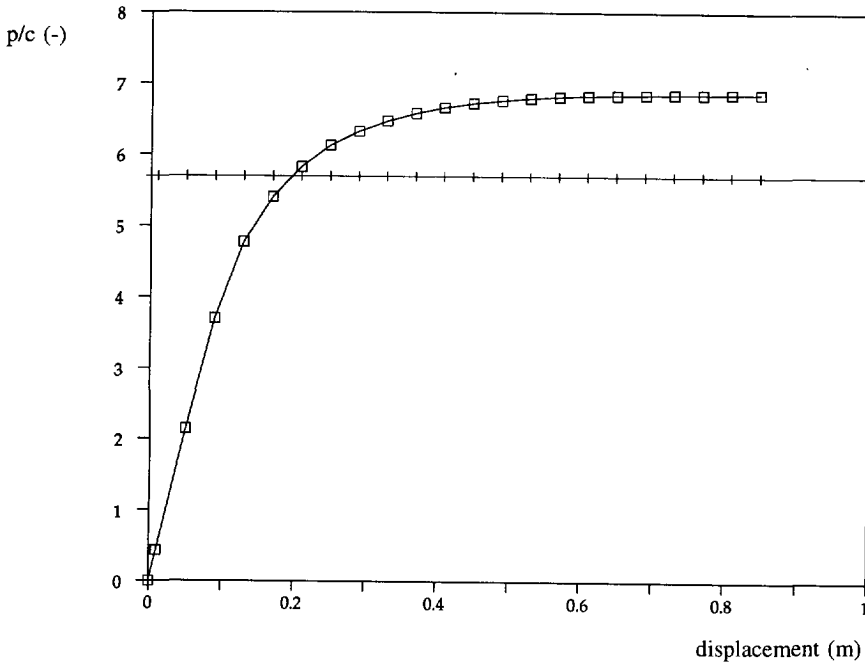
run	E (kN/m ²)	v (-)	c (kN/m ²)	ϕ ($^{\circ}$)	ψ ($^{\circ}$)	γ (kN/m ³)	K_0 (-)	E/L (-)
1	1000	0.2	5	0	0	-	-	E
2	1000	0.2	5	30	0	-	-	E
3	1000	0.2	5	40	0	-	-	E
4	1000000	0.2	5	30	0	-	-	L
5	1000000	0.2	5	30	0	-	-	E
6	1000	0.2	5	30	10	-	-	E
7	1000	0.2	5	30	10	-	-	L
8	1000	0.2	5	30	20	-	-	E
9	1000	0.0	5	30	10	-	-	E
10	1000	0.4	5	30	10	-	-	E
11	1000	0.2	5	30	0	16	0.5	E
12	1000	0.2	5	30	0	16	2.0	E

Table 3.2 Definition of runs for analysis of circular footing.

Cohesion

For the special case of frictionless behaviour the Mohr-Coulomb model reduces to the purely cohesive Tresca model. The load-displacement curve calculated is presented in figure 3.20. The theoretical bearing capacity, defined as the average vertical pressure working on the footing divided by the cohesion is: $p/c = 5.69$ (Cox et al., 1961). The difference between the numerical and the theoretical limit load is mainly caused by the finite element discretization. In an axi-symmetric configuration the nodal point at the right-hand side of the footing substantially contributes to the total

bearing capacity of the footing. Reduction of the element size around that point results in a decreasing bearing capacity towards the theoretical value (van Eekelen, 1991).



□ $E = 1000 \text{ kPa}, \nu = 0.2, c = 5 \text{ kPa}, \phi = 0^\circ, \psi = 0^\circ$
 + analytical (Cox et al., 1961)

Figure 3.20 Load-displacement curve for circular footing on cohesive soil.

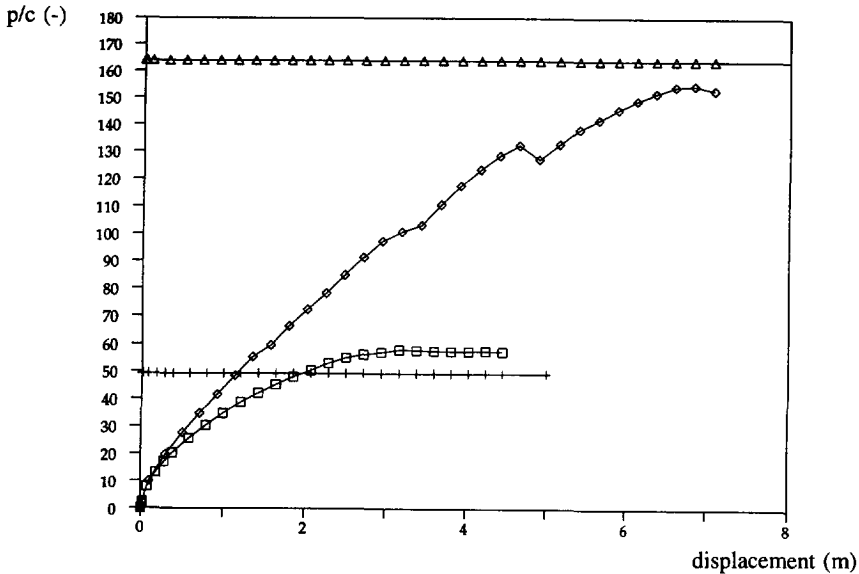
Friction

Load-displacement curves calculated for runs 2 and 3 are presented in figure 3.21. Highly non-associative material behaviour is considered: the friction angle is 30° or 40° , while the dilatancy angle is equal to zero. The analytical values for associative Mohr-Coulomb behaviour as derived by Cox et al. (1961) are presented in the same figure.

From the analysis results it was observed that converged solutions up to friction angles of about 35° could be reached easily within each incremental step. A smooth, steady state, limit load is obtained at a slightly higher level than the theoretical value. However, raising the friction angle to 40° or more yields unstable behaviour. This may be caused by the extremely high non-associativeness of the material behaviour as suggested by de Borst and Vermeer (1984).

Updated Lagrangean versus Eulerean approach

When increasing the stiffness of the material to near-infinite values, a Eulerean description of the problem tends to converge to an Updated Lagrangean approach. The total displacements of the nodal points reduce to a minimum when compared to the element size. This implies that the material flow through the elements (expressed by the convective terms as for instance given in eqn. (3.50)) is negligible.



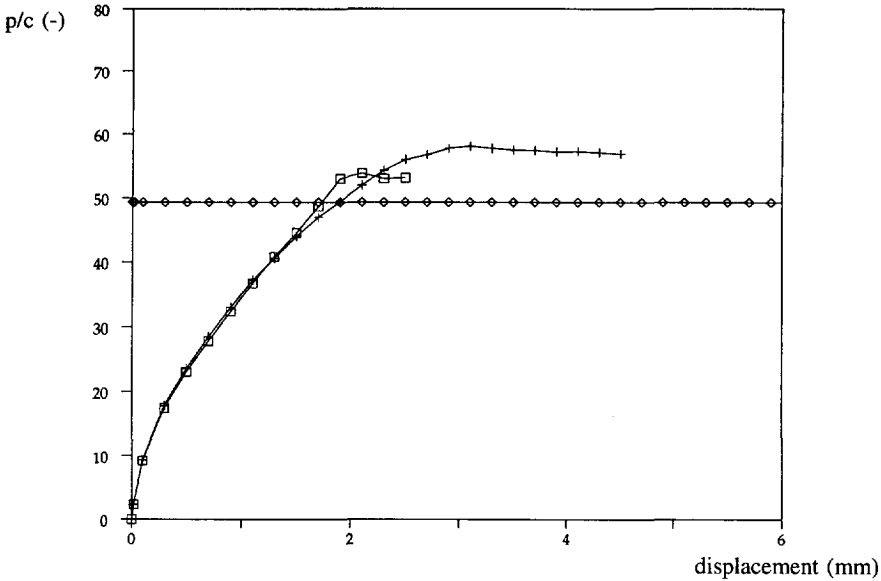
- $E = 1000 \text{ kPa}, \nu = 0.2, c = 5 \text{ kPa}, \phi = 30^\circ, \psi = 0^\circ$
- + analytical $\phi = 30^\circ$ (Cox et al., 1961)
- ◇ $E = 1000 \text{ kPa}, \nu = 0.2, c = 5 \text{ kPa}, \phi = 40^\circ, \psi = 0^\circ$
- △ analytical $\phi = 40^\circ$ (Cox et al., 1961)

Figure 3.21 Load-displacement curves for frictional soil.

The only difference therefore, between run 4 (Updated Lagrange) and run 5 (Euler) is the smoothing procedure which is related to the Eulerean approach. First local smoothing is applied to translate integration point values to nodal point values. Nodal point values are calculated by taking average nodal values from all elements connected to the particular node. Interpolation of these nodal point values gives a continuous smooth field over the complete finite element mesh.

The calculated load-displacement curves are presented in figure 3.22. Initially both curves coincide. The ultimate limit load shows a difference of about 10 %. In general it can be observed that the complete Eulerean load-displacement curve is more smooth than the Updated Lagrangean one. Evaluation of the numerical iteration

process indicated that the Eulerian calculation with smoothing is more stable than the Updated Lagrangean without.



- $E = 1000000 \text{ kPa}, \nu = 0.2, c = 5 \text{ kPa}, \phi = 30^\circ, \psi = 0^\circ$ (Updated Lagrangean)
- + $E = 1000000 \text{ kPa}, \nu = 0.2, c = 5 \text{ kPa}, \phi = 30^\circ, \psi = 0^\circ$ (Eulerian)
- ◇ analytical $\phi = 30^\circ$ (Cox et al., 1961)

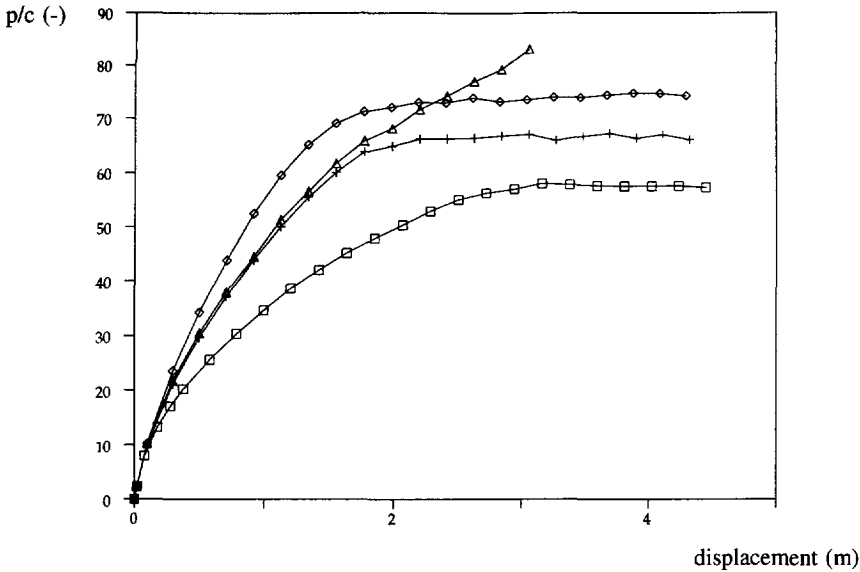
Figure 3.22 Load-displacement curves for Lagrangean and Eulerian formulation.

Dilatancy

The application of low-order enhanced B-elements in an (Updated) Lagrangean context, has shown that reasonable results could only be obtained for constant volume conditions (Nagtegaal et al., 1974; Hughes, 1987; Teunissen, 1991; de Borst and Groen, 1994). After introduction of dilatancy this element type fails to give good results. A steady state limit load cannot be obtained, since, due to locking-effects, the load-displacement curve shows unstable, steady increasing, behaviour. In the present study the same results and corresponding conclusions are found again (see figure 3.23).

However, in a Eulerian approach the locking modes are (partly) suppressed due to the smoothing procedure. The Eulerian curves indicate that for dilatancy angles equal to 10° or 20° a steady state limit load can be obtained. Increasing the dilatancy angle up to 30° (associative behaviour) divergency problems occur again. So, it can be concluded that smoothing reduces the locking problems especially in the range of small dilatancy angles. A final solution for this kind of problems can be found in the appli-

cation of high order elements (de Borst and Vermeer, 1984) or, may be, in the application of low order elements in combination with enhanced assumed strain fields (de Borst and Groen, 1994).



- $E = 1000 \text{ kPa}, \nu = 0.2, c = 5 \text{ kPa}, \phi = 30^\circ, \psi = 0^\circ$ (Eulerian)
- + $E = 1000 \text{ kPa}, \nu = 0.2, c = 5 \text{ kPa}, \phi = 30^\circ, \psi = 10^\circ$ (Eulerian)
- ◇ $E = 1000 \text{ kPa}, \nu = 0.2, c = 5 \text{ kPa}, \phi = 30^\circ, \psi = 20^\circ$ (Eulerian)
- △ $E = 1000 \text{ kPa}, \nu = 0.2, c = 5 \text{ kPa}, \phi = 30^\circ, \psi = 10^\circ$ (Updated Lagrangean)

Figure 3.23 Load-displacement curves for circular footing on frictional-dilatant soil.

Poisson's ratio

Load-displacement curves computed for different values of ν are shown in figure 3.24. It can be seen, that, although the initial slope of the load-displacement curves is different, the ultimate bearing capacity is hardly influenced. Furthermore, it was observed that it was very difficult to reach converged solutions for highly non-associative material behaviour in combination with large values of ν , i.e. larger than 0.48.

Initial state of stress

In order to study the effect of the initial state of stress in general and the lateral pressure ratio K_0 in particular, two runs have been performed. The initial vertical stress is identical, while the horizontal stress is half (run 11) or twice (run 12) the vertical stress. The corresponding load-displacement curves are visualized in figure 3.25. A large value for K_0 shows some global softening behaviour after reaching the peak load. The steady state limit load, however, is pretty much the same.

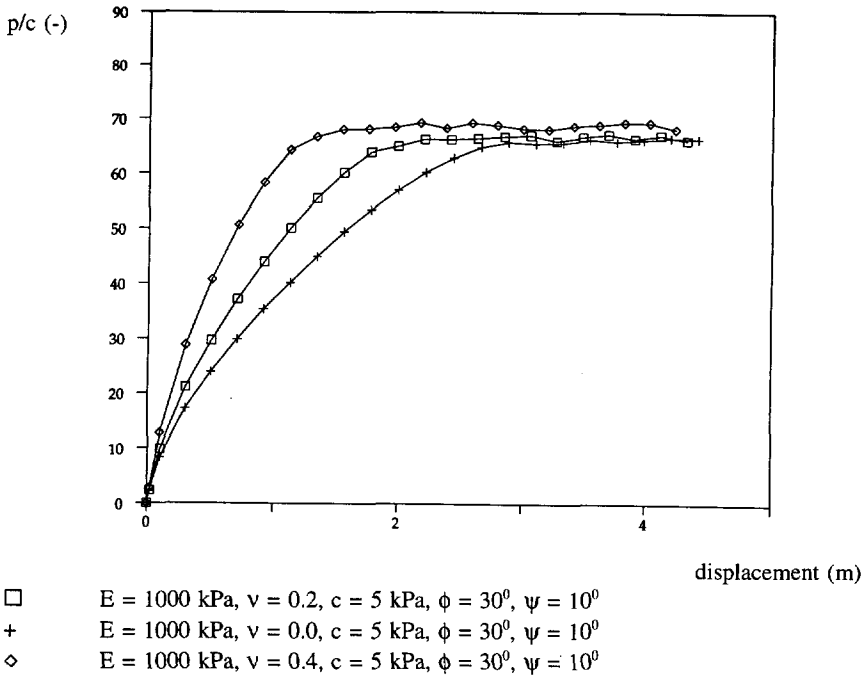


Figure 3.24 Load-displacement curves for different values of Poisson's ratio.

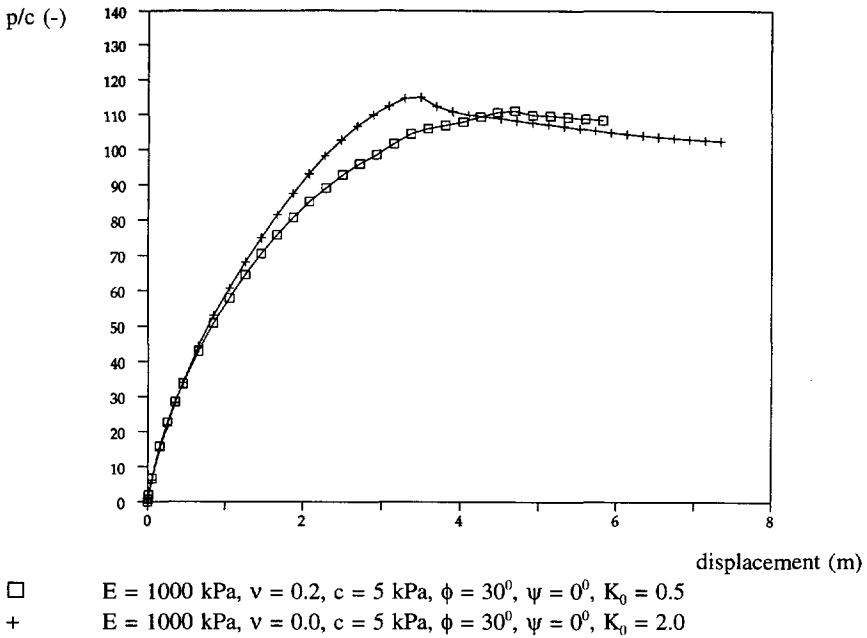


Figure 3.25 Load-displacement curves for different values of K_0 .

3.5.3 In conclusion

Based on the results presented in the foregoing section, the following conclusions can be drawn:

- The four-noded enhanced B element can be used adequately to study limit state behaviour in axi-symmetric configurations under constant volume conditions. Unstable behaviour was observed for extremely non-associative behaviour ($\phi - \psi \geq 40^\circ$).
- When introducing dilatancy the element does not work in a conventional (Updated) Lagrangean context without the application of smoothing techniques. In a Eulerean approach (including smoothing) reasonable results can be obtained for limited values of ψ (up to, say, 10°).

Looking from the other side, i.e. the material to be modelled, it can be concluded that the non-associativeness of the soil is at most equal to 30° or 35° . Under normal conditions dilatancy angles are limited to 10° or 15° . Therefore it can be concluded that the numerical procedure (Eulerean approach incl. smoothing) in combination with the four-noded enhanced B element and non-associative Mohr-Coulomb behaviour can be used to perform limit state analyses under axi-symmetrical conditions.

Appendix 3.A: Non-linear elasticity

Experimental results indicate that the elastic behaviour of soil is stress-dependent and varies both with the mean normal stress and the deviatoric stress. A widely used model is based on the initial slope of the stress-strain curve for triaxial compression (Janbu, 1963 and Ko and Scott, 1967). The initial tangent modulus may be expressed as a power function of the isotropic, effective confining pressure σ_3' :

$$E_i = K_i p_a \left[\frac{\sigma_3'}{p_a} \right]^n \quad (3.A.1)$$

in which p_a is the atmospheric pressure and K_i is a modulus number, ranging from 50 to 500 (Janbu, 1963). He found for sand values of n ranging from 0.35 to 0.55.

Zytynski et al. (1978) pointed out that such a model results into violation of the principle of conservation of energy. Therefore Lade and Nelson (1987) developed a model that neither generates nor dissipates energy in closed-loop stress paths. In his model Poisson's ratio is constant and Young's modulus is expressed as a function of the first invariant of the stress tensor I_1 and the second invariant J_2 :

$$E_i = M_i p_a \left[\frac{I_1^2}{p_a} + R \frac{J_2}{p_a^2} \right]^\lambda \quad (3.A.2)$$

Although eqn. (3.A.1) lacks a full theoretical base, this relation is commonly applied, since a), this model is able to simulate the behaviour measured in triaxial tests and b), there is a large amount of experience in determination of parameters for this model. The deformation of soil can also be expressed by using the bulk-modulus, related to the hydrostatic stress component, and the shear-modulus, related to the deviatoric component. This leads to expressions similar to the relation of eqn. (3.A.1). Vermeer (1978), for instance, proposes the following relation for the shear modulus:

$$G = G_0 \left[\frac{p}{p_0} \right]^{1-\beta}, \quad 0.33 < \beta < 0.5 \quad (3.A.3)$$

In this equation G_0 represents the shear modulus at a certain isotropic stress level p_0 . Poisson's ratio is assumed to be stress independent.

Appendix 3.B: On the critical state of sand

Since the pioneering work of Casagrande (1936), the existence of a critical void ratio is a point of discussion. An important step forward was the introduction of critical state soil mechanics by Roscoe et al. (1958). Although after that time, most attention was paid to the behaviour of clay, some attention was also given to sands (Stroud, 1971). However, up to now, the application of the critical state concept to sands is still a point of discussion. An important drawback, especially in former days, had to do with the fact that it proved to be very difficult to measure the critical state line, relating the critical void ratio of a specific sand-type to the logarithm of the mean isotropic stress level. Attempts resulted into a large scatter of the test results. However, modern laboratory techniques can be used nowadays and some of the problems have been solved (Castro, 1969).

The critical state line was assumed to be straight in the work carried out by Been and Jefferies (1985). This relation is graphically shown in figure 3.B.1.

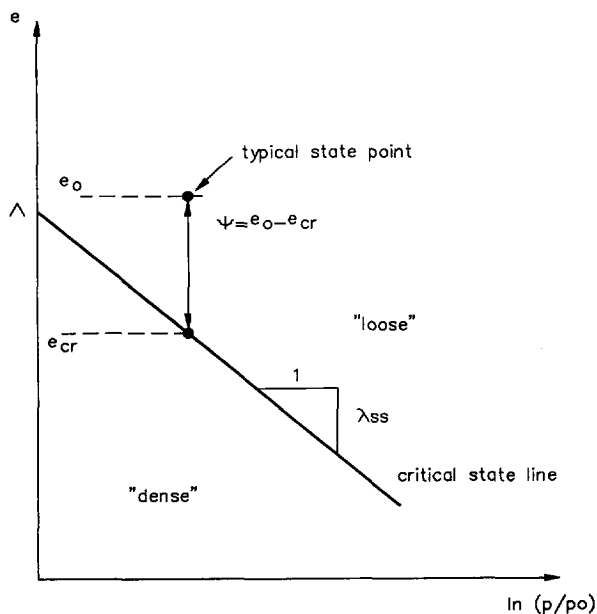


Figure 3.B.1 Definition of critical state line and state parameter (Been and Jefferies, 1985).

They also introduced the concept of the state parameter Ψ , defined as the difference between the actual void ratio and the critical void ratio (at the same mean isotropic stress level). Loose test specimens, located in the upper right part of the figure, will contract during loading (the state-parameter is defined positive), whereas dense

samples, located in the lower left part, will dilate during loading. The volume-increase or -decrease stops when the critical state line has been reached. The critical state line can be written in the following (widely accepted) form:

$$e_{cr} = \Lambda - \lambda_{ss} \ln \left[\frac{p}{p_0} \right] \quad (3.B.1)$$

However, recent test results have given rise to the suggestion, that the critical state line is not straight but rather bi-linear or curved (Been, Jefferies and Hackey, 1991). Some results of the extensive measurement program published in that paper are presented in figure 3.B.2. Crushing of grain particles at very high stress levels will be one of the most important reasons to explain this phenomenon. The state parameter concept has also been used by Been et al. (1986) as a framework for the interpretation of cone penetration data.

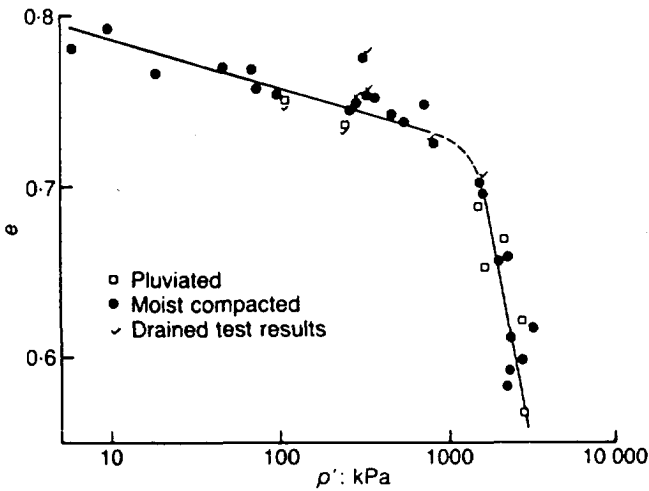


Figure 3.B.2 Critical state line for a number of different sands (Been, Jefferies and Hackey, 1991).

However, in spite of all this interesting work the existence of a critical void ratio is still a point of discussion. Questions, for instance, about the relation between the critical void ratio and the loading history, have not yet been answered conclusively.

Appendix 3.C: Potential field around a circular line-source

The potential field around a circular line-source in an infinite 3-dimensional space can be derived analytically as follows.

The hydraulic head (h [m]) caused by a point source is:

$$h(r,z) = \frac{Q}{4\pi k d} \tag{3.C.1}$$

in which Q is the rate of discharge [m^3/s], k is the permeability [m/s] and d is the distance from the point source [m], defined by:

$$d = \sqrt{r^2 + z^2} \tag{3.C.2}$$

r being the radial distance and z the vertical distance.

Eqn. (3.C.1) can be integrated over a circle with a radius R to give a circular line source with a total rate of discharge equal to Q [m^3/s]. Using a circular cylindrical coordinate system and assuming that the location of the circular source is given by ($r=R, z=0$), then the increment of the hydraulic head at an arbitrary location (r, z) can be derived as follows (see also figure 3.C.1):

$$h(r,z) = \frac{Q}{4\pi k} \frac{1}{2\pi} \int_0^{2\pi} \frac{d\alpha}{\sqrt{r^2 + R^2 - 2rR\cos\alpha + z^2}} \tag{3.C.3}$$

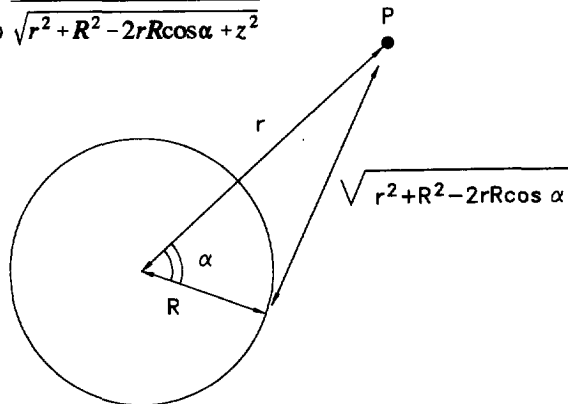


Figure 3.C.1 Distance of arbitrary point P to circular source.

Equation (3.C.3) can be worked out analytically to give:

$$h(r,z) = \frac{Q}{4\pi^2 k} \int_0^\pi \frac{d\alpha}{\sqrt{(R+r)^2 + z^2 - 2rR(1 + \cos\alpha)}} \quad (3.C.4)$$

$$h(r,z) = \frac{Q}{4\pi^2 k} \int_0^\pi \frac{d\alpha}{\sqrt{(R+r)^2 + z^2 - 4rR\cos^2(\frac{\alpha}{2})}} \quad (3.C.5)$$

$$h(r,z) = \frac{Q}{2\pi^2 k} \frac{1}{\sqrt{(R+r)^2 + z^2}} K(m) \quad (3.C.6)$$

in which $K(m)$ is an elliptic integral:

$$K(m) = \int_0^{\frac{\pi}{2}} \frac{d\beta}{\sqrt{1 - m \sin^2 \beta}} \quad ; \quad \beta = \frac{\pi}{2} - \frac{\alpha}{2} \quad (3.C.7)$$

and:

$$m = \frac{4rR}{(r+R)^2 + z^2} \quad (3.C.8)$$

The integral $K(m)$ can be approximated by (Abramowitz and Stegun, 1970):

$$K(m) = A(m) + B(m) \ln\left(\frac{1}{1-m}\right) + \epsilon(m) \quad (3.C.9)$$

where:

$$A(m) = a_0 + a_1(1-m) + a_2(1-m)^2 + a_3(1-m)^3 + a_4(1-m)^4 \quad (3.C.10)$$

and:

$$B(m) = b_0 + b_1(1-m) + b_2(1-m)^2 + b_3(1-m)^3 + b_4(1-m)^4 \quad (3.C.11)$$

Introducing the following values for the coefficients a_i and b_i , the error $\varepsilon(m)$ is less than $2 \cdot 10^{-8}$ in the whole domain.

a_0 :	1.38629436112	b_0 :	0.5
a_1 :	0.09666344259	b_1 :	0.12498593597
a_2 :	0.03590092383	b_2 :	0.06880248576
a_3 :	0.03742563713	b_3 :	0.03328355346
a_4 :	0.01451196212	b_4 :	0.00441787012

4. Analysis of cone penetration

4.1 Introduction

The cone penetration test is becoming increasingly popular as an in-situ test for site investigation and geotechnical design (Robertson and Campanella, 1986). A steel cylindrical bar with a diameter of 35.7 mm and a cone-shaped tip is pushed into the subsoil at a constant penetration rate of 2 cm per sec. A cross-section of 10 cm² and a tip-angle of 60° is generally accepted as standard and has been specified in the European and American Standards (ISSMFE, 1977 and ASTM, 1979). The friction sleeve, located above the conical tip has a standard area of 150 cm² and an outer diameter of 35.7 mm. During penetration the tip reaction force and the skin friction are registered, while in the piezo-version of the penetrometer also the generated excess pore water pressure is measured at a location either just above the shoulder of the cone (see figure 4.1) or at a position on the conical tip.

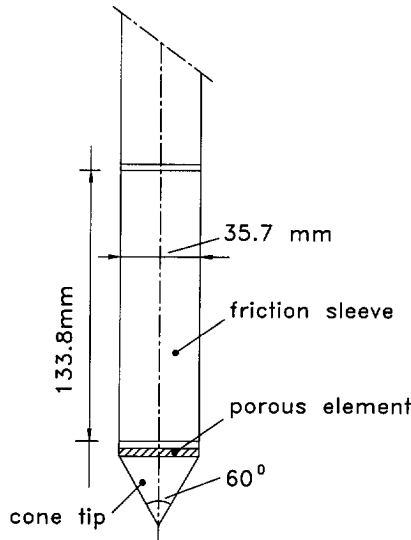


Figure 4.1 Electric piezo-friction-cone penetrometer tip.

As outlined in chapter 2, a large number of investigators have studied the mechanics of the penetration process. In this chapter the numerical model described in chapter 3 is used to analyse the cone penetration problem. Model tests have been carried out to validate the results of the model. Based on the results of this analysis some directives are given to improve the interpretation of the measured data. After introduction of the numerical model, results will be given for penetration in clay, sand and layered strata.

4.2 Numerical model

4.2.1 Eulerean approach of penetration process

In contrast with a Lagrangean type model, in a Eulerean type model, the finite element mesh is fixed in space, while the material streams through the elements. A schematic view of such a Eulerean model is presented in figure 4.2. The cone is modelled as a fixed boundary and interface friction is taken into account between this boundary and the soil. At the start of the analysis the initial state of stress is defined by the soil weight and the lateral pressure ratio at rest. So, in fact the cone is introduced into a pre-bored hole. The penetration process itself is initiated by applying incremental material displacements at the lower boundary of the mesh. Material streams upward through the mesh. As indicated in figure 4.2 a material particle "A", originally located underneath the tip of the cone, moves upward and is compressed around the shaft of the cone, arriving at, for instance, point "B". The corresponding stress and strain fields around the cone are calculated. The calculation is stopped when a steady state is reached with respect to the stress and strain distribution in the complete finite element mesh.

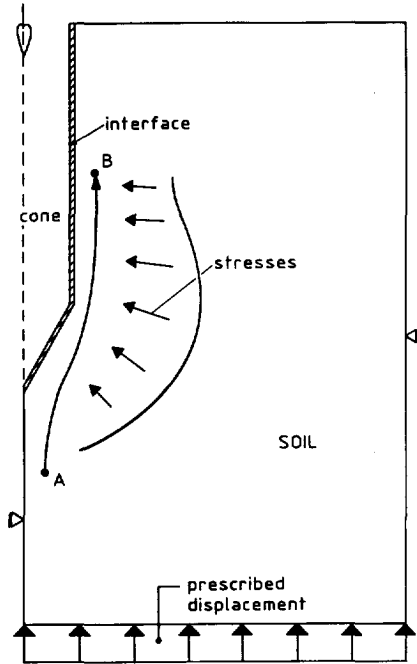


Figure 4.2 Schematic view of Eulerean approach of cone penetration problem.

An important factor in the analysis of a penetration problem is the width of the calculation area. Especially in dilatant sand it is important to be aware of the fact that unrealistic stress build-up may be calculated if the diameter of the axi-symmetric model is too small. Experimental researchers, who carried out laboratory tests with controlled stress and density conditions in sand, hold the view that a chamber with a diameter of at least 20 - 25 times the cone diameter is needed, to eliminate boundary effects (Veismanis, 1974; Chapman, 1974; Smits, 1977; Houlsby and Hitchman, 1988). To account for this effect, in the numerical model the "column of elements" located at the right-hand side of the mesh has a reduced stiffness. In these particular elements the influence up to infinity is concentrated. The corresponding stiffness is calculated using the cylindrical cavity expansion theory (Vesic, 1972). In a first step the radial stress and displacement field around an expanding cylinder (from zero radius to cone radius) in an infinite $c-\phi$ material is calculated. The radial displacement at the left-hand boundary of the "column of elements" is called u_L and the radial stress σ_L . In a separate analysis the required stiffness of those elements is determined in such a way that a radial stress σ_L working on the elements yields the same displacement u_L .

4.2.2 Finite elements

The application of conventional eight-noded quadrilateral elements with full (9-point) and reduced (4-point) integration failed to give good results (de Borst, 1982; van den Berg and Vermeer, 1988). A steady state limit load could not be obtained. Even for frictionless behaviour the load-displacement curve showed a steady increasing behaviour, caused by locking effects. These problems relate to the fact that the deformation state of an elastic perfectly plastic material is highly constrained at limit loads. To decrease the number of constraints or, better, to increase the ratio "degrees of freedom - number of constraints", four-noded elements are used, in which the constant volume condition is imposed for the average deformation of the element rather than for all four Gaussian points (Nagtegaal, 1974; Hughes, 1987; Teunissen, 1991).

To account for the contact-frictional interface behaviour between penetrometer and soil, zero-thickness four-noded interface elements are incorporated in the model. To avoid stress-oscillations and unrealistic stress build-up at the corner point between tip and shaft, a lumped integration scheme has been utilized (Schellekens, 1992). To get a smooth stress state around the corner point, the shape of the cone is rounded. Figure 4.3 shows a detail of the soil and the interface elements around the tip of the cone.

4.2.3 Initial stresses and material parameters

Since (a) deep penetration is considered (depth of cone-tip greater than, say, 10 times the cone-diameter) and (b) in the model only a limited area around the cone is mo-

delled by finite elements, the gradient of the vertical stress is of secondary importance and a homogeneous initial state of stress can be introduced into the model before starting the penetration simulation. This state of stress is characterized by $\sigma_{v,0}$, the initial vertical stress at a depth corresponding to the cone-tip, and the lateral pressure ratio K_0 , defined as the ratio of the initial horizontal stress $\sigma_{h,0}$ and $\sigma_{v,0}$.

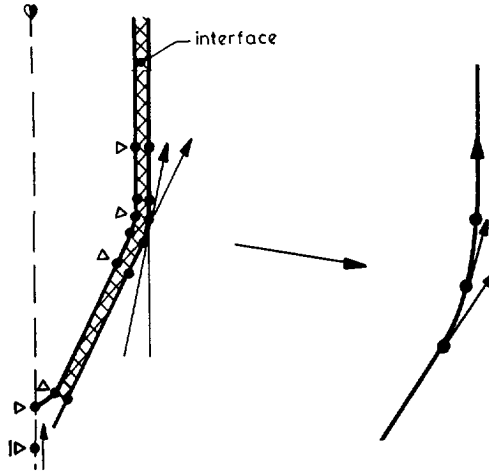


Figure 4.3 Detail of interface elements and boundary conditions.

The undrained behaviour of clay is modelled by the linear elastic perfectly plastic Tresca model with parameters Young's modulus E , Poisson's ratio ν and the undrained shear strength c_u . The material behaviour of sand is simulated by the hardening-softening Drucker-Prager or Mohr-Coulomb model (paragraph 3.4.3) with parameters Young's modulus E , Poisson's ratio ν , friction angle at constant volume $\phi_{c,v}$, cohesion c , initial dilatancy angle ψ_0 and the softening parameter ξ . The interface friction between soil and cone is modelled by the Coulomb friction model:

$$\tau_{\max} = a + \sigma_n \tan \delta \tag{4.1}$$

where a is the adhesion, σ_n is the normal stress acting on the interface and δ is the interface friction angle. The angle δ is equal to zero for undrained "steel-clay" interface friction.

4.2.4 Validation of the model

A number of test runs have been performed to validate the model. After a basic calculation has been carried out, the influence of the coarseness of the mesh in both

perfectly plastic and softening material is analyzed as well as the influence of the boundary condition at the shoulder of the cone.

Basic calculation

The finite element mesh used for the basic calculation consists of 360 elements to model the soil and is visualized in figure 4.4. The cone is assumed to be fully smooth. For this particular case, the perfectly plastic Drucker-Prager model has been applied with the following parameter values: $E = 5000$ kPa, $\nu = 0.3$, $\phi = 30^\circ$, $\psi = 0^\circ$ and $c = 2$ kPa. The initial vertical stress $\sigma_{v,0} = 35$ kPa, whereas $K_0 = 1.0$.

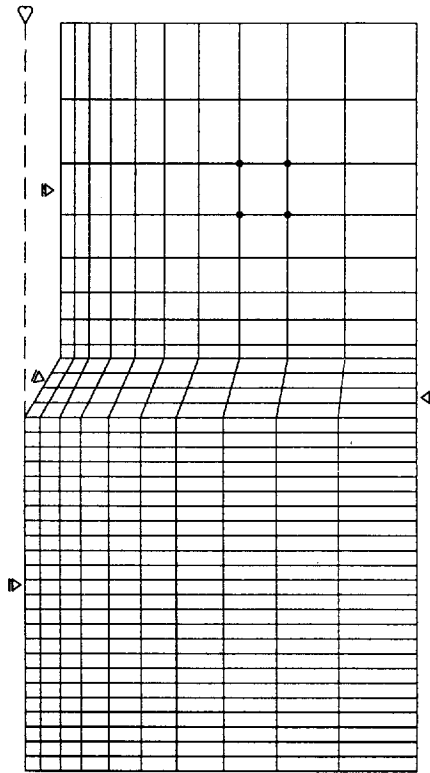
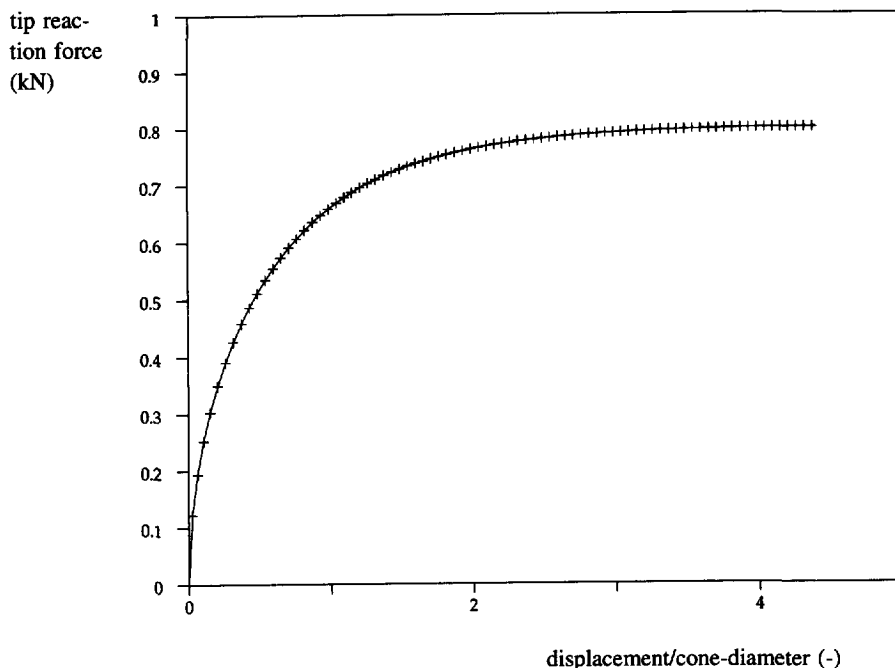


Figure 4.4 Finite element mesh for basic calculation.

The loading consists of a prescribed vertical material displacement at the bottom of the mesh and a global unbalance criterion has been used equal to 0.1 %. The calculation has been carried out using a tangential stiffness approach, updated before each iteration. Since the material behaviour is non-associative, a non-symmetric stiffness matrix occurs and has to be solved. The load-displacement curve obtained is shown in figure 4.5. An automatic step-size correction scheme has been applied: the step-

size is automatically increased or decreased by a factor two, depending on the rate of convergence. After the fourth step, the maximum (prescribed) step-size of 2 mm (i.e. 0.0556 times the cone diameter D) is reached. To reach a converged solution 4 to 5 iterations are needed. The complete run consists of 80 incremental steps. It can be seen that after a displacement of about $3D$ a steady state is reached with respect to the tip reaction force.



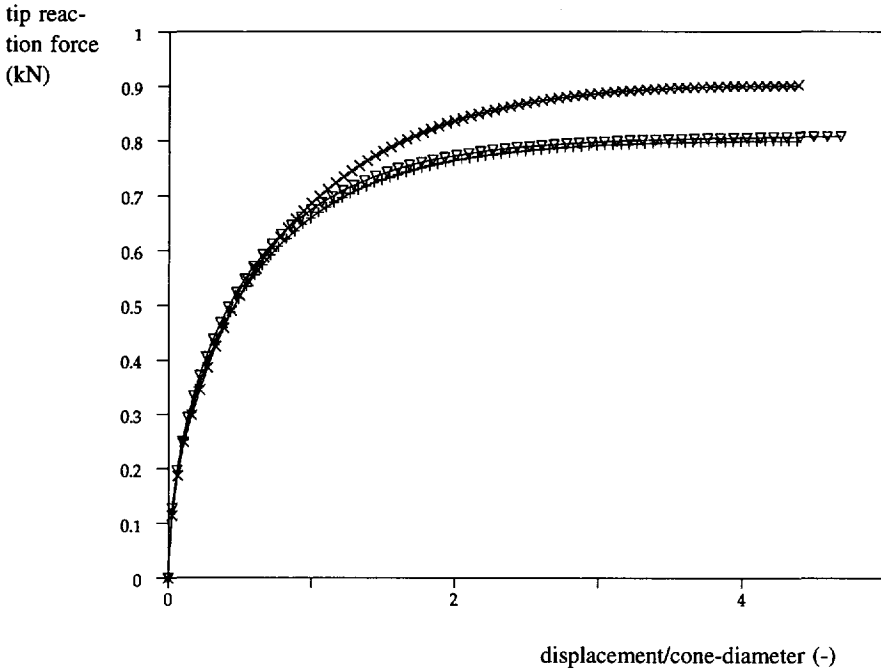
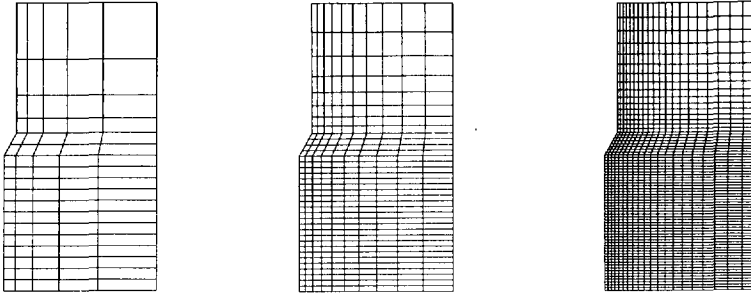
□ $E = 5000 \text{ kPa}$, $\nu = 0.3$, $c = 2 \text{ kPa}$, $\phi = 30^\circ$, $\psi = 0^\circ$

Figure 4.5 Load-displacement curve for basic calculation.

Coarseness of the mesh

In order to study the effect of the coarseness of the finite element mesh, two additional calculations have been carried out. The basic calculation is repeated twice; once using a mesh with a quarter of the number of elements (90 instead of 360) and another using four times the element number (1440 instead of 360). The calculated load-displacement curves are shown in figure 4.6.

The difference between 90 and 360 elements is about 12 %, whereas the difference between 360 and 1440 elements is negligible. Based on this, the 360-element mesh will be used in the subsequent paragraphs.



+ 360 elements x 90 elements v 1440 elements

Figure 4.6 Load-displacement curves for 90, 360 and 1440 elements.

Modelling the shoulder of the cone

Due to axi-symmetry, the contribution of the shoulder of the cone to the total reaction force dominates the contribution of the area close to the sharp tip of the cone. This is demonstrated by the following set of calculations, in which the boundary condition at the discontinuity between the tip and the shaft is varied. Three different assumptions are shown in figure 4.7. In model A the soil at the shoulder is forced to move in a vertical direction, whereas in model C the soil continues to move in a direct line with the slope of the cone tip. In model B the soil is forced to move in a direction in between.

The corresponding load-displacement curves for the finite element meshes consisting of 90 and 360 elements respectively are shown in the same figure. As can be seen, mesh-refinement reduces the influence of the boundary condition. The difference between the reaction force for model A and for model B can be interpreted as the result of a sort of "reduced fictitious cone diameter". Model A can be regarded as a cone with a radius equal to the radius according to model B minus half the element width at the left-hand side of the shoulder point. Following the same line of reasoning, in model C the fictitious radius can be interpreted to be enlarged by half the element width at the right-hand side of that point.

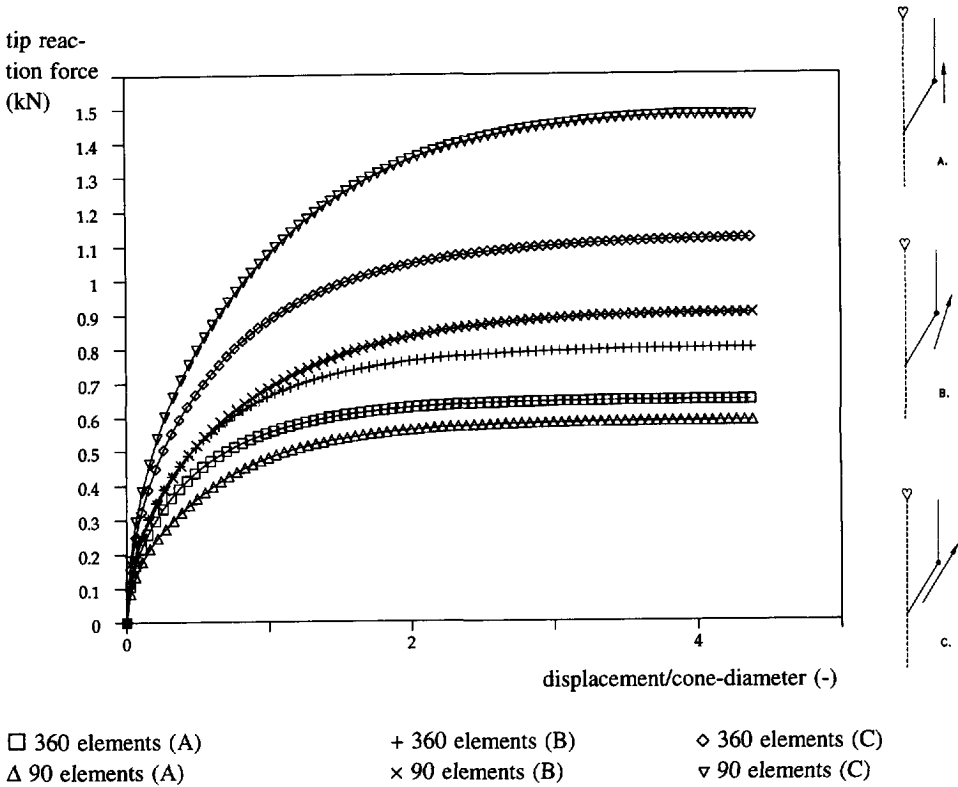


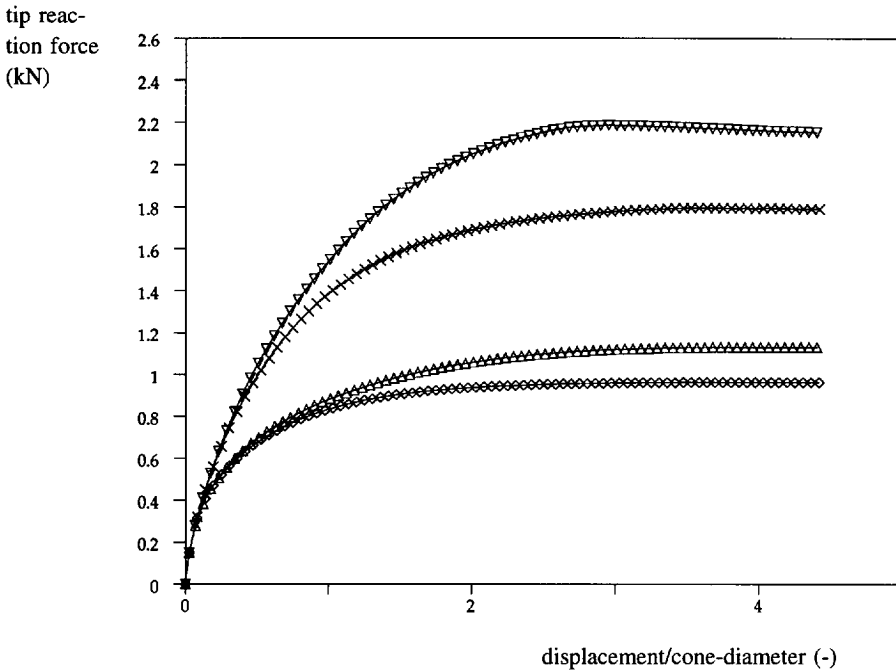
Figure 4.7 Influence boundary condition at the shoulder of the cone.

Strain softening and mesh-objectivity

Classical continuum models, i.e. models that do not incorporate an internal length scale, suffer from mesh-dependence when strain-softening models are employed in numerical analyses (de Borst and Mühlhaus, 1992). When a strain localization zone develops, the governing differential equations lose ellipticity. To regularize the equations after localization, in recent research it has been suggested that there are at least three different approaches: (1) Cosserat theory (Mühlhaus and Vardoulakis,

1987), (2) gradient plasticity theory (Mühlhaus and Aifantis, 1991) and, (3) rate-dependent models, each of them having its own advantages and disadvantages (Sluys, 1992).

In order to quantify the effect of mesh-dependency for the specific case of cone penetration in softening material, four calculations have been performed using the 90 and 360 element meshes. In two runs the material behaviour is assumed to be perfectly plastic, whereas in the other runs the softening model (paragraph 3.4.3) is used. The initial vertical stress is 35 kPa and K_0 is equal to 1.0. The results are shown in figure 4.8.



- ◇ $E = 5000$ kPa, $\nu = 0.3$, $\phi_{cv} = 30^\circ$, $\psi_0 = 10^\circ$, $c = 2$ kPa and $\xi = 0.072$ (360 elm.)
- △ $E = 5000$ kPa, $\nu = 0.3$, $\phi_{cv} = 30^\circ$, $\psi_0 = 10^\circ$, $c = 2$ kPa and $\xi = 0.072$ (90 elm.)
- × $E = 5000$ kPa, $\nu = 0.3$, $\phi = 38.3^\circ$, $\psi = 10^\circ$ and $c = 2$ kPa (360 elm.)
- ▽ $E = 5000$ kPa, $\nu = 0.3$, $\phi = 38.3^\circ$, $\psi = 10^\circ$ and $c = 2$ kPa (90 elm.)

Figure 4.8 Load-displacement curves for perfectly plastic and strain softening material (90 and 360 elements).

It can be seen that the difference between the two perfectly plastic curves is pretty much the same as the difference between the two softening curves. The ratio "limit load for 360 elements over limit load for 90 elements" is 0.83 (perfectly plastic) and 0.85 (softening model). Based on this, the conclusion is justified that for the cone penetra-

tion problem there is sufficient mesh-objectivity, at least within the range of parameters occurring in geotechnical practice. The reason is that most of the material softening takes place during the phase in which the total reaction force working on the cone increases and in which localization does not occur yet.

4.3 Penetration in clay

4.3.1 Introduction

Under undrained conditions, clay can be modelled as a purely (incompressible) cohesive material. The simplest formula used in engineering practice relates the cone resistance to the undrained shear strength. This relation originates from the bearing capacity theory (see paragraph 2.2.1).

$$q_c = N_c c_u + \sigma_{v0} \tag{4.2}$$

where:

- q_c cone resistance
- N_c cone factor
- c_u undrained shear strength
- σ_{v0} total overburden pressure

Most reported values for N_c are in the range between 5 and 28 (Baligh, 1985), between 8 and 30 (van Impe, 1986, see figure 4.9) or between 10 and 25 (Smith and Chow, 1987).

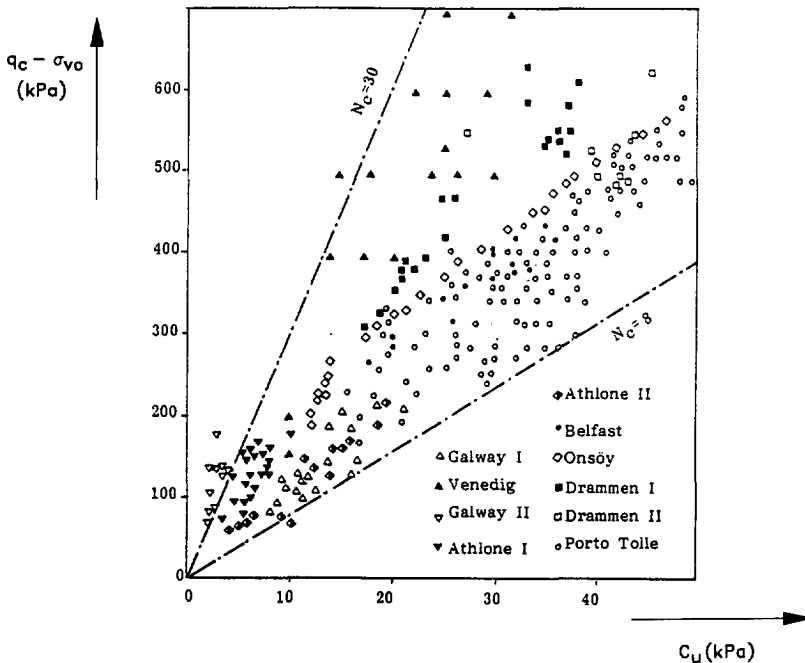


Figure 4.9 Relation between modified cone resistance ($q_c - \sigma_{v0}$) and undrained cohesion (Van Impe, 1986).

This wide range makes clear that the cone resistance is not only a function of the shear strength but also of other parameters such as the roughness of the cone, the stiffness of the clay and the initial state of stress. De Ruiter (1982) suggests that for normally consolidated clays typical values for the cone factor N_c are in the range between 10 and 15 and for overconsolidated clays 15 to 20.

As has been discussed in more detail in chapter 2, the theoretical models can be subdivided into a number of different approaches. A first approach is the bearing capacity method based on the original work by Prandtl (1921). Referring to the axi-symmetric problem, Meyerhof (1961) gives results for the relation between q_c and c_u . Also Luger et al. (1982b) and Koumoto and Kaku (1982) present results for the cone factor depending on the cone angle, the shaft adhesion α_s and the adhesion at the tip of the cone α . For a cone with a 60° top angle, the cone factor ranges from about 7.5 for a completely smooth cone to about 11.5 for a fully rough one (see table 4.1).

α_s/c_u	0.0	0.5	1.0
$\alpha/c_u = 0.0$	7.57		
$\alpha/c_u = 0.5$	8.84	9.76	
$\alpha/c_u = 1.0$	9.86	10.76	11.49

Table 4.1 Cone factor N_c for cone with a 60° top angle. Influence of adhesion to cohesion ratio on shaft (α_s/c_u) and on cone tip (α/c_u).

An alternative approach refers to the cavity expansion theory (Vesic, 1972). In the case of elasto-plastic behaviour the cone factor becomes a function of both the undrained shear modulus and the undrained shear strength of the clay:

Spherical cavity expansion:

$$N_c = 1.33 \left(1 + \ln \frac{G}{c_u} \right) \quad (4.3)$$

Cylindrical cavity expansion:

$$N_c = 1.00 \left(1 + \ln \frac{G}{c_u} \right) \quad (4.4)$$

In these formulas G/c_u is called the rigidity index, often referred to as I_r .

The third approach is based on the work done by Baligh (1975). The penetration process is simplified by dividing the cone resistance into two contributions. The first contribution is the work required to give the tip of the cone a virtual vertical displacement. The second part is the work done to expand the soil around the shaft of the cone in the horizontal (radial) direction. Then the cone factor becomes:

$$N_c = 11 + 1.00(1 + \ln \frac{G}{c_u}) \quad (4.5)$$

Along the same line of reasoning, van den Berg and Vermeer (1988) and Vermeer and van den Berg (1988) arrived at the following equation:

$$N_c = N_p + 1.00(1 + \ln \frac{G}{c_u}) + (K_0 - 1) \frac{\sigma_{v0}}{c_u} \quad (4.6)$$

Eqn. (4.6) agrees to some extent with equation (4.5) as proposed by Baligh (1975). Van den Berg and Vermeer (1988) introduce the partial cone factor N_p and they recommend to use a value according to table 4.1, ranging between 7.6 and 11.5 depending on the roughness of the cone, whereas Baligh (1975) uses a constant value for the partial cone factor N_p equal to 11 for a 60° sharp cone. Furthermore Baligh does not introduce the lateral pressure ratio K_0 to assess the initial horizontal stress σ_{h0} .

In practice penetrometers are neither smooth nor fully rough, but the adhesion is about half the cohesion of the clay. For such practical situations Luger et al. (1982) report a value of about 10 for the partial cone factor, which is ten percent lower than Baligh's value of 11. Using $N_p = 10$ and $K_0 = 1$, the total cone factor according to eqn. (4.6) becomes for:

	G/c_u	N_c
soft clay	50	14.9
stiff clay	300	16.7

Table 4.2 Cone factor N_c for soft and stiff clay according to Van den Berg and Vermeer (1988).

These values are well within the empirical range between 10 and 20. The lower bound of 10 will be reached when K_0 is well below unity. The upper bound of 20 may be reached for large values of K_0 .

An alternative approach is the simple pile approach according to Baligh (1985, 1986) and Whittle (1992). Working out the equations for this model yields the following relation between the cone factor and the rigidity index (G/c_u):

$$N_c = 2.00(1 + \ln \frac{G}{c_u}) - 0.49 \tag{4.7}$$

The problem of cone penetration has also been analysed by finite element methods. One of the first computations making use of a small-strain finite element formulation were performed by De Borst and Vermeer (1982). Results were obtained for a penetrometer with a smooth shaft. The cone factor was found to be 10. A similar analysis using the same type of elements was performed by Griffiths (1982). He arrived at a cone factor of about 9.5.

Figure 4.10 shows the relation between the cone factor and the rigidity index according to different models. Line "a" corresponds to the models proposed by Baligh (1975) and van den Berg and Vermeer (1988) for $K_0 = 1.0$ and $N_p = 11$ (eqn. (4.5) and (4.6)). The relation according to the simple pile approach is given by line "b" (eqn. (4.7)). Line "c" follows from bearing capacity models and small-strain finite element models, whereas line "d" corresponds to the spherical cavity expansion theory (eqn. (4.3)) and line "e" to the cylindrical expansion solution (eqn. (4.4)).

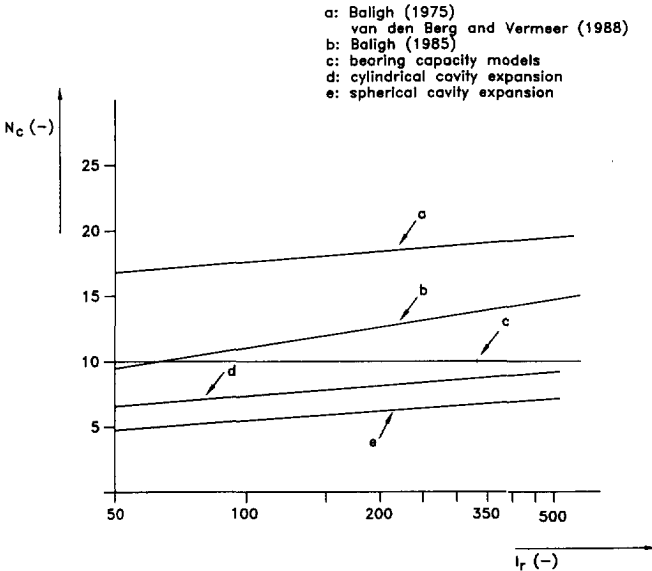


Figure 4.10 Relation between cone factor N_c and rigidity index I_r (G/c_u) according to different models.

Comparing the contents of figure 4.9 (experimental results) to those of figure 4.10 (theoretical results) it is concluded that cone factors greater than, say, 18 cannot be calculated by the models. In the literature a number of potential explanations has been given, for instance: heavily overconsolidated clay and thus extremely large values for K_0 (van den Berg and Vermeer, 1988), soil viscosity (Harder, 1989) or (partially) drained behaviour (Smits, 1977).

4.3.2 Numerical analysis

Introduction

Cone factors derived by small-strain finite element computations appeared to be independent of the stiffness of the soil. Values have been calculated of about 10 (de Borst and Vermeer, 1982; Griffiths, 1982). In these analyses the cone has been introduced into a pre-bored hole, with the surrounding soil still in its in-situ stress state. An incremental plastic collapse calculation is carried out and the collapse value identified as the indentation pressure. This interpretation is not entirely correct. During the real penetration of the cone, high lateral and vertical stresses develop adjacently to the shaft of the cone. Soil initially located underneath the tip of the cone is compressed radially outside to make room for the cone. So there is an important difference between a plastic collapse solution and a steady state penetration mechanism.

In order to erase the incorrect initial conditions a large deformation analysis is needed to simulate a displacement of at least two or three times the diameter of the cone. Such a large displacement would be enough to give a realistic build-up of the shaft pressure due to the effect that soil initially located underneath the tip of the cone has to be compressed around the shaft to make room for the cone. Accordingly, small-strain analyses only give results for the partial (stiffness-independent) cone factor, the first term in equation (4.6). To assess the full cone factor the stiffness dependent part of equation (4.6) is also needed. Then a large-strain analysis is necessary.

Definition of runs

In order to investigate the influence of the stiffness of the clay, the roughness of the cone and the initial state of stress, a number of calculations have been performed. The finite element mesh (360 elements) is presented in figure 4.4. For the simulations of a smooth cone the boundary condition at the shoulder of the cone is taken according to model B (figure 4.7). The constitutive behaviour of the clay is modelled by the purely cohesive Tresca material model. Table 4.3 presents the characteristic data.

run	E (kPa)	ν (-)	c_u (kPa)	a (kPa)	σ_{v0} (kPa)	K_0 (-)
clay_1	3000	0.49	20	0	0	-
clay_2	6000	0.49	20	0	0	-
clay_3	12000	0.49	20	0	0	-
clay_4	30000	0.49	20	0	0	-
clay_5	6000	0.49	20	10	0	-
clay_6	6000	0.49	20	20	0	-
clay_7	6000	0.49	10	0	0	-
clay_8	6000	0.49	20	0	50	1.0
clay_9	6000	0.49	20	0	50	0.4
clay_10	6000	0.49	20	0	50	2.5

Table 4.3 Definition of runs for cone penetration in clay.

Load-displacement curves and cone factors

The load-displacement curves computed for runs clay_1 to clay_4, in which the stiffness of the clay is varied, are presented in figure 4.11.

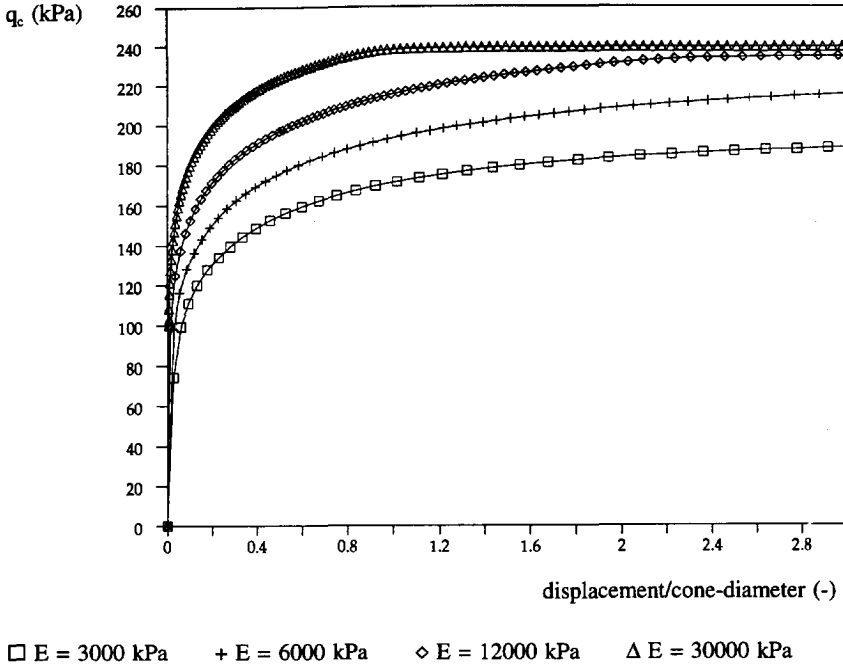


Figure 4.11 Load-displacement curves for cone penetration in clay (influence of stiffness).

Depending on the stiffness of the clay, after a material displacement of about 1D or 2D, a steady state is reached with respect to the cone resistance. In contrast with a small-strain analysis, the steady state cone resistance increases with enlarged stiffness. Cone factors are calculated ranging from 9.5 ($G/c_u = 50$) to 12.0 ($G/c_u = 500$). Introducing these values for G/c_u into the stiffness dependent part of eqn. (4.6), the second term, a difference is calculated equal to $(\ln 500 - \ln 50) = 2.3$. This is well in agreement with the numerical result of 2.5, i.e. $12.0 - 9.5$.

The cone resistance also increases with growing interface friction. The results of runs clay_2, clay_5 and clay_6 indicate that the cone factor increases from 10.9 (for $a/c_u = 0$) to 12.2 ($a/c_u = 0.5$) and to 12.9 ($a/c_u = 1.0$). The initial state of stress plays a minor role. Cone factors are calculated equal to 10.8 ($K_0 = 1.0$), 10.2 ($K_0 = 0.4$) and 11.2 ($K_0 = 2.5$).

Figure 4.12 presents the relation between the cone factor and the rigidity index (G/c_u) as derived by both the theoretical models (see figure 4.10) and the Eulerian large-strain finite element model. The full bold line corresponds to a smooth cone, whereas the shaded area can be reproduced by introducing interface friction between cone and soil.

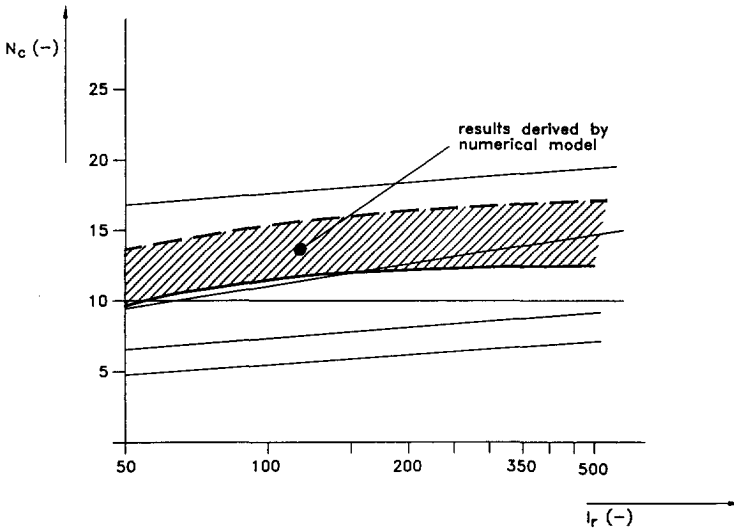


Figure 4.12 Relation between cone factor and rigidity index.

Analogous to the other models, the Eulerian finite element model too is not capable of calculating cone factors greater than, say, 16; at least for fully undrained conditions. To study the effect of (partial) drainage, we can change the behaviour from undrained to drained, while maintaining the same shear strength at a certain isotropic stress level, by the following theoretical relation:

$$c_u = c_d \cos \phi_d + \frac{\sigma_{v0} + \sigma_{h0}}{2} \sin \phi_d \quad (4.8)$$

If we assume $c_u = 20$ kPa, $c_d = 2$ kPa and $\sigma_{v0} = \sigma_{h0} = 50$ kPa, then ϕ_d can be calculated to be 21.3° . For this drained run, the material model is changed from Tresca to Mohr-Coulomb (parameters: c_d and ϕ_d), whereas all other quantities are chosen in agreement with run clay_8. The drained run yields a significant increase of the cone resistance as a cone factor is calculated equal to 33.3, while the undrained counterpart gives 10.8. Therefore, a number of experimental values greater than 20 might be caused by (partial) drained behaviour. However, final conclusions with respect to this subject can only be derived by more extensive research. For instance, the question has to be answered whether it is allowed to model drained behaviour of clay or silt by the Mohr-Coulomb criterion.

Displacements, stresses and strains

In this paragraph the results of run clay_2 ($G/c_u = 100$) are worked out in more detail. The incremental horizontal and vertical displacements during steady state penetration are visualized in figure 4.13a and 4.13b respectively. Horizontal deformations are limited to a small zone just around the tip of the cone, up to a maximum distance of about one cone diameter. Since a Eulerean approach is followed, the vertical displacement increments are given with respect to a certain prescribed value at the bottom of the mesh. To get the incremental displacements with respect to a vertical incremental displacement of the cone itself, the value at the lower boundary has to be subtracted. The combination of figure 4.13a and figure 4.13b yields a 2D velocity field, which can be compared to, for instance, flow-lines according to a simple pile or a simple cone model (figure 2.3).

Figures 4.13c and 4.13d show the plastic zone and isolines for the equivalent plastic strain (see eqn. (3.64)) at a total vertical displacement of 6 mm (i.e. 0.16 D) and 527 mm (14.6 D) respectively. In a first stage plasticity occurs at the sharp tip of the cone. The zone grows from the tip upward towards the shoulder of the cone. At enlarged deformation, due to the Eulerean approach, the plastified region moves upward along the shaft of the cone. In a narrow zone along the tip of the cone the shear strains become extremely large, about 125 %, during steady state penetration. The shape of the contour lines and the extend of the plastic region are in good agreement to those presented by Acar and Tumay (1986). They report maximum values between 50 and 100 %, calculated by a simple pile model.

Contour lines for the radial and vertical stresses are presented in figure 4.14 at a total displacement of 6 mm and 527 mm. It is remarkable that during the first stage of penetration some reduction of horizontal stress appears both at the shaft of the cone

and underneath the tip. At larger displacements due to lateral compression of the soil coming from below the tip of the cone tensile stresses disappear. It can be clearly seen that soil coming from below the tip of the cone is radially compressed when arriving along the shaft of the cone. The calculated radial stress around the shaft at steady state penetration, being about 100-120 kPa, is well in agreement with the stress derived by the cylindrical cavity expansion theory. According to this theory a radial stress is calculated equal to 112 kPa. On the other hand, the mean isotropic stress around the tip of the cone (about 160 kPa) is in good agreement to the stress calculated by spherical cavity expansion theory, i.e. 150 kPa.

4.3.3 Conclusions

Based on the results of the Eulerian finite element model the following conclusions can be drawn with respect to cone penetration in purely cohesive soils:

- for a fully smooth cone the cone factors derived by the model are well in agreement with those following from a simple pile approach.
- the cone resistance measured by a rough cone is about 1.3 times the resistance measured by a smooth cone.
- during steady state penetration plasticity occurs in a region up to about one cone-diameter D underneath the tip of the cone and about $2.5D$ around the shaft; the maximum shear strain is equal to 125 %.
- the radial stress around the shaft is well in agreement with the stress calculated by the cylindrical cavity expansion theory; the mean isotropic stress around the tip agrees to the stress obtained by the spherical cavity expansion theory.

In this paragraph the purely cohesive Tresca model is used to model the undrained behaviour of clay. The undrained shear strength according to this model is a good measure for the strength of the material and thus for the cone resistance. However, if one is interested in the development of pore pressures around a penetrating cone, the use of a more sophisticated constitutive model is recommended, for example a model based on critical state soil mechanics.

4.4 Penetration in sand

4.4.1 Introduction

The simplest formula used in engineering practice for the interpretation of cone penetration test data in drained, frictional material relates the cone resistance to the total overburden pressure. This equation originates from the bearing capacity theory (see paragraph 2.2.1):

$$q_c = N_q \sigma_{v0} \quad (4.9)$$

where:

- q_c cone resistance
- N_q bearing capacity factor
- σ_{v0} total overburden pressure

According to test results measured in large calibration chambers and collected by Robertson and Campanella (1986), N_q varies between 20 and 400 (see figure 4.15). In the literature behind these data it is found that the bearing capacity factor is at least a function of the stiffness of the soil E , the lateral pressure ratio K_0 , the angle of internal friction and the amount of dilatancy (ϕ_{peak} and ϕ'_{cv}), the density of the sand and the interface friction between cone and soil.

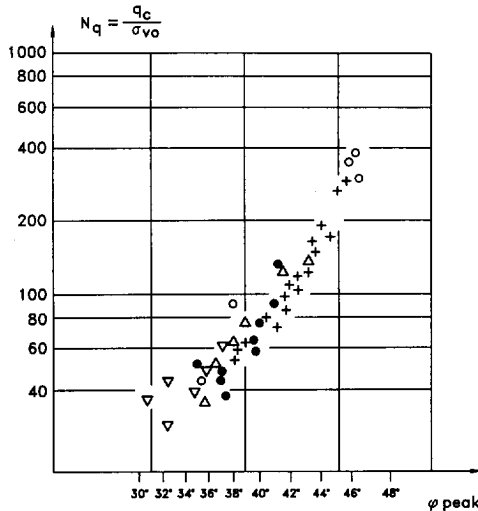


Figure 4.15 Relation between N_q and ϕ_{peak} following from calibration chamber tests (Robertson and Campanella, 1986).

Of course, density and friction angle are closely related. Once the relative density is known, it is possible to estimate the peak friction angle using, for instance, Bolton's empirical correlation (Bolton, 1986). For an overview and the most recent results of calibration chamber tests, the reader is referred to Schnaid and Houlsby (1992), who carried out a test programme to investigate the influence of relative density, stress level and stress ratio on cone pressuremeter test data.

The relation between N_q and the peak friction angle according to a large number of models based on the bearing capacity theory is shown in figure 4.16 (Vesic, 1967). From this figure it is clear that the predicted values for N_q differ substantially, depending on the specific model, i.e. the assumed shape and location of the failure plane.

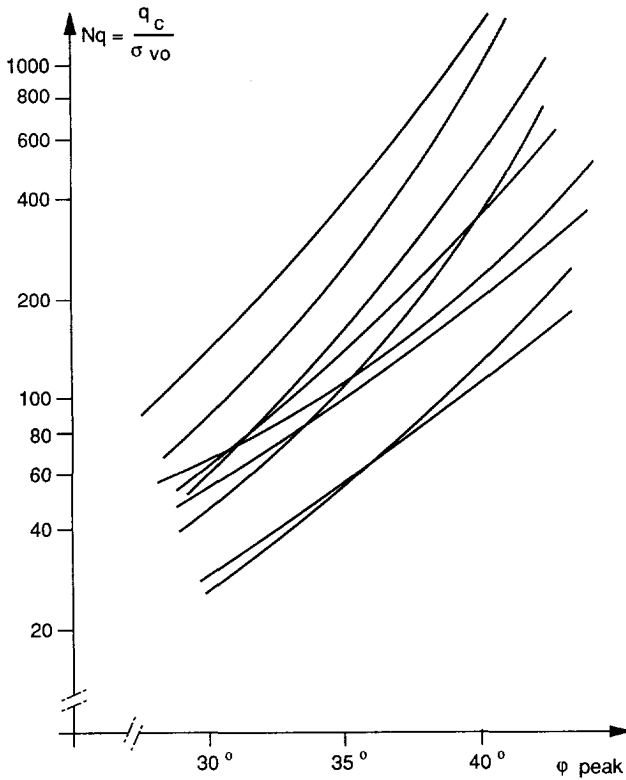


Figure 4.16 Relation between N_q and ϕ_{peak} following from models based on bearing capacity theory (Vesic, 1967).

The well-known correlation proposed by Robertson and Campanella (1986) is a combination of two bearing capacity solutions: the theoretical relationship proposed by Janbu and Senneset (1974) and the one given by Durgunoglu and Mitchell (1975).

Bearing capacity theory cannot take account of soil compressibility. A method in which this aspect can be introduced is the cavity expansion theory (see paragraph 2.2.2). In this kind of models use is commonly made of the rigidity index, I_r , and the reduced rigidity index, I_{rr} . These indices are defined as follows:

$$I_{rr} = \frac{I_r}{(1 + I_r \Delta)} \tag{4.10}$$

with:

$$I_r = \frac{E}{2(1 + \nu)(c + \gamma z \tan \phi)} \tag{4.11}$$

where E , ν , c and ϕ are Youngs' modulus, Poissons' ratio, cohesion and friction angle respectively, γz is the total overburden pressure prior to cavity expansion and Δ is the average volume change in the plastic zone as a percentage of the initial volume. Under undrained conditions I_r is identical to G/c_u . Bearing capacity factors for different values of I_{rr} , calculated by Vesic (1975), are shown in figure 4.17.

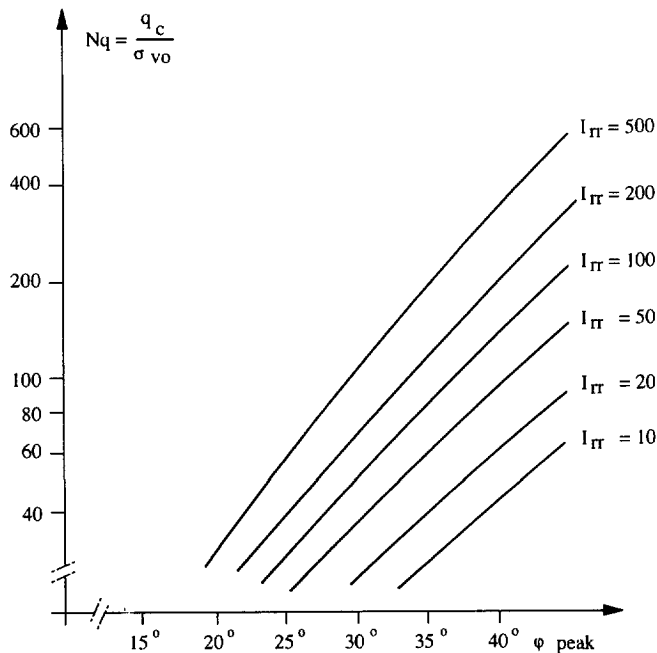


Figure 4.17 Relation between N_q and ϕ_{peak} following from models based on cavity expansion theory (Vesic, 1975).

At present publications have started to emerge in which the penetration problem is simulated by Updated Lagrangean finite element models. Cividini and Gioda (1988) present some results of penetration into a Drucker-Prager material. They use zero-thickness interface elements to model the frictional behaviour between cone and soil and they vary the smoothness of the cone-soil interface. Also Kioussis, Voyiadjis and Tumay (1988) present a model and some results of penetration of a smooth cone in sandy soil using a Di-Maggio and Sandler cap-model. In addition, results are given by Willson (1985). All of them have in common, that a model is presented and/or a few results are shown. It is very difficult to get a clear insight into the performance of the models. Schnaid and Houlsby (1992) come to the conclusion that analytical and numerical methods for the interpretation of cone pressuremeter tests in sand are currently being developed, but their suitability for the derivation of reliable friction and dilatancy angles requires further investigation.

Experimental data and bearing capacity as well as cavity expansion results are summarized in figure 4.18. In the next section the Eulerian finite element model is applied to investigate the influence of stiffness, strength, initial stress level and stress ratio as well as interface friction on the cone resistance.

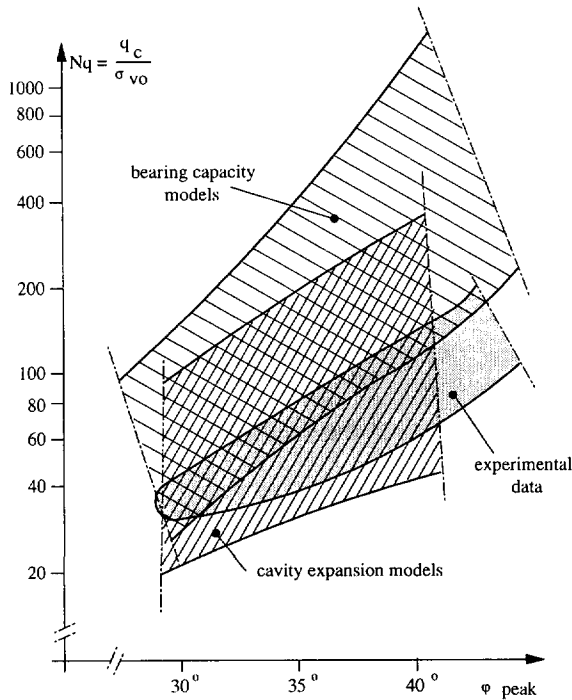


Figure 4.18 Relation between N_q and ϕ_{peak} following from experimental data, bearing capacity theory and cavity expansion models.

4.4.2 Numerical analysis

Introduction

The numerical analysis is subdivided into a preliminary analysis (see also: van den Berg et al., 1992a) and a more comprehensive sensitivity analysis. The aim of the preliminary analysis is to investigate the influence of the roughness of the cone (smooth or Coulomb friction) and the choice of the constitutive model (Drucker-Prager or Mohr-Coulomb). The finite element discretization used in the preliminary calculations is presented in figure 4.19. This mesh consists of 75 four-noded quadrilateral enhanced B-elements (Nagtegaal et al., 1974) to model the soil and 13 zero-thickness elements to model the interface between cone and soil. For the simulation of a smooth cone the boundary condition at the shoulder of the cone is taken according to model B (figure 4.7).

Preliminary calculations

In order to investigate the influence of the roughness of the interface and the material model four runs have been carried out, characterized in table 4.4. In this table "D-P" refers to the Drucker-Prager constitutive model, whereas "M-C" stands for Mohr-Coulomb behaviour. Prior to penetration the material is in a state of critical density, i.e. no volumetric effects take place during penetration.

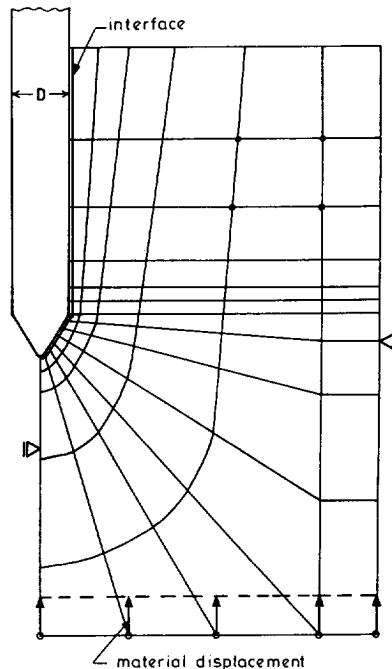


Figure 4.19 Finite element mesh for preliminary analysis.

run	E (kPa)	ν (-)	c (kPa)	ϕ_{cv} ($^{\circ}$)	ψ_0 ($^{\circ}$)	ξ (-)	σ_{v0} (kPa)	K_0 (-)	δ ($^{\circ}$)	a (kPa)	mat.
sand_1	1000	0.2	5	30	-	-	35	1.0	-	-	D-P
sand_2	1000	0.2	5	30	-	-	35	1.0	20	3.3	D-P
sand_3	1000	0.2	5	30	-	-	35	1.0	-	-	M-C
sand_4	1000	0.2	5	30	-	-	35	1.0	20	3.3	M-C

Table 4.4 Material data adopted in preliminary calculations.

Vertical material displacement increments are introduced at the bottom of the mesh. The calculation is stopped at the moment a steady state situation is reached with respect to cone resistance and skin friction. Load-displacement curves for run sand_4 (Mohr-Coulomb, frictional) are shown in figure 4.20. Two lines can be distinguished: the relation between displacement and (a) total vertical reaction force at the tip of the cone and (b) total frictional force at the shaft of the cone. To derive the cone resistance the tip reaction force has to be divided by the projected area of the cone, i.e. 10 cm^2 . The skin friction can be calculated by dividing the total frictional force by the outer surface of the friction sleeve, i.e. 150 cm^2 .

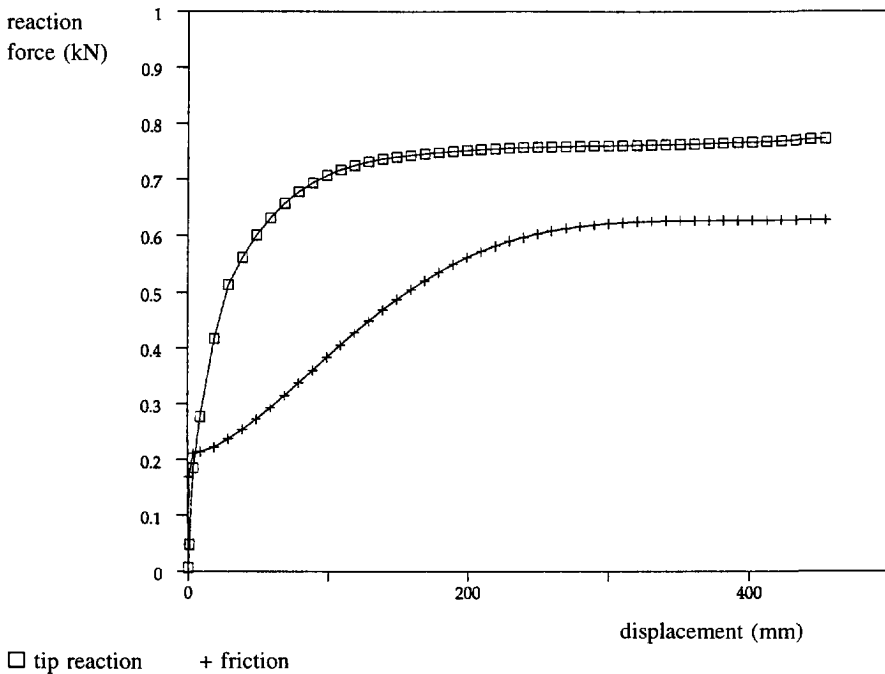


Figure 4.20 Load-displacement curves computed for run sand_4 (Mohr-Coulomb, frictional).

The line representing the frictional force shows two different stages. First, at a very small displacement level (a few millimeters), the initial frictional force is mobilized being equal to the product of the initial horizontal stress and the interface friction coefficient (Coulomb friction). After that, the total frictional force steadily increases until a second constant level is reached. This second rise is caused by the fact that at enlarged penetrating distance, "expanded" soil coming from below the tip of the cone, i.e. soil with a larger horizontal stress, passes the friction sleeve.

The calculated values for the cone resistance, the skin friction, the bearing capacity factor and the friction ratio for runs sand_1 to sand_4 are summarized in table 4.5. The friction ratio is defined as the skin friction divided by the cone resistance.

run	characteristics	q_c (MPa)	f_s (MPa)	N_q (-)	f_r (%)
sand_1	Drucker-Prager, smooth	0.29	0	9.7	-
sand_2	Drucker-Prager, frictional	0.63	0.050	21.0	7.9
sand_3	Mohr-Coulomb, smooth	0.28	0	9.3	-
sand_4	Mohr-Coulomb, frictional	0.76	0.041	25.3	5.4

Table 4.5 Cone resistance, skin friction, bearing capacity factor and friction ratio for preliminary calculations.

Roughness of the cone

From the results of table 4.5 it is clear that, when considering friction between cone and soil, the cone resistance is doubled or tripled. Stress distributions around a smooth and a frictional cone also differ considerably. This is shown in figures 4.21 and 4.22, in which horizontal and vertical stresses around the cone at steady state penetration are given.

Results for run sand_1 (Drucker-Prager, smooth) are shown in the left hand figures, while the right hand figures contain the results corresponding to run sand_2 (Drucker-Prager, frictional). The contents of those figures lead to the following conclusions:

- The horizontal stress build-up along the shaft of the cone can be clearly recognized. This effect, caused by the fact that soil coming from below the tip of the cone has to be pushed aside to make room for the cone, cannot be simulated in a conventional Lagrangean small-strain analysis.
- For a smooth cone and a relatively small value of the friction angle ($\phi=30^\circ$), the horizontal stresses and even the isotropic stresses underneath the tip of the cone decrease. A kind of "splitting" failure mechanism occurs.

- The horizontal stress level around the tip of the cone is larger than the vertical stress level (smooth cone) or within the same order of magnitude (frictional cone).

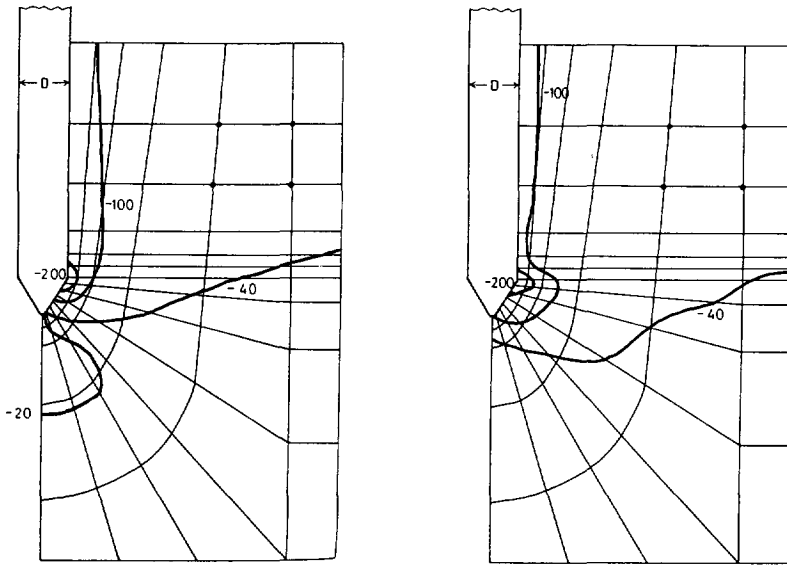


Figure 4.21 Horizontal stress at steady state penetration (left-hand side: smooth cone and right-hand side: frictional cone).

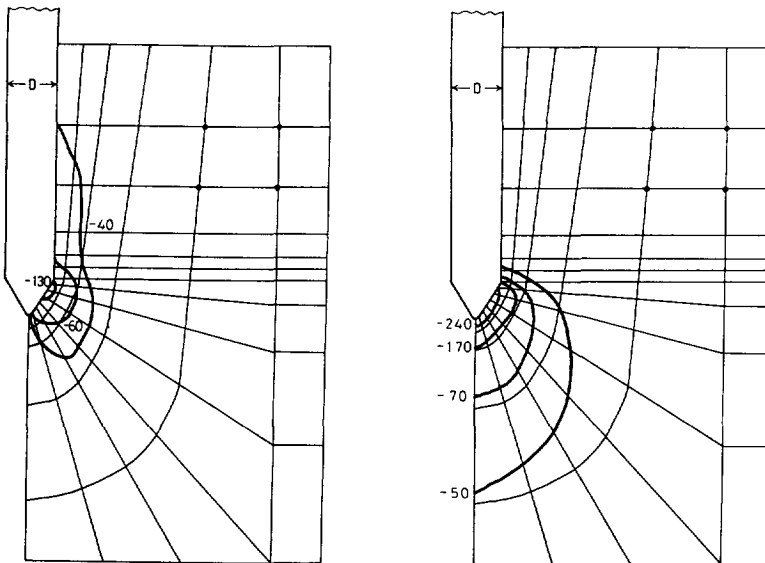


Figure 4.22 Vertical stress at steady state penetration (left-hand side: smooth cone and right-hand side: frictional cone).

Concluding it can be remarked that it is necessary to include interface friction into the model in order to get reliable results. This is confirmed by the fact that bearing capacity factors calculated for smooth cones ($N_q \approx 10$) fall outside the shaded regions given in figure 4.18. The calculated results for frictional cones ($N_q = 20 - 30$) are in better agreement to measured data.

The friction ratios calculated are too large when compared to data measured in practice. Friction ratios for sand are normally found between, say, 0.5 and 2 %. The calculated value for Mohr-Coulomb behaviour is about 5 %. This implies that the ratio between the strength of the interface and the strength of the continuum, assumed in the analysis, i.e. 0.667, is too large.

Constitutive models

The results for Drucker-Prager behaviour can be compared to those for Mohr-Coulomb behaviour (see table 4.5). It is found that:

- For a smooth cone, the difference between both constitutive models is negligible. A Drucker-Prager model gives a slightly higher cone resistance.
- For a frictional cone, however, there is a significant difference between both models. A Mohr-Coulomb model gives a higher cone resistance and a lower skin friction when compared to a Drucker-Prager model.

The reason for these phenomena has to do with the fact that around a penetrating cone two regions can be distinguished, visualized in figure 4.23. The stress state in region "A" is a state of triaxial compression" (the maximum stress is the vertical stress component), whereas in region "B" a state of triaxial extension prevails (maximum stress is the horizontal stress component).

The parameter values for the constitutive behaviour are chosen in such a way that for triaxial compression the Drucker-Prager and Mohr-Coulomb models coincide (see figure 4.23). This particular choice implies that for a smooth cone the difference is negligible, since for a smooth cone only the region in front of the cone tip plays a role. For a frictional cone, the horizontal stress build-up around the shaft defines the generated skin friction. These horizontal build-up stresses are lower than for a Mohr-Coulomb model than for a Drucker-Prager model (see figure 4.23). Consequently, the skin friction will be lower as well.

Stress paths for a number of nodal points are presented in figure 4.24 (Drucker-Prager) and in figure 4.25 (Mohr-Coulomb). For Drucker-Prager behaviour the failure line for triaxial compression is identical to the one for triaxial extension. For Mohr-Coulomb behaviour, however, a nodal point on the shaft (triaxial extension) follows another stress path than a point at the cone tip (triaxial compression).

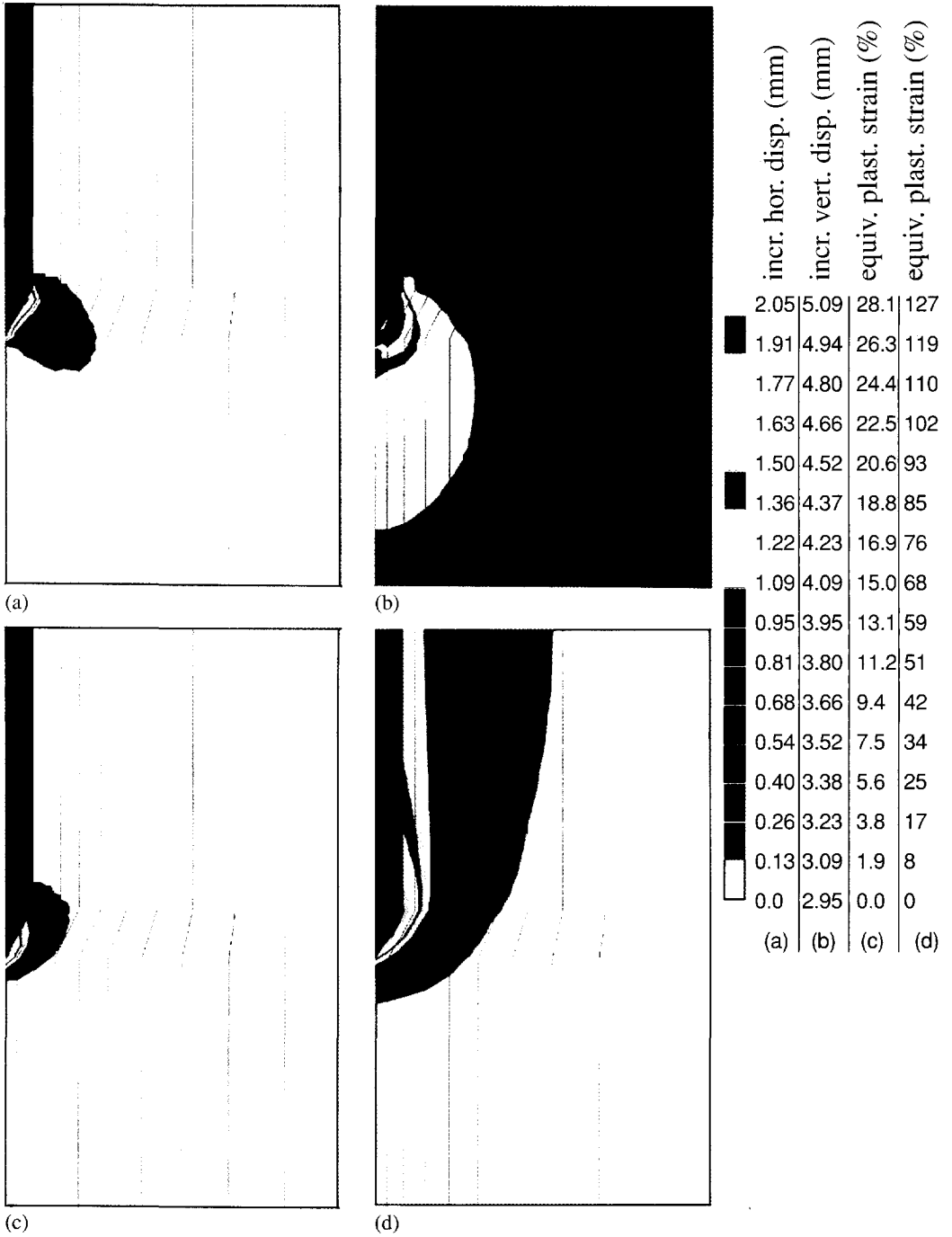


Figure 4.13

Incremental horizontal (a) and vertical (b) displacements at steady state penetration and equivalent plastic strain at a displacement of 6 mm (c) and 527 mm (d); $G/c_0 = 100$.

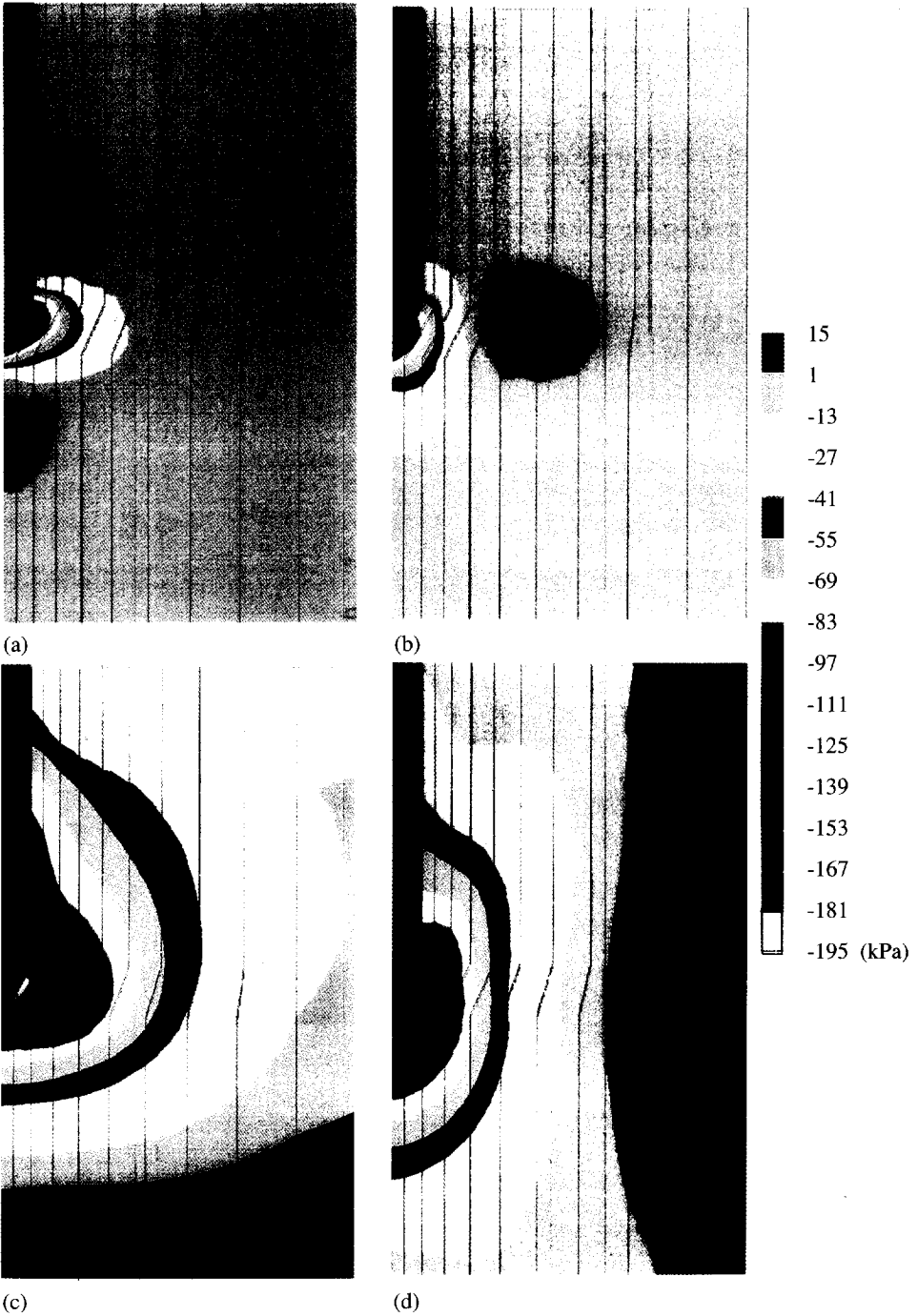


Figure 4.14

Horizontal (a,c) and vertical stresses (b,d). Both figures at the top at a displacement of 6 mm and those at the bottom at a displacement of 527 mm; $G/c_u = 100$.

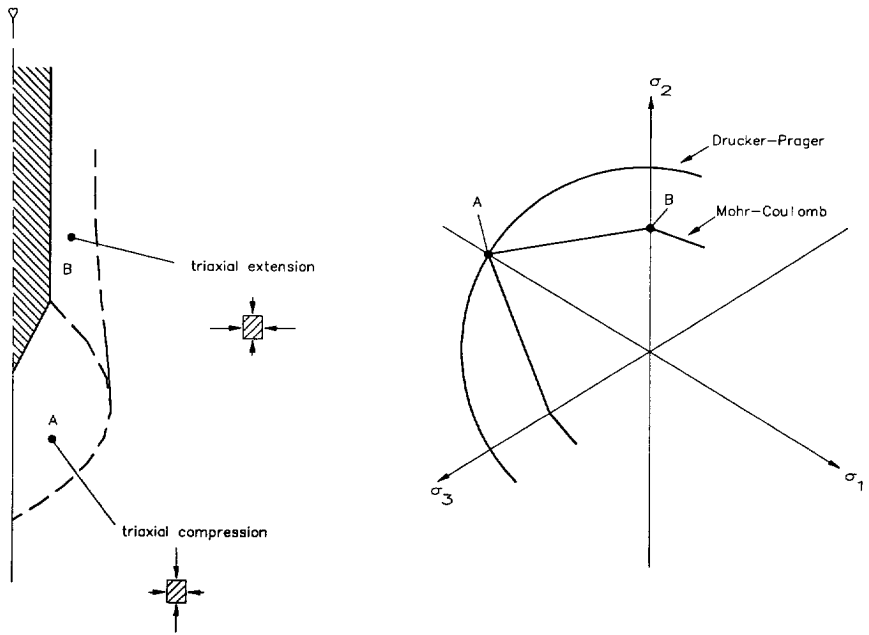


Figure 4.23 Triaxial compression (A) and triaxial extension (B) region around penetrating cone.

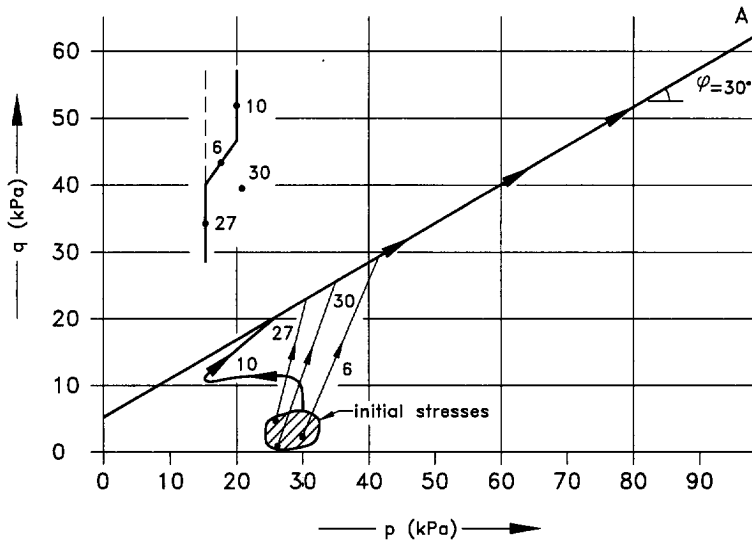


Figure 4.24 Stress paths in p-q diagram for run sand_2 (Drucker-Prager).

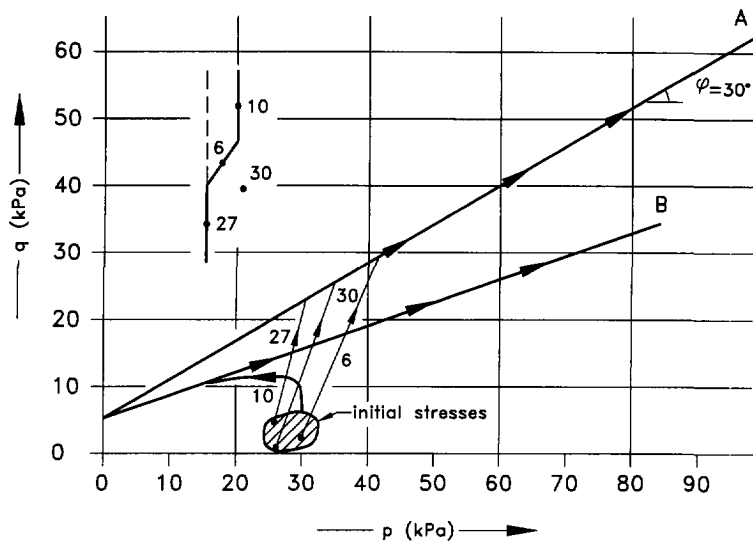


Figure 4.25 Stress paths in p-q diagram for run sand_4 (Mohr-Coulomb).

Concluding, it can be remarked from the preliminary analysis that it is necessary (a) to introduce interface friction between cone and soil and (b) to use a Mohr-Coulomb model, especially in order to get more realistic values for the friction ratio.

Definition of runs for sensitivity analysis

In order to quantify the influence of the stiffness of the sand, the friction angle at constant volume deformation, the amount of dilatancy, the roughness of the cone and the initial state of stress, a sensitivity analysis has been carried out. The finite element mesh used is presented in figure 4.4. The constitutive behaviour of the sand is modelled by the hardening/softening Mohr-Coulomb model (paragraph 3.4.3). In this model the dilatancy angle reduces from an initial value to zero and the friction angle decreases from a peak value to the friction angle for constant volume deformation. Characteristic input data is given in table 4.6.

Load-displacement curves and bearing capacity factors

Calculated load-displacement curves are presented in figures 4.26 to 4.30. In these figures the relation is shown between the cone resistance and respectively: the stiffness of the sand (figure 4.26), the friction angle (figure 4.27), the interface friction (figure 4.28), the lateral pressure ratio (figure 4.29) and the initial vertical stress level prior to penetration (figure 4.30). The influence of the amount of dilatancy can be found by comparing the results of runs sand_5 and sand_8. The curves show some minor numerical instabilities, caused by the interface elements. However, for all

cases reasonable steady state limit loads with respect to the cone resistance could be found.

run	E (kPa)	ν (-)	c (kPa)	ϕ_{cv} ($^\circ$)	ψ_0 ($^\circ$)	ξ (-)	σ_{v0} (kPa)	K_0 (-)	δ ($^\circ$)	a (kPa)	mat.
sand_5	5000	0.3	2	30	10	0.072	35	1.0	10	0.67	M-C
sand_6	10000	0.3	2	30	10	0.072	35	1.0	10	0.67	M-C
sand_7	20000	0.3	2	30	10	0.072	35	1.0	10	0.67	M-C
sand_8	5000	0.3	2	30	0	-	35	1.0	10	0.67	M-C
sand_9	5000	0.3	2	25	0	-	35	1.0	10	0.67	M-C
sand_10	5000	0.3	2	35	0	-	35	1.0	10	0.67	M-C
sand_11	5000	0.3	2	30	10	0.072	35	0.67	10	0.67	M-C
sand_12	5000	0.3	2	30	10	0.072	350	1.0	10	0.67	M-C
sand_13	5000	0.3	2	30	10	0.072	35	1.0	20	1.33	M-C
sand_14	5000	0.3	2	30	10	0.072	35	1.0	5	0.33	M-C

Table 4.6 Material data adopted in sensitivity analysis.

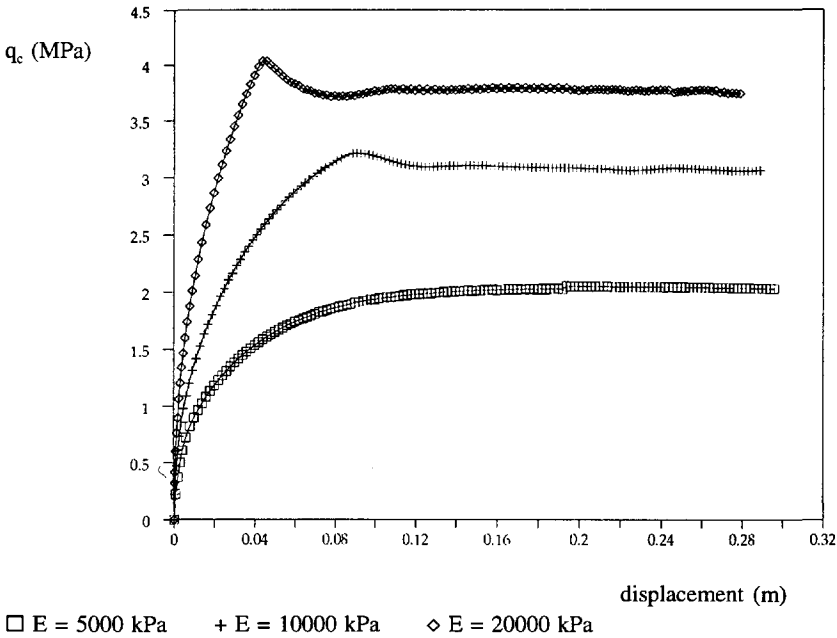


Figure 4.26 Influence of stiffness on cone resistance (runs sand_5, sand_6 and sand_7, see table 4.6).

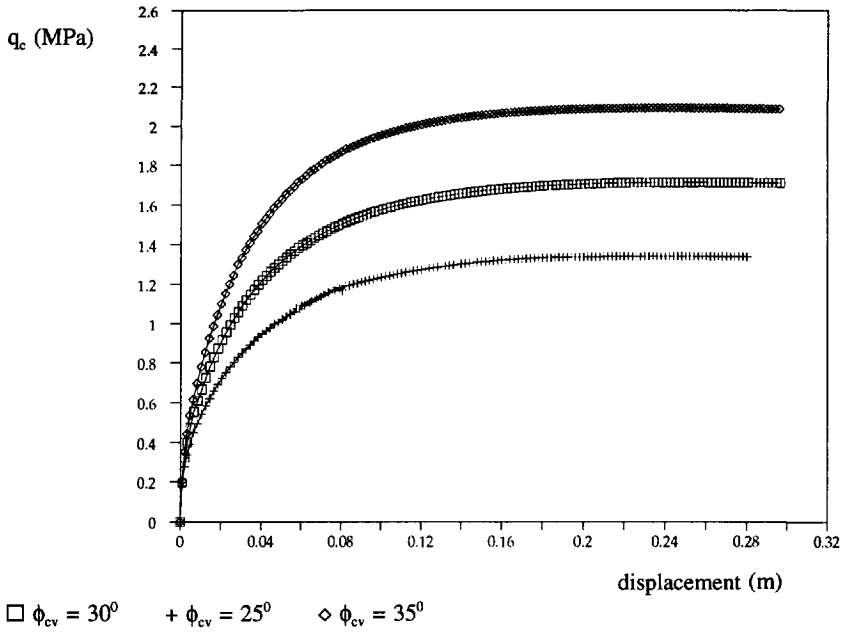


Figure 4.27 Influence of friction angle on cone resistance (runs sand_8, sand_9 and sand_10, see table 4.6).

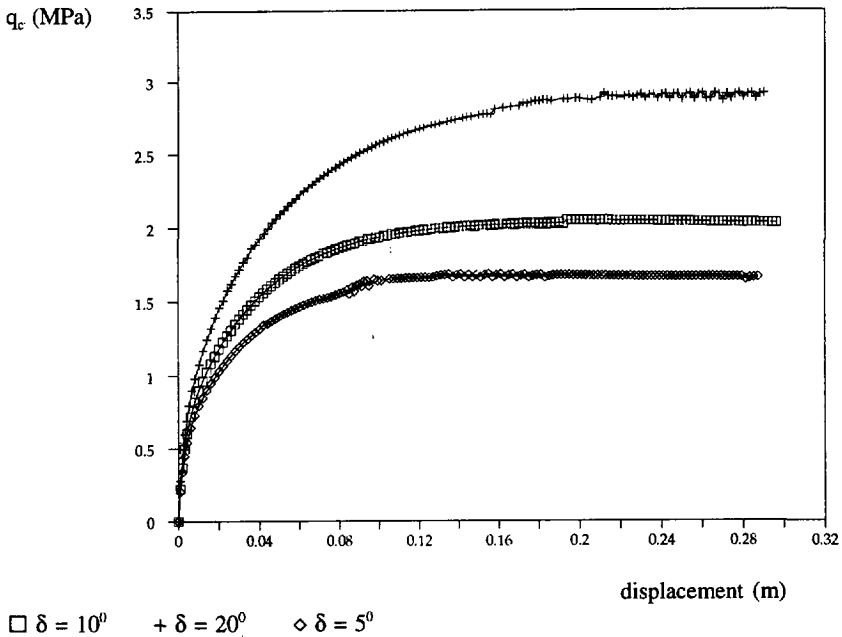


Figure 4.28 Influence of interface friction on cone resistance (runs sand_5, sand_13 and sand_14, see table 4.6).

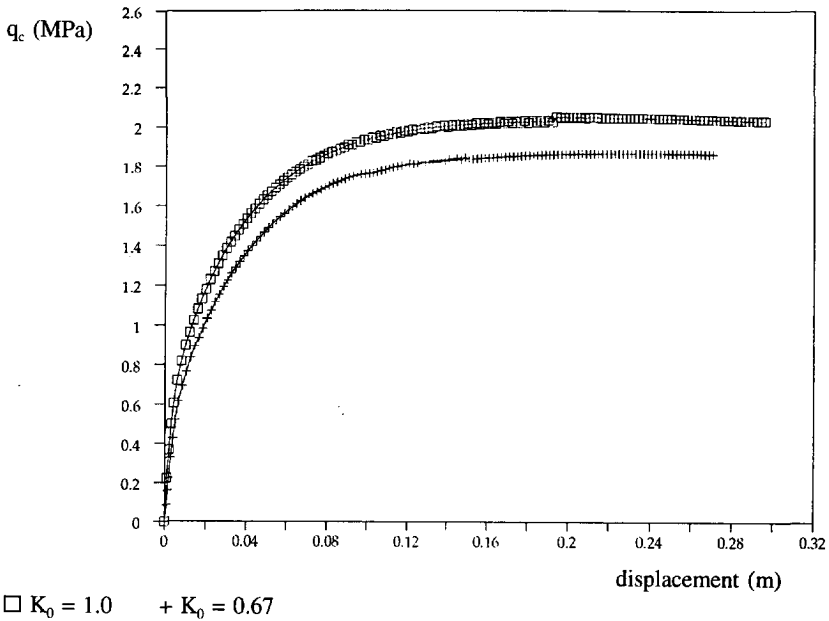


Figure 4.29 Influence of lateral pressure ratio on cone resistance (runs sand_5 and sand_11, see table 4.6).

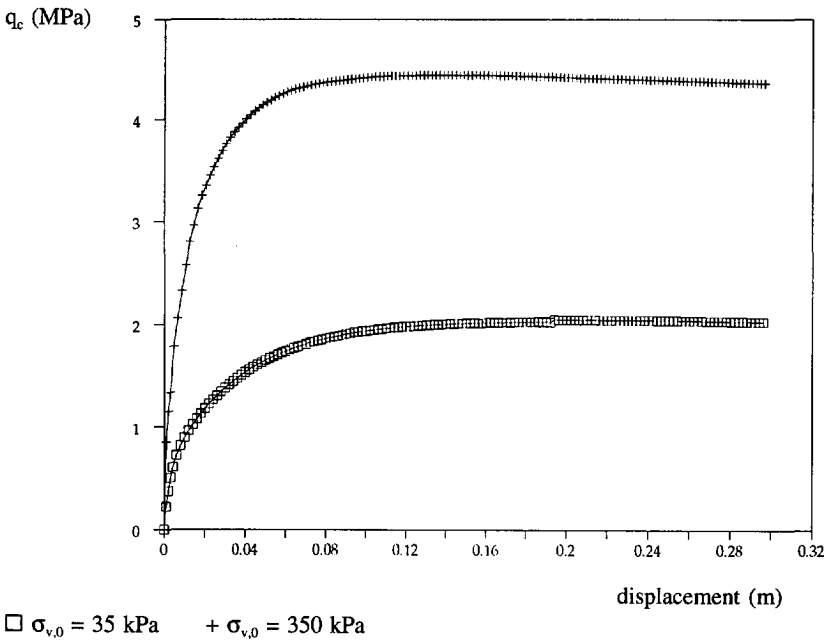


Figure 4.30 Influence of initial vertical stress on cone resistance (runs sand_5 and sand_12, see table 4.6).

The steady state values are summarized in table 4.7 and in figure 4.31. The results indicate that the cone resistance depends on all of the parameters: stiffness, friction and dilatancy, interface friction, initial vertical stress and, to a smaller extent, the lateral pressure ratio prior to penetration.

run	q_c (kPa)	N_q (-)	f_s (kPa)	f_r (%)
sand_5	2035	58.1	51	2.5
sand_6	3070	87.7	49	1.6
sand_7	3760	107.4	17	0.5
sand_8	1710	48.9	39	2.3
sand_9	1340	38.3	31	2.3
sand_10	2080	59.4	44	2.1
sand_11	1860	53.1	46	2.4
sand_12	4380	12.5	139	3.2
sand_13	2900	82.6	61	2.1
sand_14	1660	47.4	33	2.0

Table 4.7 Results of sensitivity analysis cone penetration in sand.

The results derived by the numerical model can be compared to experimental data and data calculated by other models. For example, the peak friction angle adopted in the runs sand_5, sand_6, sand_7, sand_11, sand_13 and sand_14 is equal to 38.3° . The bearing capacity factors calculated range from about 45 to 110. The experimental data are in the same order of magnitude (see figure 4.18). It is noted that the combination of parameters for run sand_12 is not very realistic, especially the stiffness in relation to the initial vertical stress.

The friction ratio is strongly influenced by the stiffness of the sand in the sense that the larger the stiffness the lower the friction ratio. The other parameters hardly affect the friction ratio. The friction ratio for all cases with $E = 5000$ kPa (except sand_12) is between 2.0 % and 2.5 %. For $E = 10000$ kPa the friction ratio is about 1.5 % and for $E = 20000$ kPa about 0.5%.

Displacements, stresses and strains

The shape of the load-displacement curve depends on the stiffness of the material (see figure 4.26). The results indicate that for $E = 5000$ kPa the slope of the curve smoothly goes to a steady state limit value. With increasing stiffness, however,

another mechanism arises. At a certain load level localization of deformation suddenly occurs and the direction of the curve slope changes. Therefore, in the discussion about the deformation mechanisms associated to cone penetration in sand we will concentrate on the results corresponding to run sand_5 ($E = 5000$ kPa) and run sand_7 ($E = 20000$ kPa).

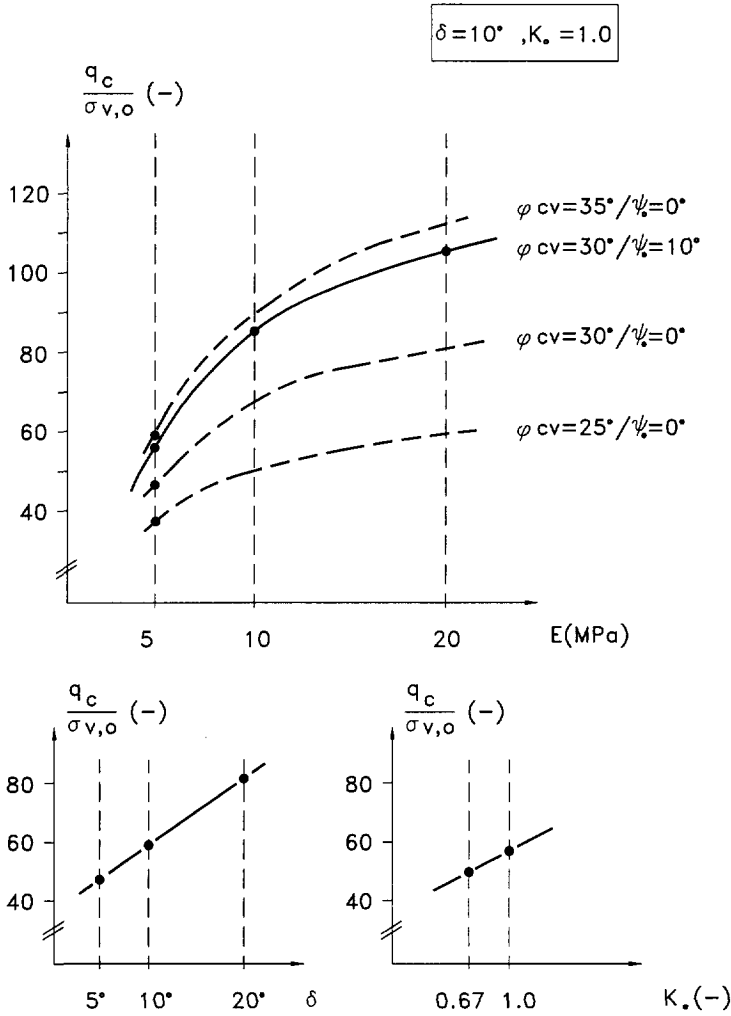


Figure 4.31 Results of sensitivity analysis cone penetration in sand ($\sigma_{v,0} = 35$ kPa).

Incremental displacements are shown in figure 4.32 ($E = 5000$ kPa) and figure 4.33 ($E = 20000$ kPa). In order to clarify the deformation mechanisms the incremental displacement vectors are plotted with respect to a unit vertical cone displacement (i.e.

the calculated incremental displacements diminished by the prescribed vertical material displacement at the bottom of the mesh).

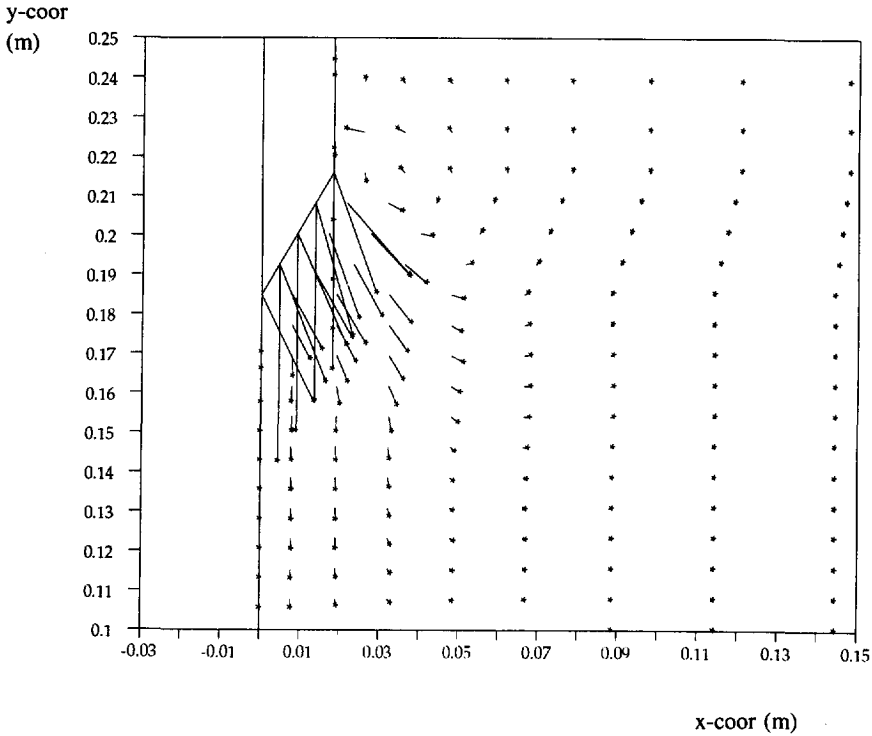


Figure 4.32 Incremental displacements around cone at steady state penetration ($E = 5000$ kPa).

For $E = 5000$ kPa (run sand_5) the distribution of the deformation around the cone is very much the same throughout the complete calculation. Deformation can be observed up to a distance of 2 or 3 diameters in front of the cone. Radial movements can only be recognized in a zone up to 1 or 2 diameters outside the cone axis. The deformation pattern around the shoulder of the cone, a vortex-shaped movement of the material, is very complicated. It is important to be aware of this fact, since at that point normally the pore pressure is measured.

Figure 4.33 ($E = 20000$ kPa, run sand_7) shows the deformation pattern before localization (figure 4.33a, displacement = 0.03 m) and after localization (figure 4.33b, displacement = 0.05 m). Initially, the deformation mechanism closely resembles the mechanism calculated for $E = 5000$ kPa (run sand_5): downward movement in front of the cone and no distinct failure planes. However, the mechanism suddenly changes: the deformation in front of the cone stops and the soil is pushed aside and

upward. The mechanism is quite similar to the well-known onion-shaped failure planes typical for bearing capacity theory (see figure 2.1). Since stiffness and deformation are closely related it naturally follows that in a loose sand deposit the deformation field will be smooth, whereas in dense sand distinct failure lines will occur. This is in agreement with observations during triaxial testing and plate load tests (Lorenz and Heinz, 1969).

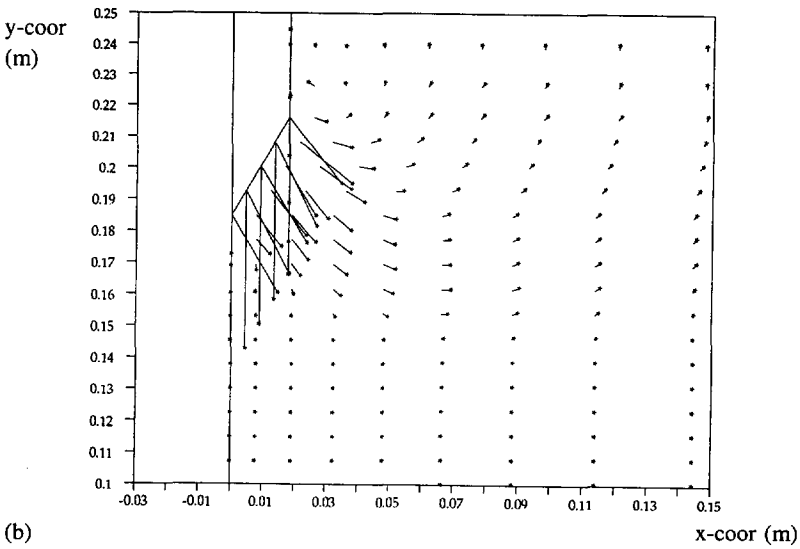
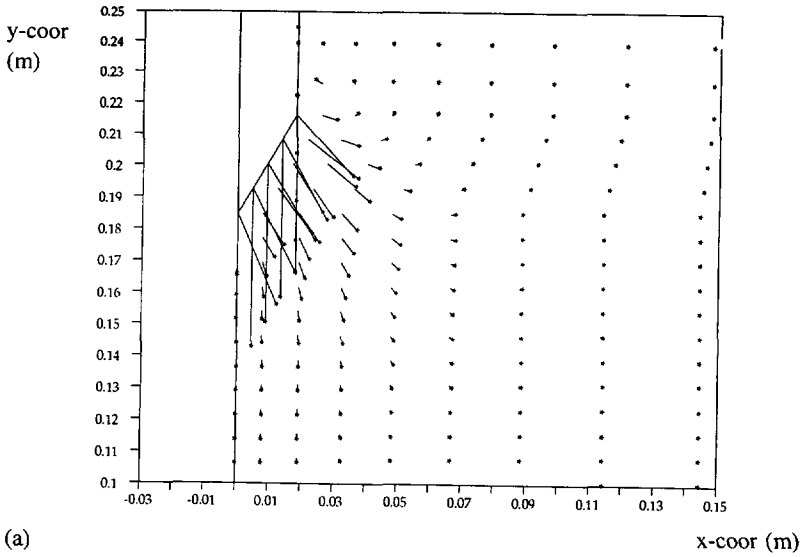


Figure 4.33 Incremental displacements around cone at a displacement of 0.03 m (a) and 0.05 m (b), $E = 20000$ kPa.

The stress distribution around the cone during steady state penetration in sand is shown in figure 4.34 (run sand_5, $E = 5000$ kPa): horizontal, vertical, tangential and invariant shear stresses respectively. From these pictures it can be concluded that:

- the maximum stresses can be found in a region just beneath the shoulder of the cone.
- the horizontal and vertical stresses are in the same order of magnitude.
- just above the shoulder of the cone a sharp reduction of stresses can be seen.
- the horizontal stress around the shaft of the cone due to the expansion of soil coming from below the tip of the cone is about 400 kPa.

Equivalent plastic shear strains at steady state penetration are visualized in figure 4.35 (run sand_5). It is noted that the plastified region is somewhat larger than the coloured zone in the figure, since the first contour-line represents the region inside which the plastic strain is larger than 10 %. Globally, the coloured area can be interpreted as the region in which the material is in a state of critical density as in the constitutive model the critical density is reached at a shear strain level of about 10-15 %. It can be seen that:

- the plastic region in front of the cone is limited: up to about one cone diameter downward.
- the maximum shear strain is about 150 %.
- the size of the plastic zone around the shaft is about 1.5 cone diameter.

Pore water pressure

Effective stress analyses for cone penetration start from the assumption that this process can be considered to be fully drained. For large values of the permeability of the sand this indeed seems to be reasonable. However, the question arises whether fine-grained or silty sands have to be interpreted as undrained material (clay) or as drained material (sand). In order to get a first approximation of the pore water pressures generated during penetration, the uncoupled approach theoretically worked out in paragraph 3.4.6 is followed.

First, the volumetric strain increments around the cone are derived by an effective stress analysis. The constitutive behaviour of the soil is modelled by the hardening-softening Mohr-Coulomb model (see paragraph 3.4.3). Table 4.8 shows characteristic data adopted in the calculations. The other quantities, which are not included in this table, are similar to those of run sand_5 (see table 4.6). Starting from an undisturbed initial state of stress ($\sigma_{v0} = 35$ kPa and $K_0 = 1.0$), at three displacement levels (2, 80 and 160 mm penetration) the pore water pressure distribution around the cone is determined in a separate (groundwater) flow analysis (see paragraph 3.4.6). The results for runs pore_1 and pore_3 are presented in figure 4.36.

run	ϕ_{cv}	ψ_0	ξ	density
pore_1	40° (ϕ)	10° (ψ)		very dense (no softening)
pore_2	30°	0°	0.072	critical density
pore_3	30°	10°	0.072	very dense
pore_4	30°	5°	0.072	medium dense
pore_5	30°	-5°	0.072	medium loose
pore_6	35°	10°	0.072	very dense

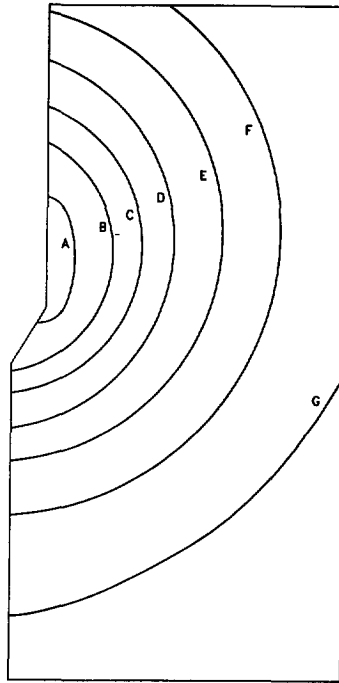
Table 4.8 Characteristic data for pore pressure analysis.

The distribution of excess pore water pressures around the cone is shown in the upper part of figure 4.36. The shape of the contour-lines can be considered to be typical, as all runs qualitatively yield the same results. The quantitative values, however, strongly depend on the permeability and the amount of generated volumetric strain, characterized by the initial dilatancy angle and the softening parameter. This is shown in the lower part of figure 4.36. At a displacement of 160 mm a steady state is reached, both at location A (the tip of the cone) and at location B (the position of the pore pressure transducer, see figure 4.1). For dense sand ($\psi_0 = 10^\circ$) and a permeability of 10^{-4} m/s negative pore water pressures are derived varying between 1 kPa and 6 kPa, depending on the amount of dilatancy softening. All results are linearly dependent on the permeability of the material.

Figure 4.37 shows the results calculated for different values of the initial dilatancy angle (which is a measure for the density prior to penetration) and the friction angle at constant volume deformation. The figure indicates that the excess pore water pressure is linearly dependent on the initial dilatancy angle and independent of the friction angle at constant volume. In order to derive an approximation of the excess pore water pressure during cone penetration the following procedure can be used in geotechnical engineering practice:

1. Determine the permeability k of the sand.
2. Determine the initial relative density prior to penetration, D_r , or the peak friction angle. Both quantities are related (Bolton, 1986). For Dutch sands, for instance, the following relation can be used (SCW, 1978):

$$\phi_{peak} = 28^\circ + 15^\circ * D_r \quad (4.12)$$



A: -0.93 kPa
 B: -0.82 kPa
 C: -0.74 kPa
 D: -0.61 kPa
 E: -0.50 kPa
 F: -0.39 kPa
 G: -0.28 kPa
 (pore-3)

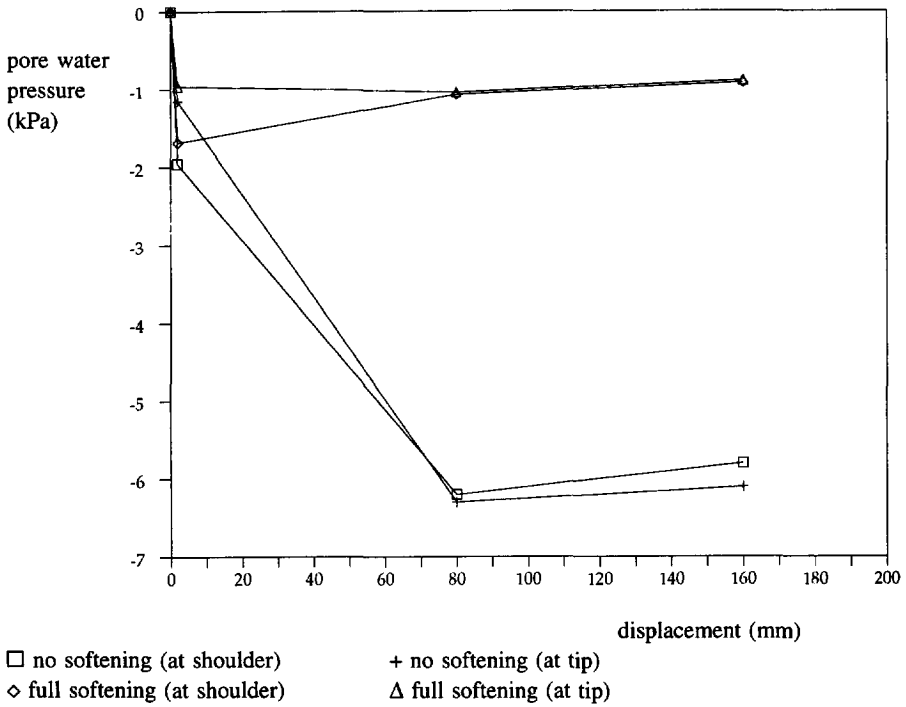


Figure 4.36 Pore water pressures around penetrating cone ($k = 10^{-4}$ m/s).

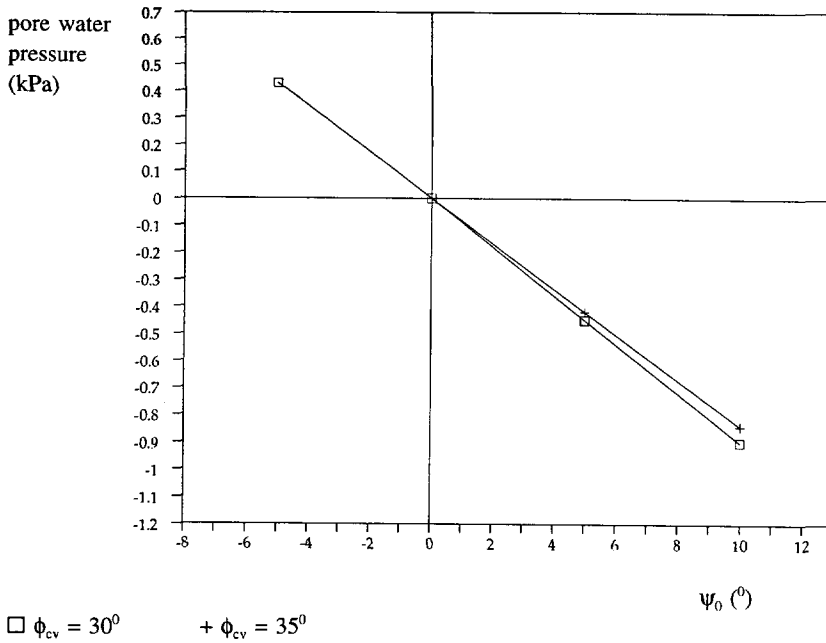


Figure 4.37 Relation between generated pore pressure around penetrating cone and density (full softening, $k = 10^{-4}$ m/s).

3. The initial dilatancy angle, ψ_0 , can be derived from ϕ_{peak} and ϕ_{cv} by using Rowe's stress dilatancy relation:

$$\sin \phi_{peak} = \frac{\sin \phi_{cv} + \sin \psi_0}{1 + \sin \psi_0 \sin \phi_{cv}} \quad (4.13)$$

where ϕ_{cv} can be assumed to be about 30° .

4. Calculate the generated pore water pressure, u , by the following relation:

$$|u| = 0.14 \text{ à } 0.84 \frac{v}{k} \gamma_w R \psi_0, \quad \psi_0 [rad] \quad (4.14)$$

where v is the penetration rate and R is the radius of the cone.

5. To get an answer to the question whether the measured values have to be interpreted like undrained or like drained material, the excess pore water

pressure has to be compared to the effective (isotropic) stress level at a certain depth. If the absolute value of u is larger than, say, 10% of the effective stress, then the penetration process cannot be interpreted straightforwardly as a drained process.

Following this procedure, it can be concluded that cone penetration in sand with a permeability larger than about 10^{-5} [m/s] can be considered to be a drained process.

4.4.3 Conclusions

The results of the numerical analysis indicate that two regions can be distinguished around a penetrating cone. In front of the cone tip the material is in a state of triaxial compression, whereas around the shaft of the cone the stress state changes into triaxial extension. Consequently, the Mohr-Coulomb model is more convenient to analyse the penetration process than the Drucker-Prager one.

The following conclusions can be drawn with respect to penetration in sand:

- the cone resistance is not only influenced by the initial vertical stress and the peak friction angle, but also by the stiffness, the interface friction and, to a smaller extent, the lateral pressure ratio prior to penetration.
- in a loose sand deposit the deformation field around the cone is smooth, whereas in dense sand localization of deformation into distinct failure planes occurs.
- shear strains are calculated between 100 and 150 %, indicating the importance of the introduction of a critical state concept.
- penetration in sand with a permeability larger than about 10^{-5} m/s can be considered to be a drained process.

A more extensive comparison of the present results to those measured in large calibration chambers (Houlsby and Hitchman, 1988; Schnaid and Houlsby, 1992) is recommended.

Since it is found that the cone resistance is strongly influenced by the stiffness of the soil, independent information about the in-situ stiffness will increase the reliability of the estimated peak friction angle, or, in the context of this study, the initial density characterized by the initial dilatancy angle. A number of other ways are open to determine the in-situ stiffness of sand layers. For instance, penetration tests can be performed using cones with different shapes. The cone pressuremeter, too, is a powerful tool to get information about the stiffness. To analyse pressuremeter data the Eulerian finite element model of this study can be used adequately. Another way to derive an estimation of the soil stiffness will be presented in the next section. The gradient of the cone resistance per unit depth, measured when a cone passes through the boundary between two layers, includes information about the stiffness.

4.5 Penetration in layered soil

4.5.1 Introduction

The subsoil consists of layered deposits with different thicknesses and properties. During the interpretation of measured data one has to consider the effects of a cone passing through the boundaries between soil layers. Questions like "what is the minimum thickness of a layer, so that it is allowed to interpret the measured data straightforwardly according to rules for homogeneous material?" have to be answered. Or: "at what distance above a another layer the cone tip senses that layer and what is the penetrating distance into a layer necessary to arrive at the new steady state value corresponding to the material of that layer?"

Up to now, the answers to those questions have been highly empirical and based on a relatively small number of experiments (Robertson and Campanella, 1986). Schmertmann (1978) concludes that he is not aware of extensive research on this subject. Calibration chamber tests for sand (Schmertmann, 1978; Treadwell, 1975) show that the cone tip senses an interface between 5 and 10 cone diameters ahead and behind. They conclude that the distance over which the cone resistance is influenced increases with increasing soil stiffness. This implies that for interbedded deposits the minimum stiff layer thickness to ensure full tip resistance is equal to 10 - 20 times the cone diameter, i.e. 36 to 72 cm.

For undrained clay layers, however, the minimum thickness of a layer to generate the full cone resistance, is considerably lower: 2 to 4 times the cone diameters or 7 to 15 cm (Schmertmann, 1978; Robertson and Campanella, 1986).

Figure 4.38 presents the results of a laboratory chamber test carried out by Schmertmann (1978). The figure shows the measured cone resistance when a cone penetrometer passes from a lower to a higher relative density layer of the same sand. At a distance of about $4D$ ahead the cone tip senses the dense (stiff) layer and at a distance of about $6D$ into the dense layer the new steady state resistance is reached. Figure 4.39 shows the reverse: a dense layer on a loose layer. The influence region is about $6D$ ahead and behind.

An important application of the cone penetration test in the Netherlands is the determination of pile bearing capacity. This application also asks for judgement about the influenced region. The present state of the art is still highly empirical (Robertson and Campanella, 1986). A widely used method is the so-called $4D/8D$ approach, originally developed by Begemann. This approach states that, in order to determine the bearing capacity of a pile, a distance of $0.7D$ to $4D$ under the tip of the pile and $8D$ above the tip has to be taken into account. A full discussion, however, of the various

methods for the prediction of pile bearing capacity is behind the scope of the present work. A more detailed description is given by Schmertmann (1978) and de Ruiter and Beringen (1979).

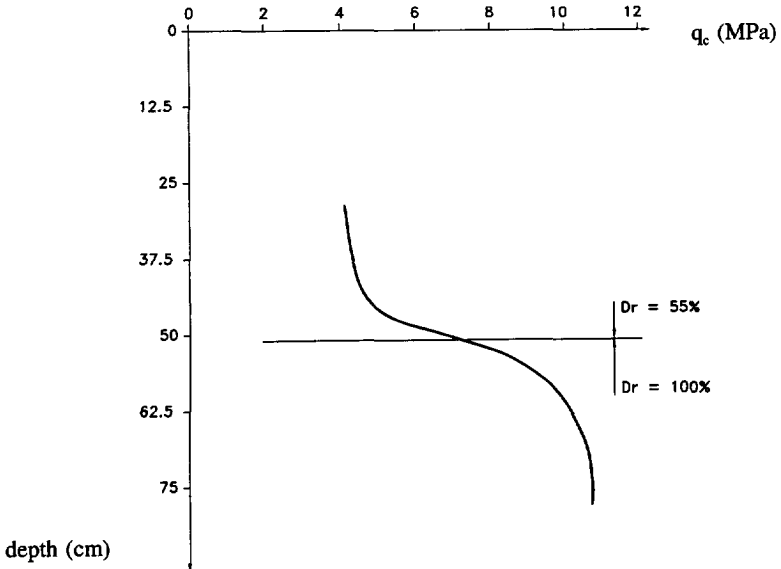


Figure 4.38 Cone penetration through loose to dense sand boundary (Schmertmann, 1978).

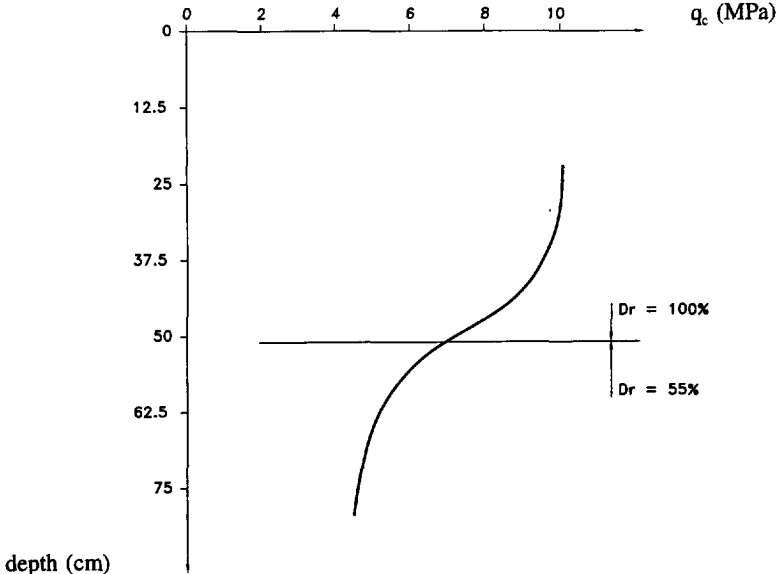


Figure 4.39 Cone penetration through dense to loose sand boundary (Schmertmann, 1978).

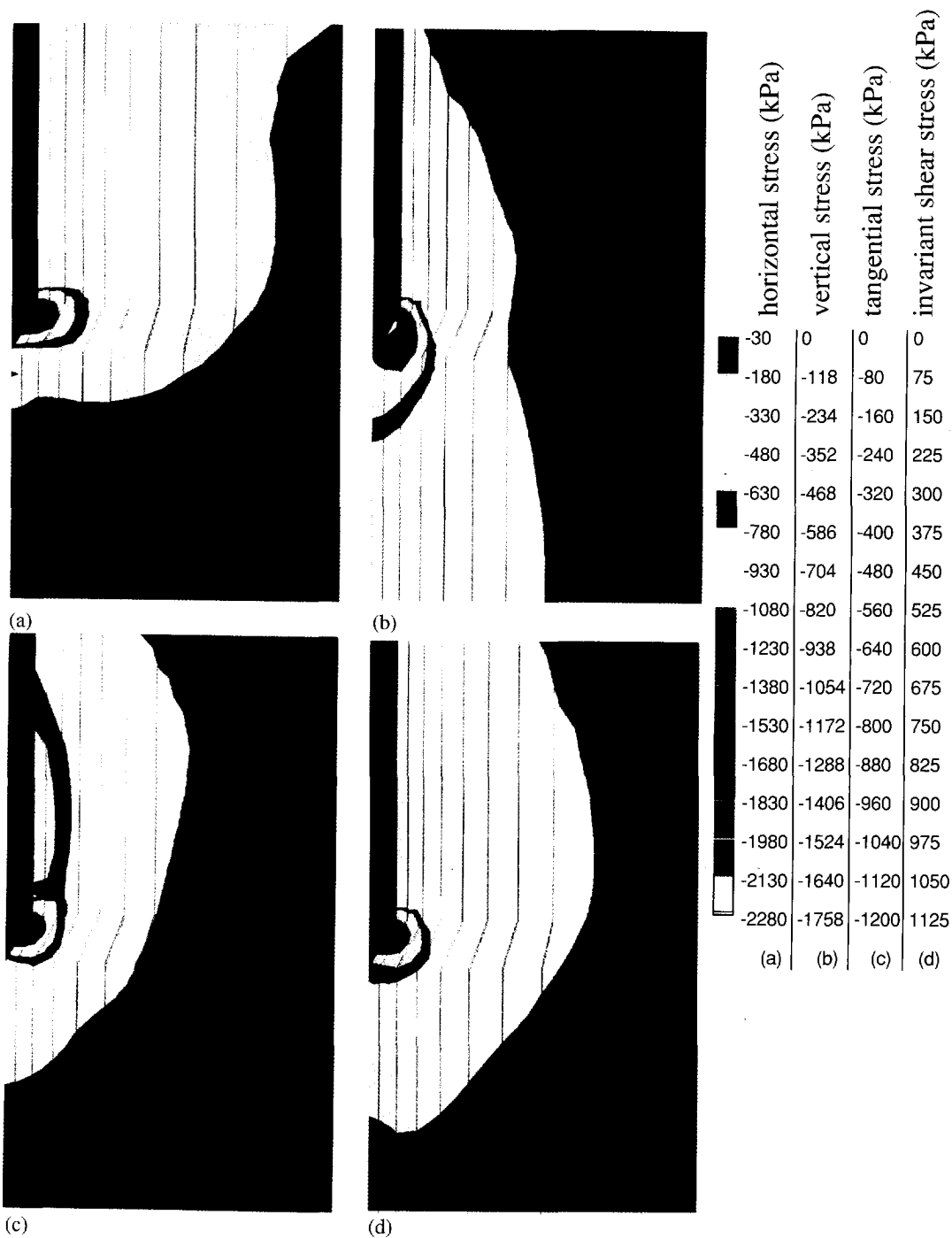
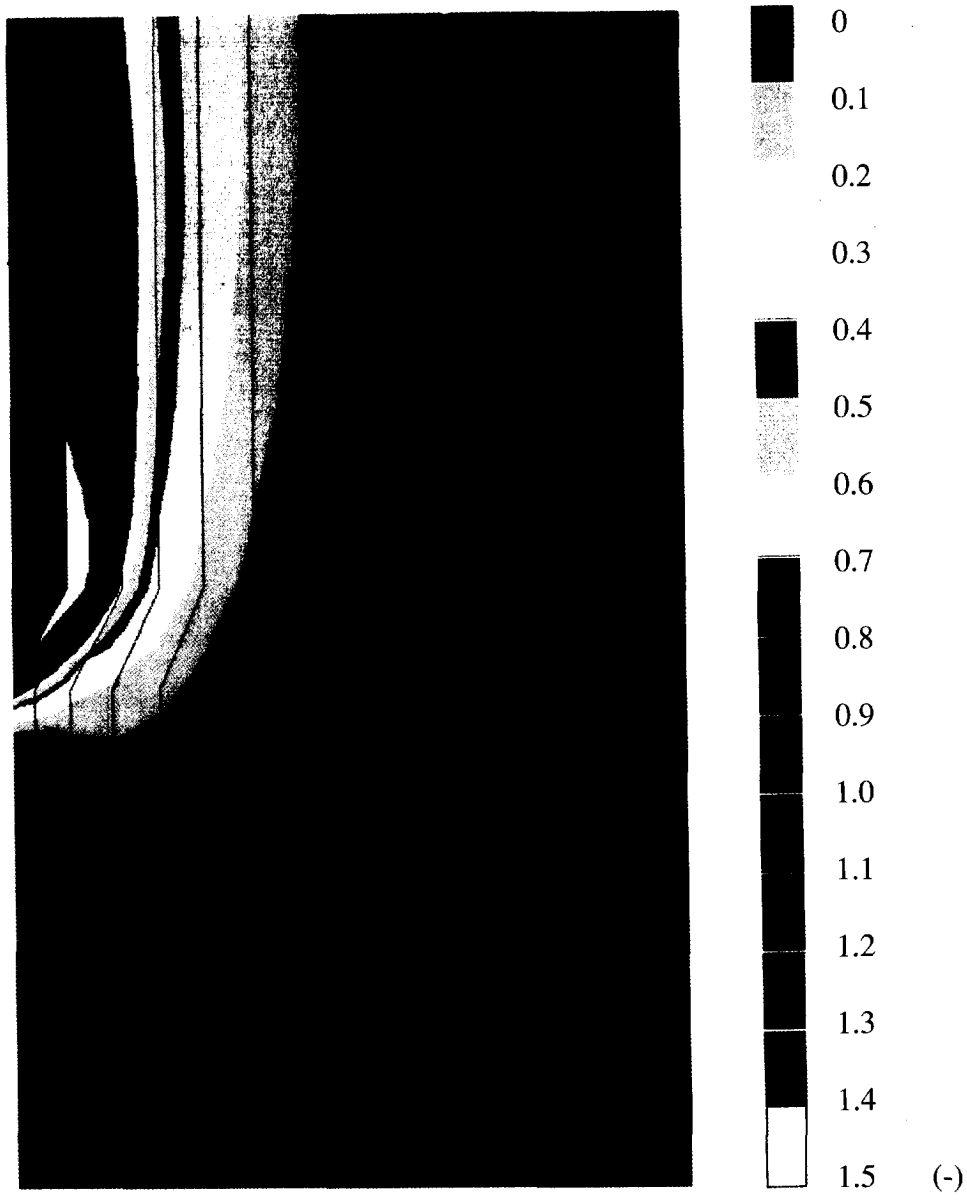


Figure 4.34 Stresses around cone during steady state penetration (run sand_5, $E = 5000$ kPa); horizontal (a), vertical (b), tangential (c) and invariant shear (d).



124 *Figure 4.35* Equivalent plastic strains around cone during steady state penetration (run sand_5, E = 5000 kPa).

In the numerical and experimental work presented in this paragraph, two systems are being studied referred to as "clay on sand" and "sand on clay". First, some numerical results of cone penetration in layered media are given. After that, the results of two experiments are described, carried out in the laboratory under controlled conditions. The numerical analysis has been carried out prior to the experiments. Therefore the conditions are not exactly identical. Based on the numerical as well as the experimental results, some conclusions will be drawn, especially focussed on the interpretation of measured data.

4.5.2 Numerical analysis of layered systems

The finite element discretization is shown in figure 4.4. The loading consists of a material flow through the mesh, introduced by prescribed material displacements at the bottom of the mesh. The initial state of stress, characterized by the initial vertical effective stress σ_{v0} and the lateral pressure ratio K_0 together with the material parameters are given in table 4.9. During the analysis it was observed that the numerical iteration process was much more unstable for Mohr-Coulomb behaviour than for the Drucker-Prager criterion. Therefore it was decided to perform the sensitivity analysis using the latter model. However, since it was concluded in paragraph 4.4 that a Mohr-Coulomb model is more convenient to analyse cone penetration in sand, at the end of this paragraph the results of one successful Mohr-Coulomb calculation are presented and compared to the Drucker-Prager results.

	clay	sand
E (kN/m ²)	2000	5000
v (-)	0.49	0.3
c (kN/m ²)	10	2
ϕ_{cv} (°)	-	30
ψ_0 (°)	-	10
ξ (-)	-	0.072
σ_{v0} (kN/m ²)	35	35
K_0 (-)	1.0	1.0
δ (°)	-	10
a (kN/m ²)	6.67	0.667

Table 4.9 Material parameters and initial stresses adopted in the calculations.

clay on sand

The first simulation is related to cone penetration from a (soft) clay layer into a (stiffer) sand layer. At the start of the analysis the clay-sand boundary is located at 46.2 mm below the tip of the cone (see figure 4.40). The load-displacement curve calculated is presented in figure 4.41. Additionally to the curve for the two-layer system, curves are given for homogeneous clay and homogeneous sand. The discontinuities of the two-layer line are related to the fact that at that specific points, modification of material properties from clay to sand takes place in the soil and/or interface elements located closely to the tip of the cone.

From figure 4.41, it can be concluded that for this particular case, 15 cm penetration into the sand layer is needed to reach a new steady state cone resistance. This is about 4 times the cone diameter. Figure 4.40 presents the position of the boundary between the layers at four different stages during penetration.

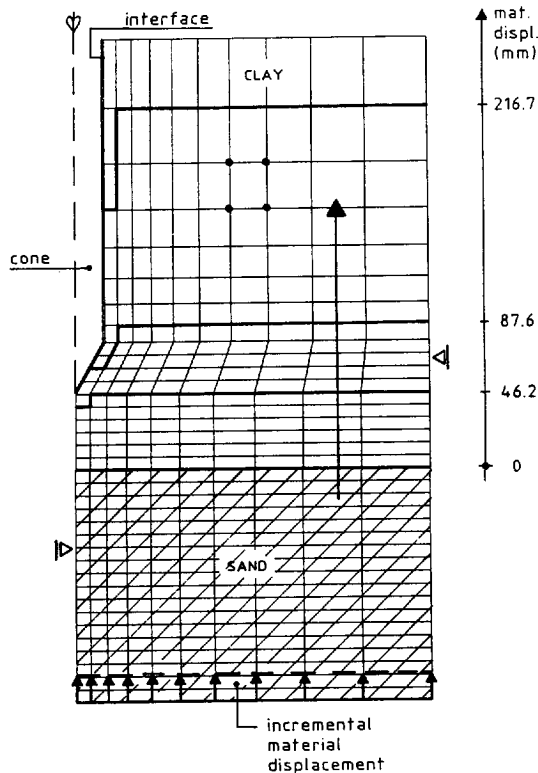


Figure 4.40 Finite element mesh and location of clay-sand boundary during penetration.

It can be seen that the boundary between both layers does not remain horizontally. In front of the cone tip hardly any influence can be noticed. However, when the boun-

dary moves upward along the tip of the cone towards the shoulder some clay sticks to the cone and a thin clay film remains between the shaft and the sand layer, even when the boundary is at a position of several diameters above the cone tip.

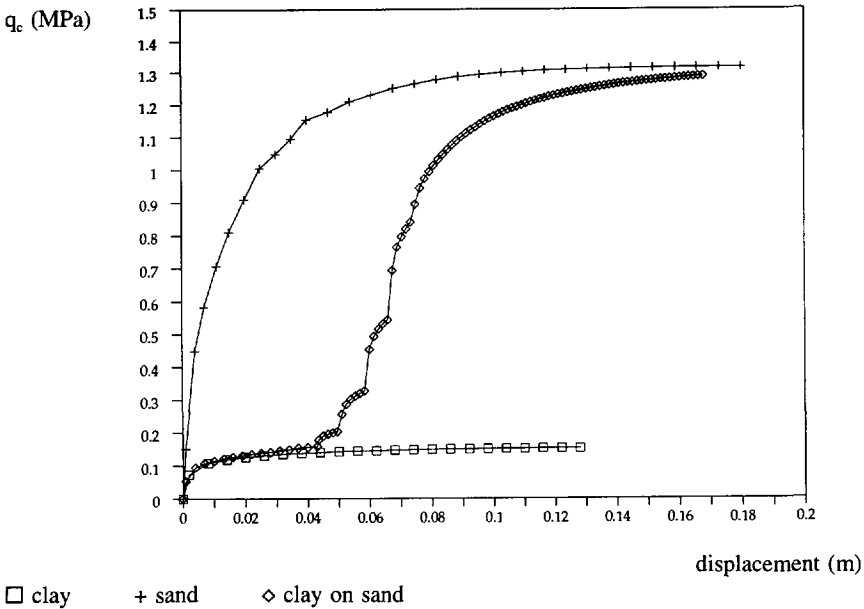


Figure 4.41 Load-displacement curves for homogeneous sand, homogeneous clay and "clay on sand".

In order to investigate the influence of the stiffness of the sand or, better, the stiffness ratio between sand and clay layer, two additional calculations are carried out: (a) the stiffness of the sand is decreased to the stiffness of the clay ($E_{sand} = 2000$ kPa) and (b) the stiffness is increased to $E_{sand} = 8000$ kPa. The calculated load-displacement curves are shown in figure 4.42.

From this figure it is clear that the slope of the curve strongly depends on the stiffness ratio. The gradient of the cone resistance per unit depth increases with increasing stiffness. For $E_{sand} = E_{clay} = 2000$ kPa, the gradient of the cone resistance is equal to about 0.095 MPa per cm penetration, while this value increases to 0.172 ($E_{sand} = 5000$ kPa) and to 0.213 MPa/cm ($E_{sand} = 8000$ kPa). Since, generally speaking, the stiffness of sand is large when compared to the stiffness of clay, the gradient of the cone resistance measured at the clay-sand is dominated by the sand layer and thus provides information about the sand stiffness.

The penetrating distance into the sand layer necessary to arrive at the new steady state value increases with increasing stiffness. For $E_{sand} = E_{clay}$ the interval during

which the cone resistance rises to the new level is limited to the vertical length of the cone tip. If the cone tip is fully embedded in the sand layer, a steady state is reached immediately. For $E_{\text{sand}} = 5000 \text{ kPa}$, the distance necessary to reach the full resistance is equal to $3D$, while this length increases to $5D$ for $E_{\text{sand}} = 8000 \text{ kPa}$.

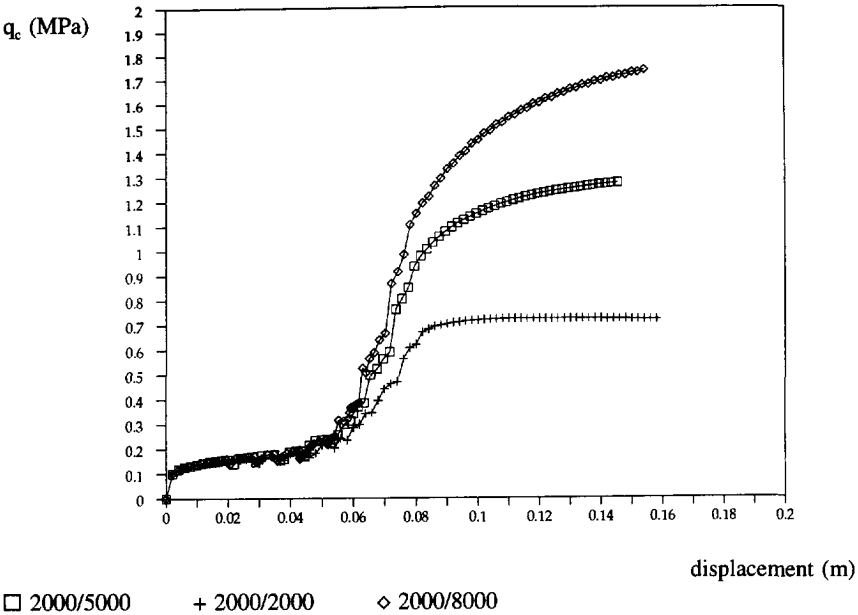


Figure 4.42 Load-displacement curves for different stiffness-ratios between clay and sand layer ($E_{\text{clay}}/E_{\text{sand}}$).

sand on clay

The second system shows the opposite: penetration from a sand layer into a clay layer. At the start of the simulation the boundary between sand and clay is located between the first and the second element at the lower side of the mesh, i.e. 177.1 mm under the tip of the cone (see figure 4.43). The load-displacement curve calculated is presented in figure 4.44. For this particular case, it can be seen that at a distance of about 10 cm above the clay boundary the cone resistance starts to drop: the cone senses the soft layer at a distance of about $3D$.

In order to investigate the influence of stiffness, the stiffness ratio between the (stiffer) sand layer and the (soft) clay layer is varied. Two additional calculations are carried out: (a) the stiffness of the sand is decreased to the stiffness of the clay layer ($E_{\text{sand}} = 2000 \text{ kPa}$) and (b) the stiffness is increased to $E_{\text{sand}} = 8000 \text{ kPa}$. The corresponding load-displacement curves are shown in figure 4.45.

It is found that the shape of the curve strongly depends on the stiffness ratio. The steepness of the curve increases with growing sand stiffness. If the stiffnesses are equal the cone senses the next layer just at the moment the tip reaches that layer. For this particular case the new steady state cone resistance is reached immediately after the tip of the cone is fully embedded in the clay. For $E_{\text{sand}} = 5000 \text{ kPa}$ the cone senses the soft layer at a distance of $3D$ and for $E_{\text{sand}} = 8000 \text{ kPa}$ at a distance of about $4D$. As can be seen in figure 4.43 at some distance ahead the relatively stiff sand is pushed into the soft clay layer. And at continued penetration some sand remains between the shaft of the cone and the clay, smeared out over a length of about 50 mm .

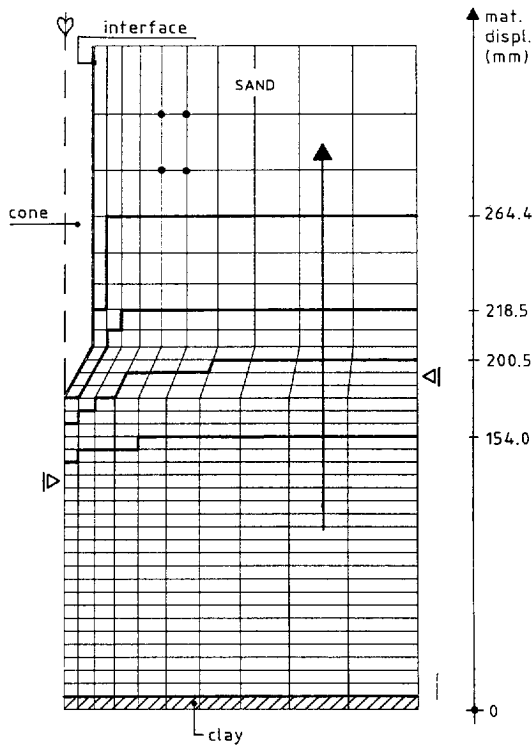


Figure 4.43 Finite element mesh and location of sand-clay boundary during penetration.

Mohr-Coulomb

In order to examine the influence of the constitutive model, one additional calculation has been performed using the Mohr-Coulomb criterion instead of the Drucker-Prager model. The parameter values are in accordance to those given in table 4.9, except that the stiffness of the sand is equal to 8000 kPa . The results are shown in figure 4.46 and have to be compared to the 2000/8000 line presented in figure 4.42.

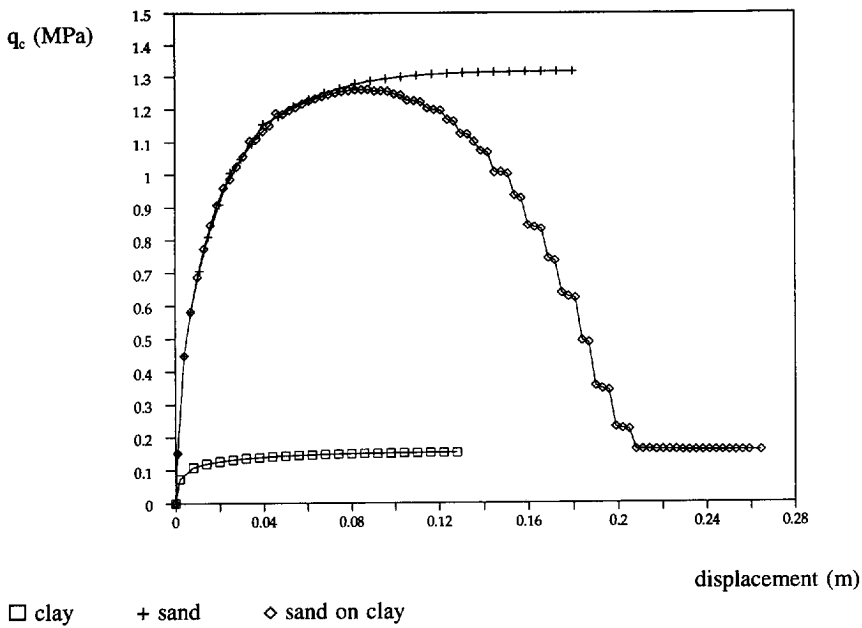


Figure 4.44 Load-displacement curves for homogeneous sand, homogeneous clay and "sand on clay".

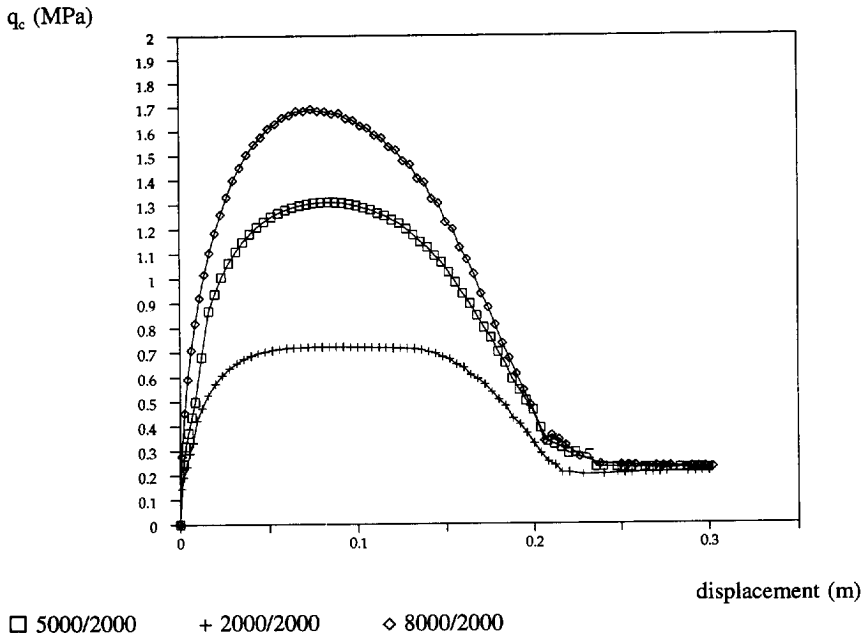


Figure 4.45 Load-displacement curves for different stiffness-ratios between clay and sand layer (E_{sand}/E_{clay}).

In figure 4.46 two lines can be distinguished: the relation between the total vertical material displacement and (a) the total vertical reaction force at the tip of the cone and (b) the total frictional force at the shaft of the cone. To derive the cone resistance the tip reaction force has to be divided by the projected area of the cone, i.e. 10 cm^2 . The skin friction can be calculated by dividing the total frictional force by the outer surface of the friction sleeve, i.e. 150 cm^2 . From figure 4.46 it can be seen that after the cone tip is at a position of about 25 cm (or 7D) in the sand layer, a new steady state is reached with respect to the cone resistance. This value is somewhat larger than the result for Drucker-Prager behaviour, i.e. about 5D.

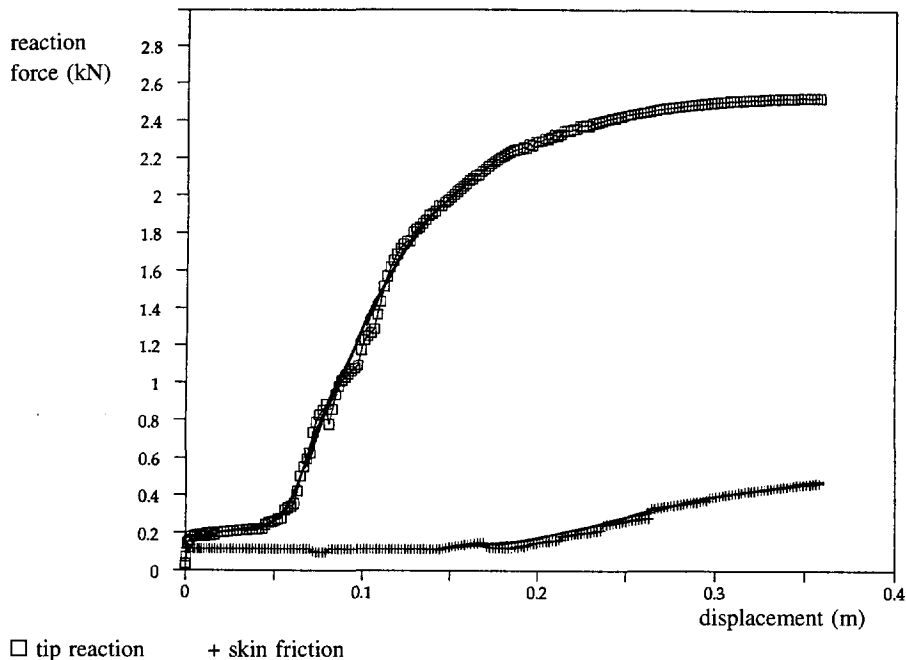


Figure 4.46 Load-displacement curves (tip reaction and shaft friction) for "clay on sand" (Mohr-Coulomb model).

4.5.3 Experiments

Introduction

The introduction to paragraph 4.5 stated, that the number of cone penetration tests in layered media, carried out under controlled conditions, is limited. Therefore, in order to validate the results of the numerical model, full scale cone penetration tests have been performed in the laboratory. Tests were conducted in a two-layer soil profile, referred to as "sand on clay" and "clay on sand". During penetration the cone resistance, the skin friction and the excess pore water pressure were registered. The deformation pattern around the penetrating cone was recorded.

Test set-up

The test chamber, specially designed for the tests, consists of four hardened glass plates (with dimensions of 1.0 m by 0.4 m and a wall-thickness of 12 mm), joined together to give a rectangular geometry with a base of 0.4 m by 0.4 m and a height of 1.0 m. A photograph of the testing facility is presented in figure 4.47. In this chamber a homogeneous soil mass is introduced.

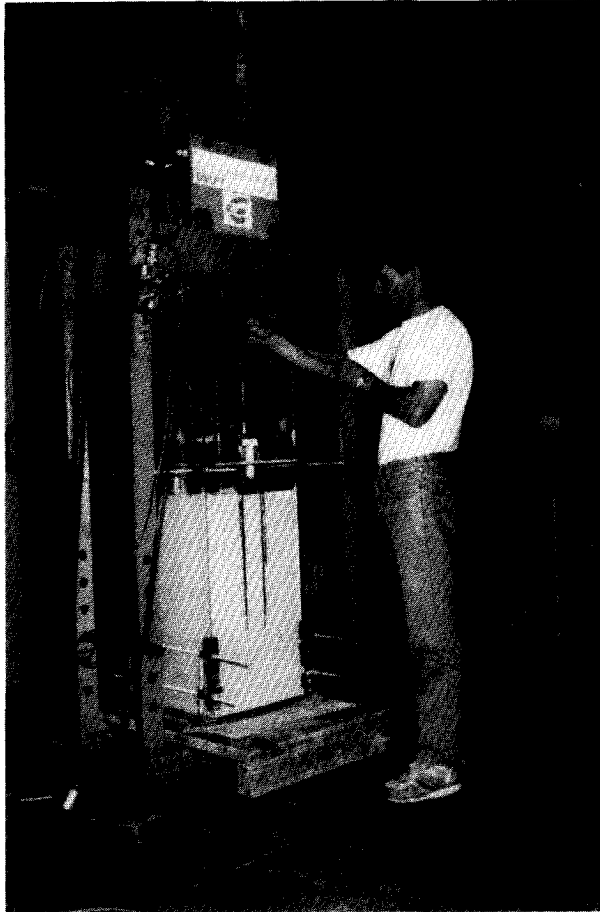


Figure 4.47 Testing facility.

Preparation of clay

To create a homogeneous clay mass with a certain strength, in the test chamber a China clay called Specwhite kaolin is introduced, initially in a slurried state at a water content far above the liquid limit. At the top of the chamber a rigid steel plate is placed and loaded by a (stepwise) increasing vertical pressure. At the top and the bottom plane of the cell as well as in the four diagonal corner axes drainage can take place. The consolidation process is controlled by measuring the settlement of the clay mass and the excess pore water pressure inside the test bin as a function of time. Constant values indicate the end of consolidation.

After about 75 % of the final strength is reached, one of the glass plates is removed carefully. At this uncovered side of the chamber a grid is plotted on the clay consisting of square-shaped blocks in order to record the deformation during penetration. The glass plate is greased with glycerine to avoid friction between plate and clay during continued consolidation and penetration.

Preparation of sand

After completion of the clay layer, underwater sand raining techniques have been used to create a homogeneous sand mass at a certain density. Since extensive studies have been carried out towards the mechanical behaviour of Eastern Scheldt sand at different densities (Laboratorium voor Grondmechanica, 1979; van den Berg, 1991c), this type of sand has been chosen for the tests. In order to be in a position to monitor deformations, the sand was sprayed with an orange or white paint, giving a rectangular grid.

Testing procedure

Two types of cones have been used (figure 4.48). A cone lengthwise cut in half was pushed downward along the glass plate at a constant penetration rate of 2 cm per second. During penetration four photographs per second were taken and a video film was made to monitor the deformation of the soil around the penetrating cone. In the center of the test chamber a real CPT (full cone) was carried out. The rate of penetration was also 2 cm per second and during penetration the cone resistance, the skin friction and the excess pore water pressure were measured. Two test series have been carried out. In the first series a clay layer was placed upon a sand layer ("clay on sand"), while the second test showed the opposite ("sand on clay").

Soil characteristics

At the end of each test series a careful "site investigation" was conducted on the soil. A number of samples were taken for subsequent classification tests, triaxial testing and direct shear testing of soil along a piece of steel in order to derive information about the frictional interface behaviour between cone and soil. In addition in-situ strengths were measured with a hand-penetrometer and a hand-torvane and moisture

contents and densities were determined at different positions. All test results are summarized in table 4.10.

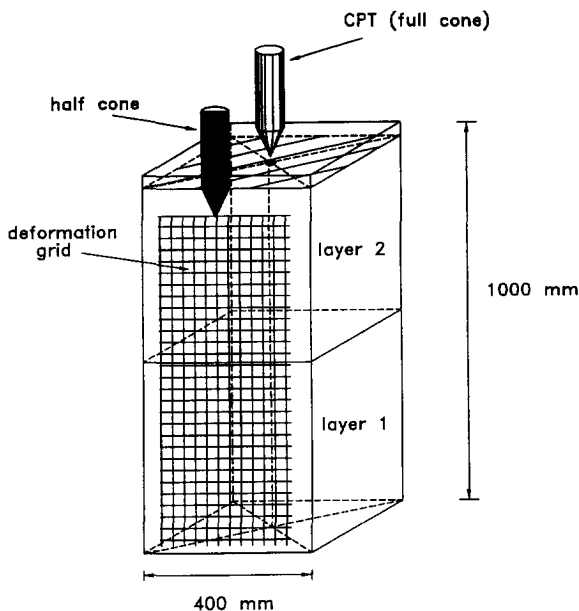


Figure 4.48 Testing facility, position of cones and "deformation grid".

clay		sand	
liquid limit	69%	min. porosity	35%
plasticity limit	38%	max. porosity	47%
plasticity index	31%	water content	23% (a) 22% (b)
water content	49% (a) 52% (b)	D_r (n)	51% (a) 55% (b)
γ (w=50%)	17.0 kN/m ³	γ_{dr} (kN/m ³)	15.6 (a) 15.5 (b)
c_u/σ_v'	0.21	E_{50}	11.5 MPa
G/c_u	200	ϕ_{peak}	34.7 ^o (a) 35.3 ^o (b)
ϕ'	23 ^o		
c'	0		
c_u	11 (a) 13 (b) kPa		

Table 4.10 Data of sand and clay (a: "clay on sand" and b: "sand on clay").

Results test "clay on sand"

In this test a clay layer with a thickness of 50.2 cm was placed upon a sand layer with a thickness of 49.8 cm. The results measured by the full cone in the center of the test bin are shown in figure 4.49.

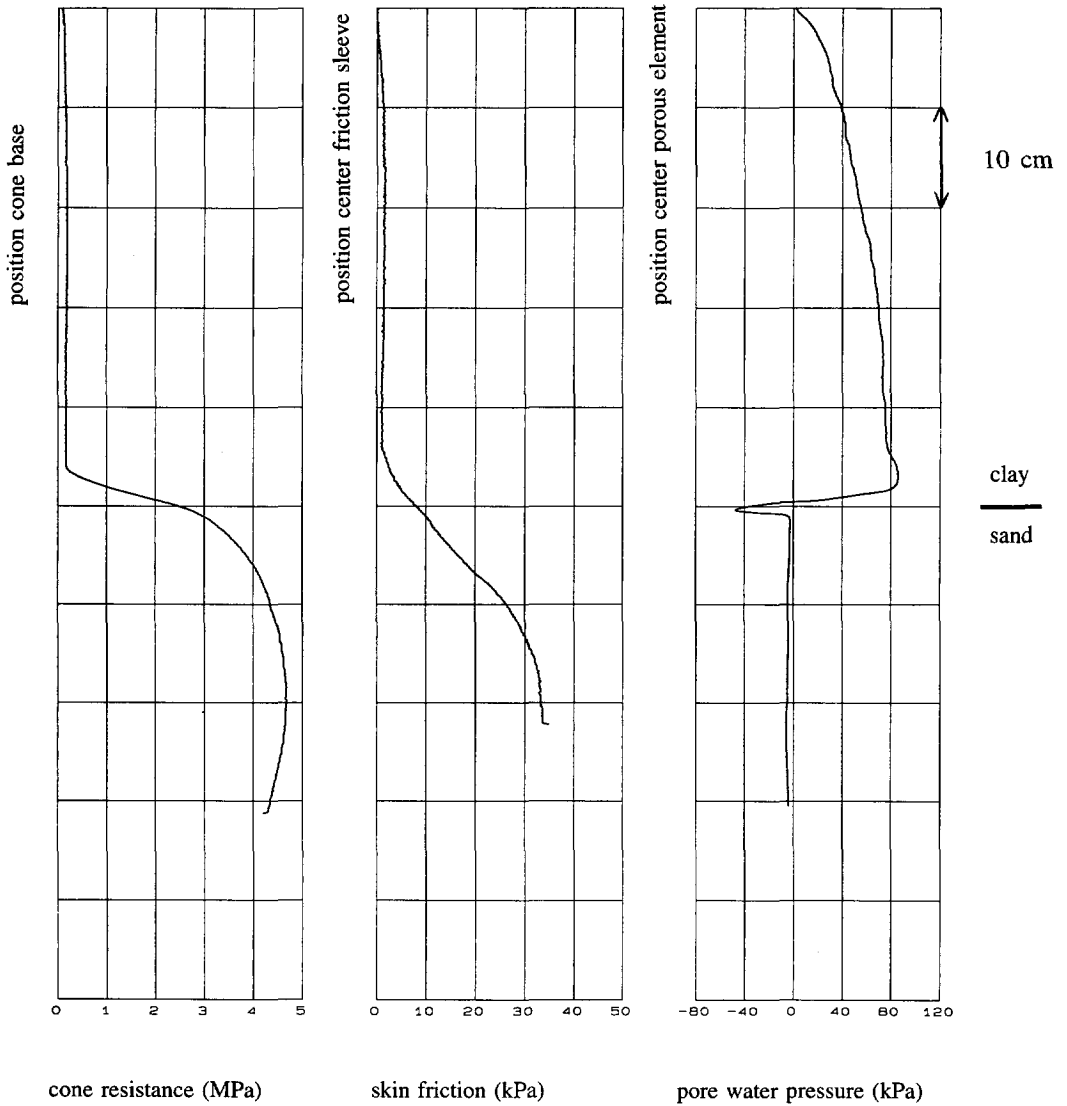


Figure 4.49 Measured results (test: "clay on sand").

The cone resistance is given as a function of the position of the cone base (the cross section at the shoulder), i.e. about 3.1 cm above the sharp point of the cone tip. The skin friction is presented as a function of the position of the center of the friction sleeve, i.e. about 7 cm above the cone base, whereas the pore water pressure is given as a function of the position of the center of the porous element, i.e. a few millimeters above the cone base (see figure 4.1).

During penetration through the top layer of clay, a steady state cone resistance is measured, varying between 180 and 200 kPa, indicating the homogeneity of the clay mass. Since the undrained shear strength of the clay is 11 kPa, a cone factor N_c is found equal to about 16. At the moment the cone tip is at a position very close to the sand boundary (about 1.5 cm or 0.5D ahead) the cone senses the stiff layer. The cone resistance starts to increase, initially approximately linear with depth. After the cone tip is at a position of about 20 cm (5-6D) inside the sand layer, a steady state is reached again. This corresponds to the calculated value of 5-7D. The gradient of the load-displacement curve near the boundary is about 0.6 MPa per cm penetration.

After the friction sleeve is fully embedded in the clay, the skin friction reaches a constant level equal to about 2 KPa. This implies that the friction ratio (1%), is somewhat small when compared to data generally accepted in engineering practice. The skin friction starts to increase at the moment the lower end of the sleeve arrives at the sand boundary. During the length of the sleeve, 13.4 cm, a more or less linear relation is measured. After that a more curved shape is found rising up to a steady state value in the sand layer of about 34 kPa, or a friction ratio of 0.8%.

The pore water pressure in the clay increases with depth up to a value of about 80 kPa. This is equal to 5-6 times c_u , which is well with agreement to experimental data collected by Robertson and Campanella (1986). The same time the porous element passes the sand boundary a sharp reduction of pore pressure can be distinguished: a reduction from +80 kPa to -50 kPa over a length of 2 cm. This is related to the phenomenon found in paragraph 4.4: when starting penetration in a frictional material, just above the shoulder of the cone a sharp stress relief occurs. At enlarged displacement it can be seen that a small negative pore pressure remains, caused by dilatancy effects in the sand. This is related to the fact that the in-situ density is somewhat larger than the critical density ($\psi_0 \approx 5^\circ$). As the permeability of the Eastern Scheldt sand is equal to about $8 \cdot 10^{-5}$ m/s (SCW, 1978), the measured value of about 5 kPa is of the same order of magnitude as to the calculated results presented in paragraph 4.4.2.

Figure 4.50 shows the deformation around the demi cone at four different stages. In clay the deformation is limited to a very small zone around the cone. Outside a region of about 1.5D around the cone no visible deformation effects can be distinguished. This is in agreement with results derived by other investigators, who carried

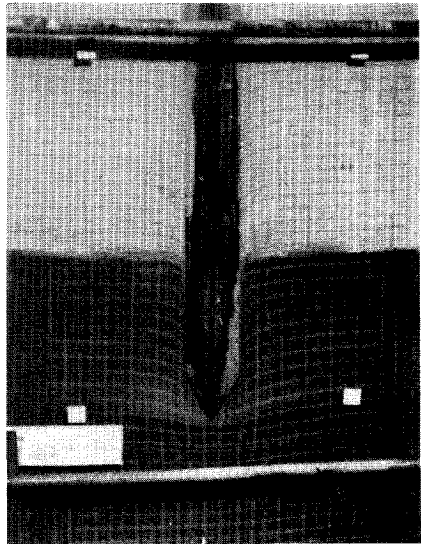
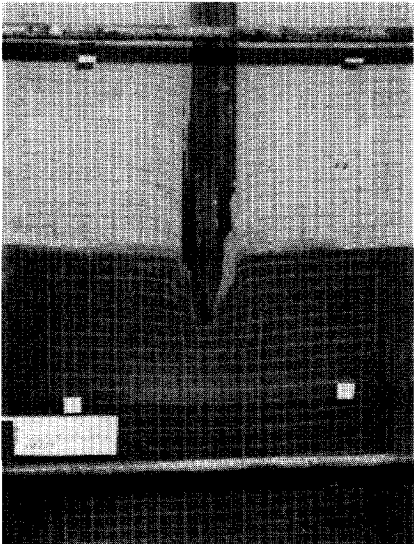
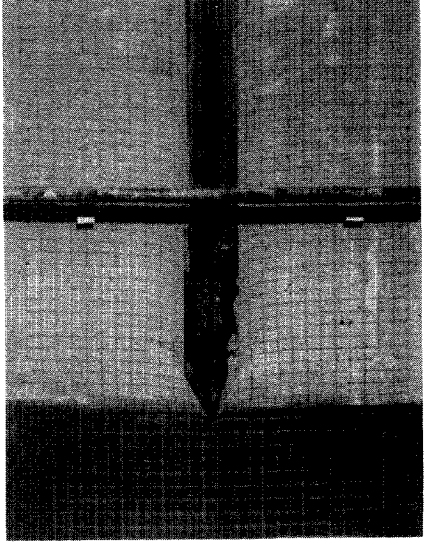
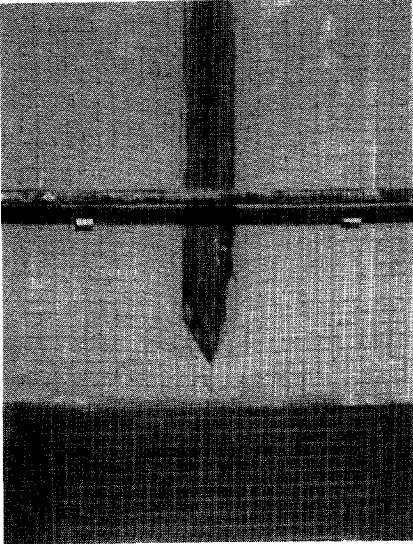


Figure 4.50 Deformation around cone (test: "clay on sand").

out tests in homogeneous clay. An overview is given by Harder (1989). In addition, there is hardly any visible effect before the tip of the cone reaches the sand layer. When the cone enters the sand layer, the influenced region becomes much larger, especially in front of the cone tip: deformation can be seen up to about $2D$ ahead. Although the clay is extremely soft when compared to the sand, over a few centimeters into the sand layer, a thin clay film is attached to the cone. This effect, which is visualized in figure 4.51, is in agreement to the calculated result, presented in figure 4.40.

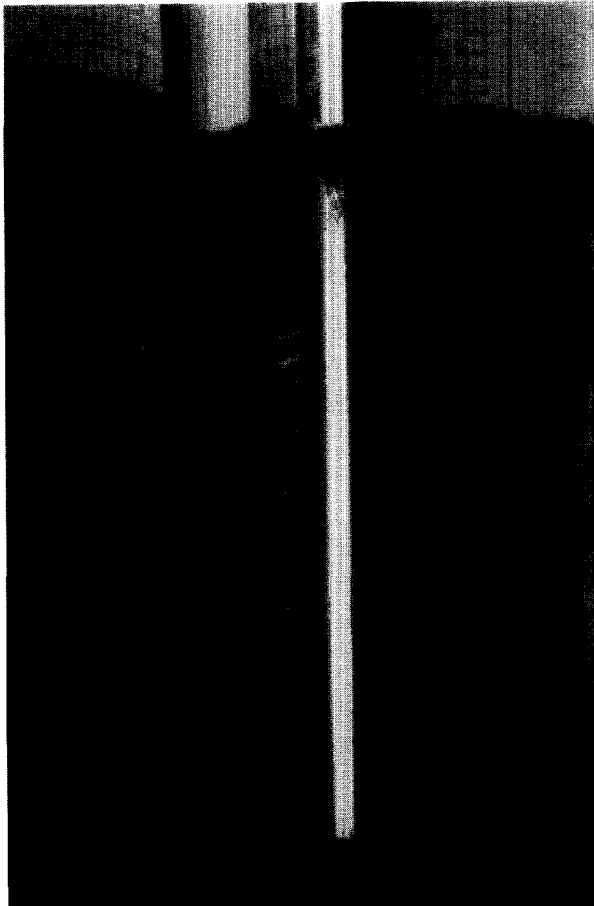


Figure 4.51 Clay film attached to cone at interface between sand and cone.

Results test "sand on clay"

The results of the second test, a relatively stiff sand layer on a soft clay layer, are shown in figure 4.52. The thickness of the clay layer is 49.5 cm and that of the sand layer is 45.9 cm.

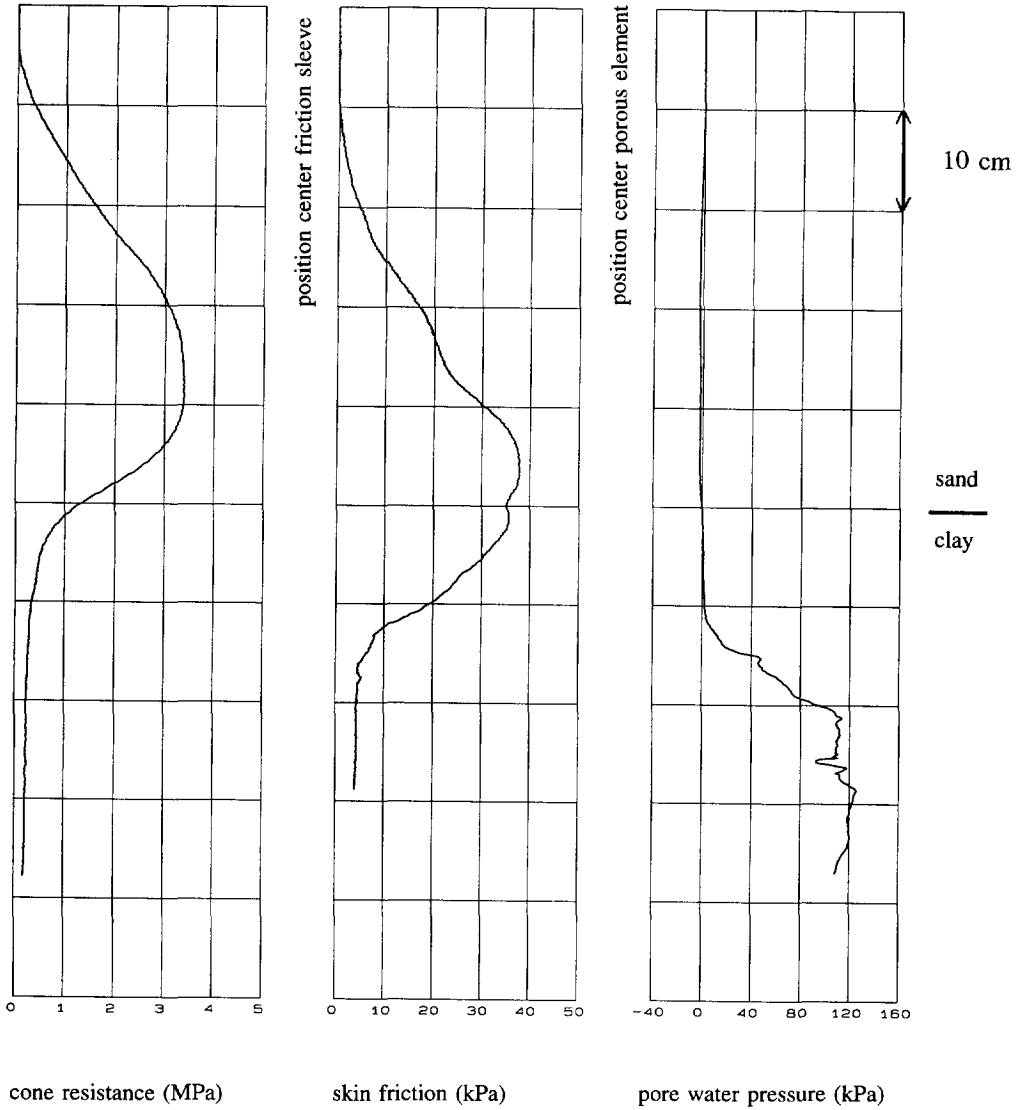


Figure 4.52 Measured results (test: "sand on clay").

In figure 4.52 the cone resistance is presented as a function of the position of the cone base, the skin friction as a function of the position of the center of the friction sleeve, while the pore pressure is given as a function of the position of the center of the porous element.

Due to boundary effects caused by the free surface, the cone resistance is not at the steady state value yet, at the moment the influence of the soft clay layer comes into being. It can be concluded from the former test ("clay on sand") that the steady state resistance would have been about 4.5 MPa. Based on this a hypothetical curve can be drawn for homogeneous sand. From this curve and the measured curve, it can be concluded that the cone senses the soft clay layer at a distance of about 15 cm (cone tip) or 18 cm (cone base). A new steady state cone resistance is reached when the cone tip has penetrated into the clay layer over a length of about 10-15 cm. The steady state cone resistance is equal to 200 kPa, or $N_c = 16$ ($c_u = 12.5$ kPa).

The friction ratio in sand increases from less than 0.5% just beneath the free surface to about 0.8% at some decimeters inside the sand mass. This depth-effect can be explained by the fact that the vertical position of cone tip and friction sleeve are different. The friction ratio in clay at steady state penetration is equal to about 2%, as the measured skin friction is about 4 kPa.

During penetration in the sand layer again some negative pore water pressures are measured (under-pressure), about 2-4 kPa, indicating dilatancy effects in the sand. Another interesting phenomenon is related to the fact that the increase of pore pressure which is inherent to penetration in clay, only starts after the porous element is at a position of about 10 cm beneath the undisturbed clay boundary. This clearly indicates that sand is pushed downward into the soft clay layer. At continued penetration into the clay layer a more or less constant value is found equal to 100-120 kPa. Some unstable behaviour can be recognized.

The deformation pattern around the penetrating cone is shown in figure 4.53. Before the cone enters the clay layer some sand is pushed downward into the soft clay layer. Figure 4.54 shows a picture of the hole created by the cone after the cone itself has been removed. This photograph shows that indeed over a length of about 10 cm into the clay layer a sand cylinder with a thickness of about 1 cm surrounds the cone completely. Some more sand is taken downward deeper into the clay layer, as the picture shows some discontinuously located pieces of sand. Apparently, at continued penetration into the clay layer, some pieces of sand come free from the cone, causing some unstable behaviour, especially in the measurement of pore water pressures.

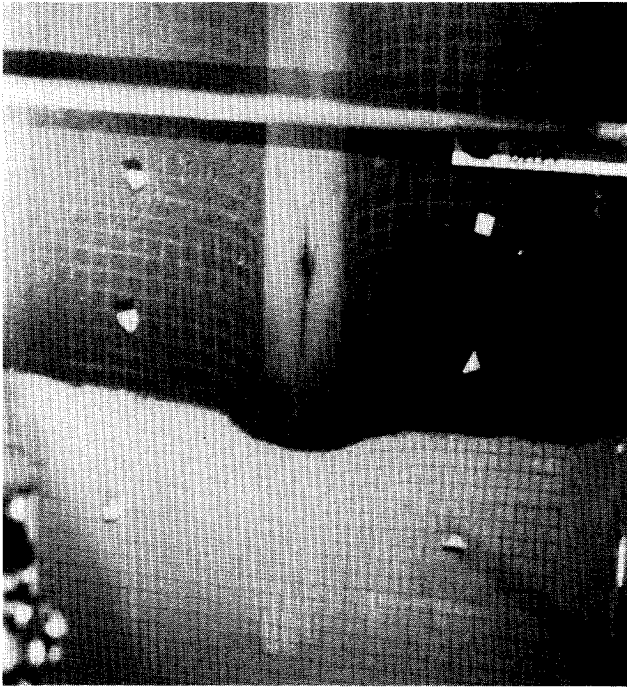


Figure 4.53 Deformation around cone (test: "sand on clay").

4.5.4 Conclusions

The results of the numerical analysis and the experiments indicate that a cone penetrating in frictional material senses a soft clay layer at a distance of 4-5D. To reach the full steady state cone resistance in a frictional layer, about 6-7D penetration into that layer is needed. Those values, however, correspond to the specific situations analyzed. The results strongly depend on the stiffness ratio between the layers. If, for instance, the stiffnesses coincide, the cone does not sense the next layer in advance. Based on this, the 4D/8D method, used as a general rule to determine the bearing capacity of a foundation pile, can be criticized. It is recommended to start a discussion towards an enhanced design rule.

The results imply that the thickness of interbedded stiff frictional deposits to ensure full tip resistance is at least 12D or 40-50 cm. For undrained clay layers, however, the minimum thickness is considerably lower. Both the numerical model and the experiments indicate that a thickness of only a few diameters (10-15 cm) is enough to generate full resistance.

The gradient of the cone resistance per unit depth in a region around a layer-boundary depends on the stiffness ratio between both layers. Since the stiffness of the clay layer is negligible when compared to the stiffness of the sand layer, the gradient can be regarded as a measure for the stiffness of the sand. However, a problem arises if the boundary is not a distinct line but rather a smooth transition. To be sure that it is allowed to interpret the measured values around the boundary according to the philosophy of this paragraph (the boundary is a distinct line), geological knowledge of the site is needed or soil samples have to be taken.

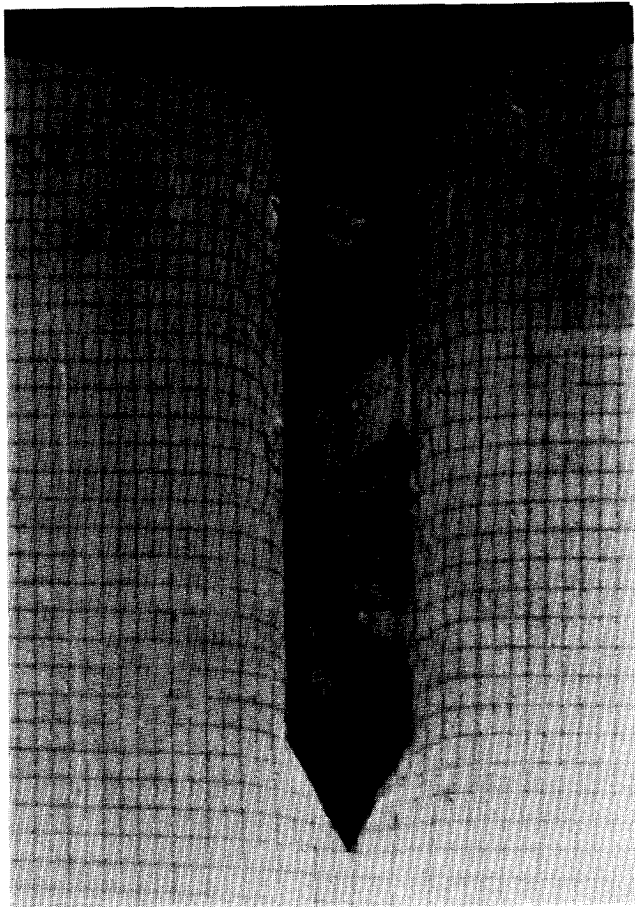
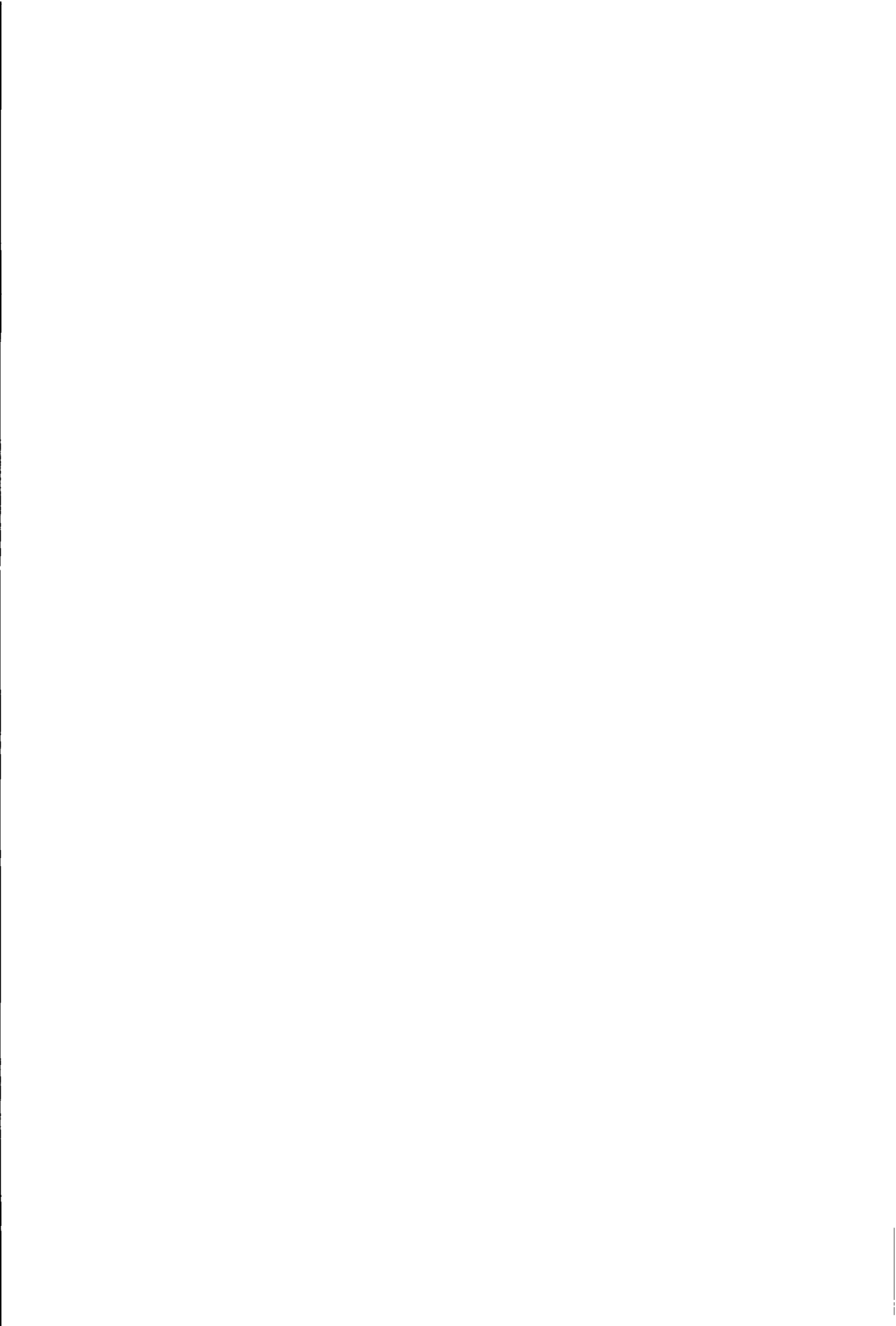


Figure 4.54 Hole created by the cone (test: "sand on clay").

Although it was concluded in paragraph 4.4 that a Mohr-Coulomb failure criterion is much more convenient to analyse cone penetration in sand, in most of the calculations presented in this section use was made of the Drucker-Prager model. During the analysis it was observed that the numerical iteration process for the Mohr-Coulomb criterion was more unstable than for the Drucker-Prager one. Stabilization of the numerical process, when a layer boundary passes the cone tip, can be achieved by defining the constitutive behaviour of an element in terms of an overlay model. Depending on the exact location of the boundary inside an element, the total material behaviour is composed by a certain percentage of material A and a complementary percentage of material B. It is advisable to elaborate this concept in more detail.



5. Sampling disturbances in soft clay

5.1 Introduction

To assess the mechanical properties of the subsoil, there are two fundamental different ways of investigation: in-situ measurement (CPT, cone-pressuremeter, dilatometer, Ménard pressuremeter) and determination in the laboratory (triaxial testing, simple shear testing, oedometer testing). For the second way of investigation soil samples are needed. Disturbances during the sampling process itself are mainly caused by the area-ratio of the device (i.e. the outer diameter of the sampling device divided by the diameter of the sample) and the interface friction between soil and sampler. In order to quantify those influences calculations have been carried out both for a thin-walled Piston Sampler (i.e. a hollow steel cylinder with a wall-thickness of 1 mm) and for the Delft Continuous Sampler (see figure 5.1). The inner diameter of both devices is 66 mm. The area-ratio of the Piston Sampler is negligible, but there is friction both on the inside and on the outside of the apparatus. On the other hand, the area-ratio of the Delft Sampler is much larger, but the interface friction on the inside is limited to a small region around the tip of the device. The differences are visualized in figure 5.2.

In addition full scale tests have been carried out in the laboratory to validate the numerical results.

5.2 Delft Continuous Sampler

Taking soil samples from the bottom of a borehole, which is a traditionally accepted method, has two important disadvantages. First, the soil to be sampled may be disturbed by the drilling operations prior to sampling. Second, soil samples are taken at discrete levels. Only limited information is obtained for the soil located between sample levels.

To overcome these problems the continuous sampling technique has been developed. The full length of the sample is obtained in one continuous operation. The Delft Continuous Sampler, for instance, is capable to receive samples up to a maximum length of about 25 m. A continuous profile of the sub-soil is obtained. It permits detailed examination of microstructures, like lenses and laminations (Begemann, 1966).

To prevent soil plugging and to obtain long undisturbed soil samples, the friction between the sample and the tubes must be negligible. To achieve this, the Delft sample is enclosed in a sleeve. Figure 5.1 presents a cross-section of the Delft

Sampler and its main components. The sleeve is stored in a chamber situated in the bottom assembly. It is pulled through a narrow slit and attached to a floating piston. When the sampler moves into the ground, the sleeve rolls down, wrapping up the sample like a sausage. Between this sausage of soil and the inner tube a specially designed drilling mud is applied to eliminate friction between sample and tube. For lateral support of the sample, the density of the mud is adapted to fit the local soil conditions.

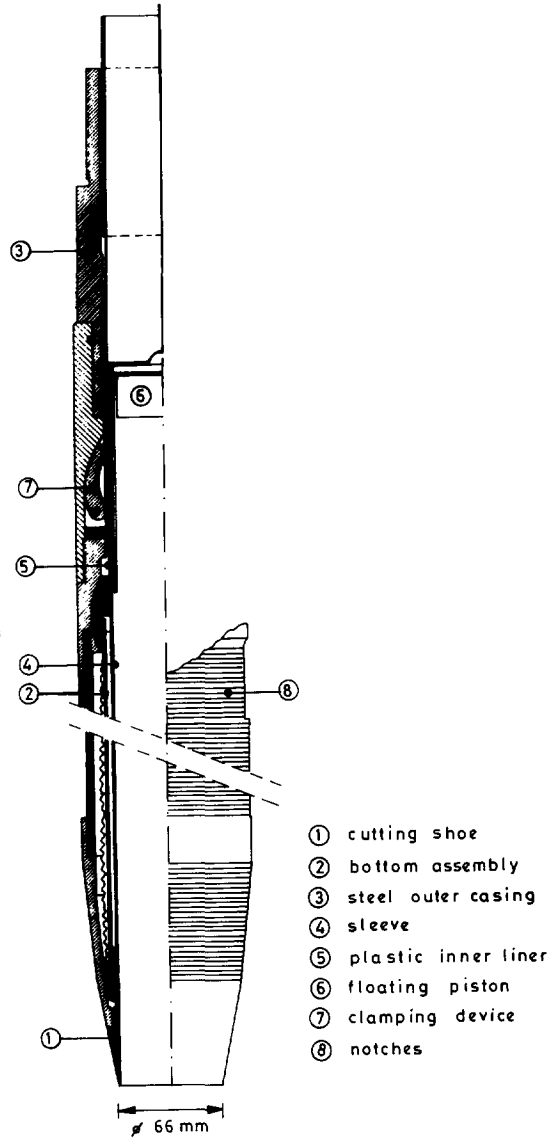


Figure 5.1 Cross-section of Delft Continuous Sampler.

In this way the sleeve entirely envelops the soil sample entering through the cutting shoe. As the sampling proceeds, extension tubes (steel outercasing) are connected to the bottom assembly to form a string. Plastic inner liners are installed inside the extension tubes. Notches are machined in the skin of the bottom assembly to prevent vibration of the sampler during penetration. A clamping device is activated automatically on pulling the extraction tubes. The clamps pinch the plastic liners and prevent the soil sample from dropping out of the sampler. The sampling process is controlled by monitoring (1) the drilling mud consumption, (2) the force required to keep the piston stationary and (3) the penetration resistance.

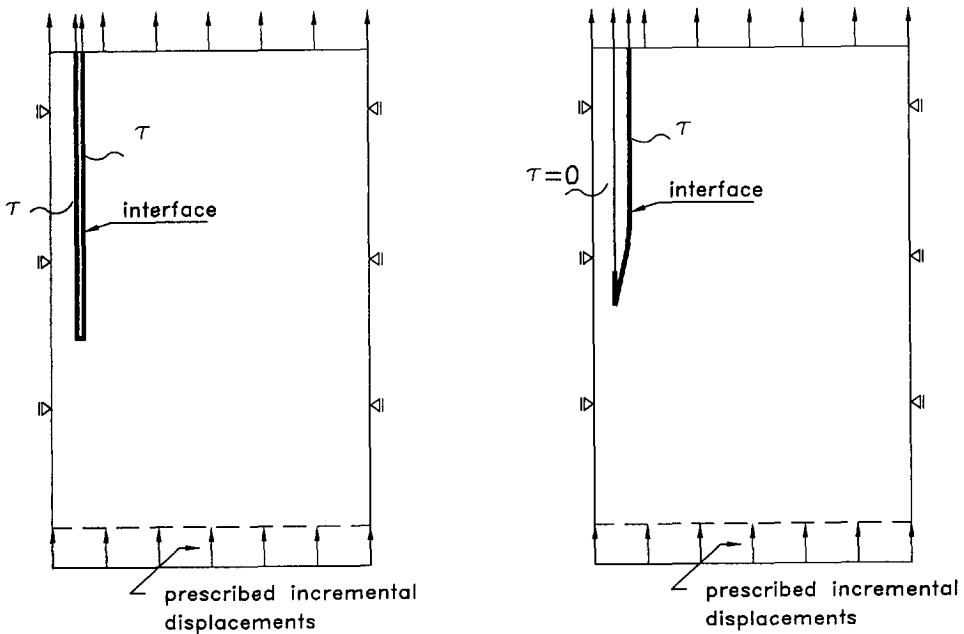


Figure 5.2 Axi-symmetric models for Piston Sampler (left) and Delft Sampler (right).

5.3 Numerical analysis of sampling process

The axi-symmetric models for the Piston Sampler and the Delft Sampler are shown in figure 5.2. The finite element discretizations consist of about 400 four-noded continuum elements to model the soil. Between sampler and soil zero-thickness interface elements are incorporated in the model to account for the frictional interface behaviour. The loading consists of a material flow through the fixed mesh, introduced by prescribed displacements at the bottom of the mesh. The load-displacement curve is

calculated as well as stress and strain fields around the device until a steady state situation is reached, i.e. soil introduced at the bottom of the mesh has moved out of the mesh at the top. In the mesh the length of the device is 420 mm, measured from the top of the mesh to the tip of the cutting shoe.

A linear elastic perfectly plastic von Mises model has been used to model the constitutive behaviour of the soil. The friction mechanism is described by elastic shearing behaviour up to a specified level. If the shear stress exceeds this level (the adhesion of the soil a), plastic deformation occurs. The following material parameters have been adopted:

Young's modulus E :	6100 kPa
Poisson's ratio ν :	0.49
undrained cohesion c_v :	20.3 kPa
interface adhesion a :	4.4 kPa

No initial stresses have been introduced into the models.

Load-displacement

The calculated load-displacement curves are presented in figure 5.3. The push-in force, indicated in the figures, is the total vertical force acting on the sampler. For the Piston Sampler three phases can be distinguished. During phase 1 the interface elements on the outside of the device fail in shear, from the bottom upward.

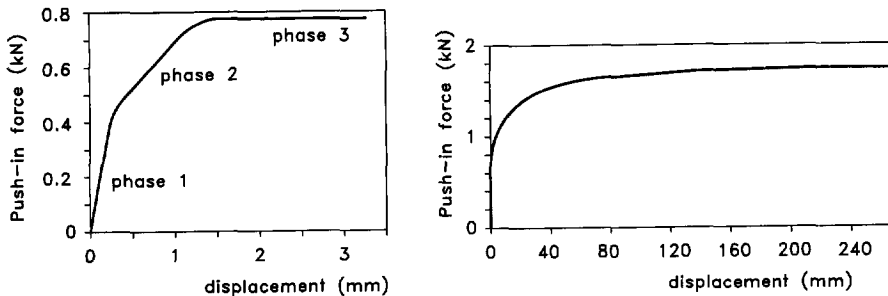


Figure 5.3 Load-displacement curves calculated for Piston Sampler (left) and Delft Sampler (right).

During phase 2 the same mechanism is found at the inside of the sampler, while phase 3 corresponds to steady state penetration of the sampler. For this particular length of the device (420 mm), the push-in force during this phase is 0.77 kN. The

reaction force of the Piston Sampler is linearly dependent on the interface adhesion, since the contribution of the tip resistance is negligible. For the same length of the device, the vertical force acting on the Delft Sampler during steady state penetration is about 1.6 kN, subdivided into 0.45 kN, caused by friction, and 1.15 kN, caused by tip resistance.

Deformation

The most significant deformation mode of the soil moving into the sampler is one-dimensional compression: the sample shortens. The incremental displacements during steady state penetration, presented as relative quantities with respect to the displacement of the sampler, are presented in figure 5.4. Both figures have not been drawn to the same scale: the aim of this way of presentation is to show the most significant mechanisms.

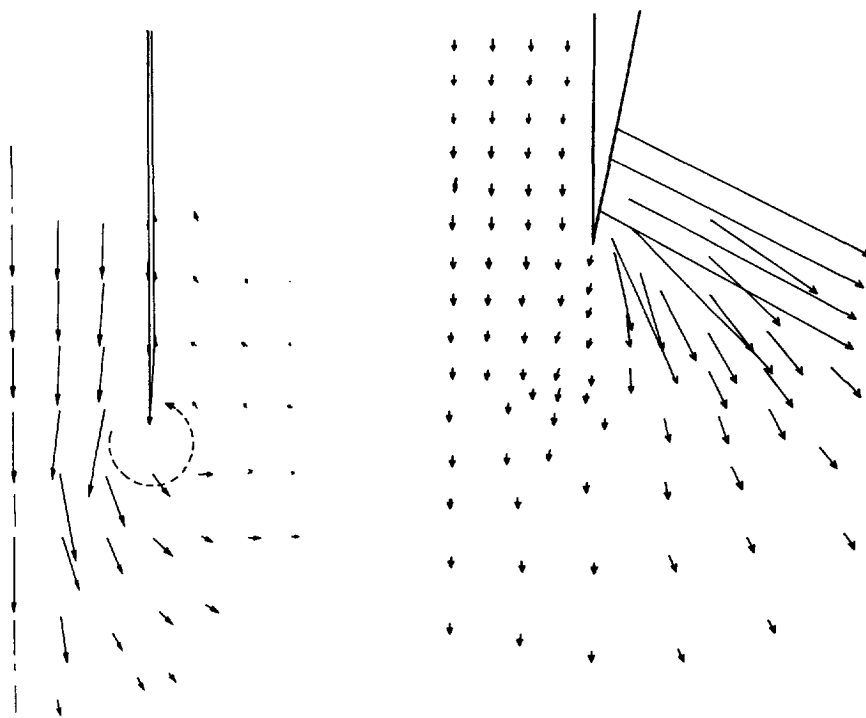


Figure 5.4 Incremental displacements during steady state sampling for Piston Sampler (left) and Delft Sampler (right).

For the Delft Sampler large deformations occur on the outside of the sample, caused by the relatively large area ratio. Soil is pushed aside to make room for the device. As can be seen, for a particular cutting angle of 11 degrees (standard angle for Delft Sampler) there is hardly any influence of this "area ratio"-effect on the quality of the sample.

The amount of shortening is strongly dependent on the inside friction of the system. To investigate the influence, three calculations have been performed for the standard Piston Sampler. Different values for the interface friction, defined by the ratio R , have been introduced into the model.

$$R = \frac{\tau_{max}}{c_u} \tag{5.1}$$

For the specific geometry as presented in figure 5.2 and an R -value equal to 0.125, a shortening of the sample during steady state sampling, has been calculated of 0.1%. The amount of shortening increases to 0.6% (for $R = 0.22$) and even to 47.6% (for $R = 0.5$). For the third case the interface friction nearly causes complete soil-plugging.

Stresses

Similar to the deformations, also the stresses are strongly influenced by the interface friction. Except inside a very thin interface zone between sampler and soil, for a Piston Sampler and an R -value of 0.125 no plasticity occurs in the soil itself. Increasing the R -value to 0.22, the invariant shear stress reaches the undrained shear strength of the soil in a small region in the center-line underneath the device at a distance of slightly more than one sampler-radius. This is shown in figure 5.5.

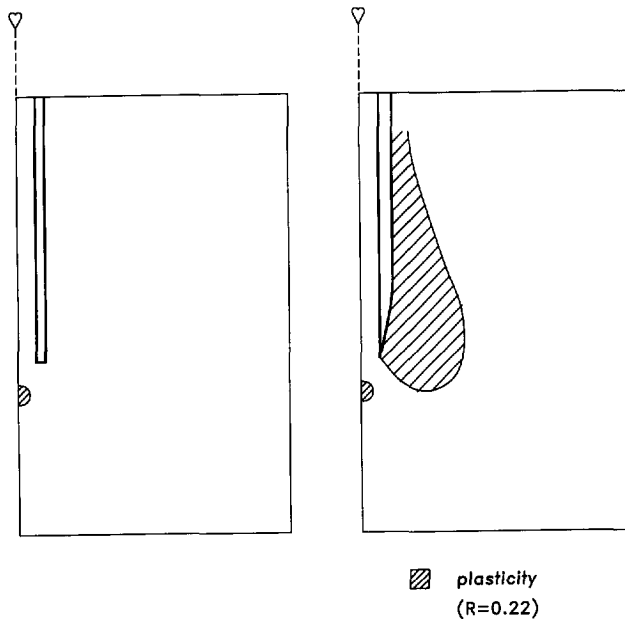


Figure 5.5 Plasticity during steady state penetration for Piston Sampler (left) and Delft Sampler (right).

Introducing an R-value into the model equal to 0.5 results into plasticity over the whole cross-section of the sample. Inside the apparatus unloading occurs and the stress state becomes elastic again. However, reaching the undrained shear strength indicates that the micro-structure of the clay has been influenced non-reversibly. For the Delft Sampler, in front of the device a mechanism has been calculated identical to that of the Piston Sampler (figure 5.5). In addition, at the outside of the device, a large plastic zone occurs, caused by the large outside displacements (see figure 5.3). The outside displacements are responsible for relatively large compressive radial stresses around the sampler, presented in figure 5.6.

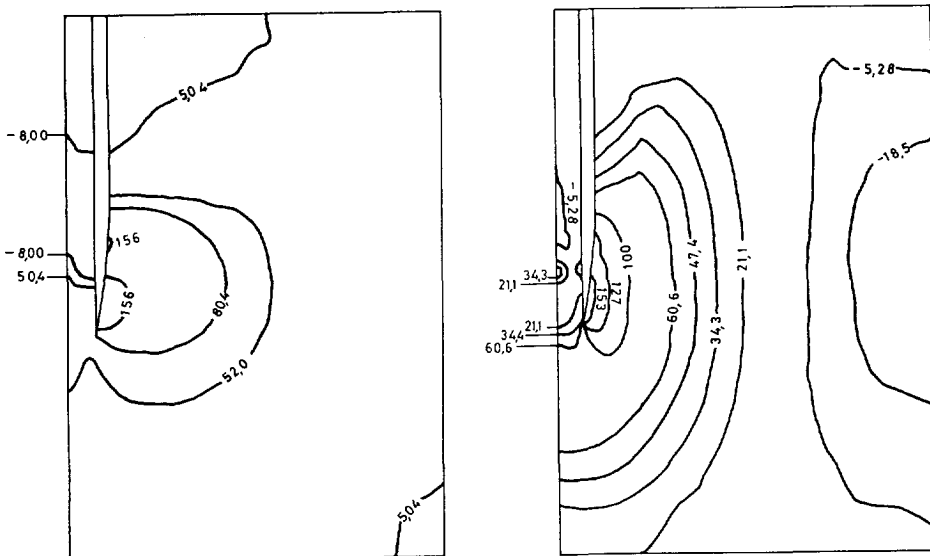


Figure 5.6 Radial (left) and vertical (right) stresses around Delft Sampler.

5.4 Experiments

To validate the results of the numerical analysis, sampling tests were conducted in homogeneous clay. A Piston Sampler and a Delft Sampler lengthwise cut in half were pushed along a glass wall into a homogeneous clay mass. A grid was printed on the clay to visualize the deformations. In addition, standard (full) sampler apparatuses were pushed into the same clay mass, to determine the material parameters. All tests were carried out twice, referred to as series 1 and series 2. The testing facility introduced in paragraph 4.5.3 was used.

Test set-up

The testing facility (figures 4.47 and 4.48) consists of four hardened glass plates joined together to give a rectangular bin with a base of 0.4 m by 0.4 m and a height of 1.0 m. The bin was filled with a clay slurry which was a mixture of 125 kg Spec-white Kaolin powder and 93% water. After the bin had been filled, the clay slurry was consolidated to a certain strength. The result was a homogeneous, fully saturated and consolidated clay mass. In the first series the water content was 44.29% and in the second series 43.52%. The average liquid limit and plastic limit were 59.1% and 30.6% respectively.

Multi-stage consolidated undrained (CU) triaxial tests were carried out to derive the mechanical properties of the clay. The most significant results are summarized in tabel 5.1. It is remarkable that the undrained shear strength measured in-situ (using a pocket-penetrometer and a hand-torvane) is somewhat less, ranging from 15 to 18 kPa.

	series 1	series 2	average
c_u (kPa)	20.4	20.2	20.3
G_{50} (kPa)	7400	4800	6100

Table 5.1 Material parameters of clay in test bin.

After 90% of the consolidation process had been completed, the glass plates were carefully removed to print the grid on the clay. Before replacing the glass plates, they were lubricated with silicone oil to minimize the friction between clay and glass plate.

All tests were performed with at a penetrating rate of 1 cm per second. The force necessary to push-in the samplers was measured as a function of the penetrating depth. Furthermore, photographs were taken and a video film was made of the deforming grid. In the second series a pore pressure transducer was placed in the clay underneath the Delft Sampler.

Load-displacement

The load-displacement curves measured during test series 2 are presented in figure 5.7. Since the resistance of the Piston Sampler is fully determined by interface friction, the adhesion between soil and device can be back-calculated from the slope of the load-displacement curve to be 4.4 kPa.

The load-displacement curve measured for the Delft Sampler shows two different parts. At the discontinuity, the thickest part of the Delft Sampler passes the surface

of the clay. The slope of the first part of the curve is partly determined by interface friction and partly by the area ratio of the apparatus. During the second part of the curve, the slope is fully determined by the additional interface friction working on the outside of the straight part of the device. The values corresponding to a penetrating depth of 42 cm have to be compared to the results of the numerical analysis. At that particular depth, the experiment shows a value of 1.81 kN, whereas the numerical model gives a somewhat lower value of 1.6 kN. Maybe, the difference is caused by the notches machined on the outside of the sampler (see figure 5.1).

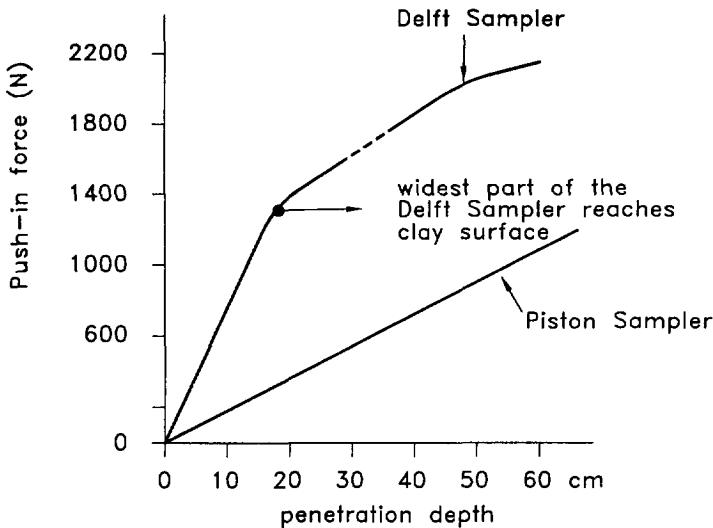


Figure 5.7 Load-displacement curves for Piston Sampler and Delft Sampler measured during test series 2.

Deformation

Figure 5.8 shows the deformed grid during penetration of the demi samplers. The photo taken from the penetrating Piston Sampler shows some one-dimensional shortening of the sample (about 1% of its length). In addition, a downward deflection of the horizontal lines in a limited zone very close to the sampler can be recognized.

The photograph of the Delft Sampler shows more deformation. As can be seen, on the outside of the sampler, the clay is heavily pushed downward and radially outward. Inside the device, however, there is only a scarcely visible one-dimensional effect.

Since it is difficult to quantify the small deformations inside the sample, image-processing techniques have been used to make deformation plots out of video shots. The

result for the Delft Sampler is shown in figure 5.9. The measured deformations visualized in this figure can be compared to the calculated deformation pattern as presented in figure 5.4. Both figures show some downward displacements inside the bore mouth without a gradient in horizontal direction. From the experiments (figure 5.9) it can be clearly recognized that the sample deforms more or less elastically inside the bore mouth and recovers at some distance inside the device.

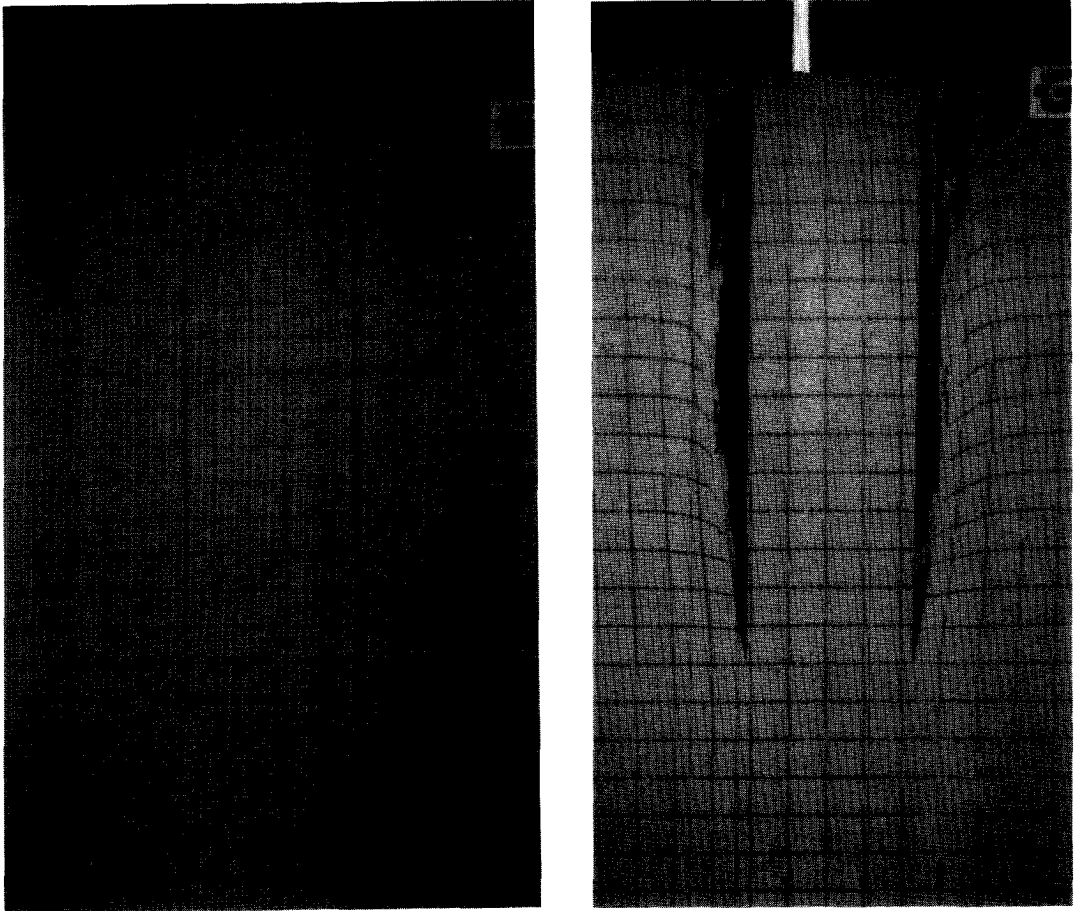


Figure 5.8 Deformation in clay during penetration of Piston Sampler (left) and Delft sampler (right).

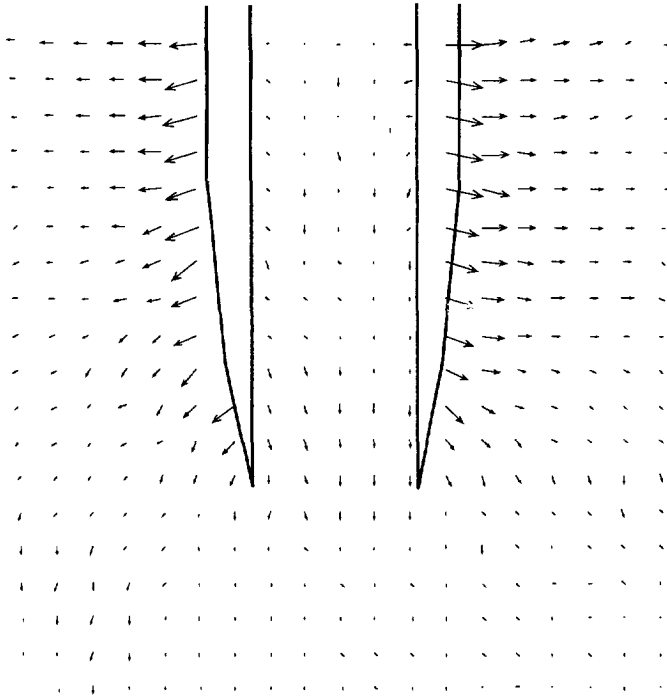


Figure 5.9 Deformation in clay during penetration of Delft Sampler after image processing of video shots.

Stresses

A pore pressure transducer was placed in the clay during the second test series, located at a position in the center-line of the Delft Sampler. The excess pore water pressure measured during sampling is presented in figure 5.10. The isotropic stress in the center-line of the sample as calculated by the numerical model is plotted in the same figure. The shape of the curves shows a good agreement. The most significant conclusions are:

- the excess pore pressure reaches its maximum (compressive) value at some distance (about 0.6 to 0.7 times the sampler radius) underneath the tip of the device.
- after that, the pore pressure in the sample starts to decrease, while after the soil has passed the cutting shoe, an under-pressure remains inside the sample.

The under-pressures which are calculated and measured in the sample appear to agree very well to each other. The maximum (compressive) pore pressure underneath the cutting shoe, following from the numerical model, however, is twice as large as

found by the experiments. Maybe, the combination of the undrained shear strength, the initial stresses and the constitutive model used are responsible for the difference.

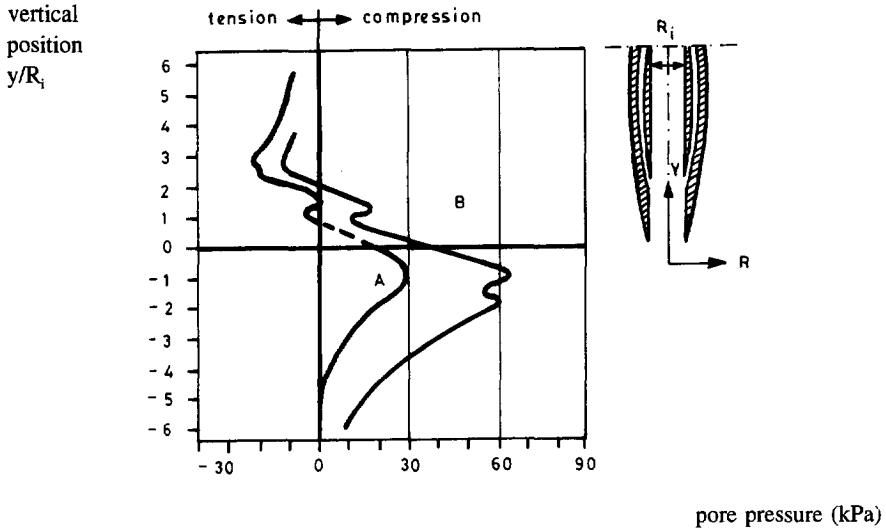


Figure 5.10 Measured (A) and calculated (B) pore pressures in clay during sampling (Delft Sampler).

Budhu and Wu (1992) and Baligh et al. (1987) also present plots for the straining history in the center-line of samplers. They also find the maximum compression at some distance below the bore mouth, and tension higher up inside the sampler (see figure 5.11). This is in agreement with the results of the present study.

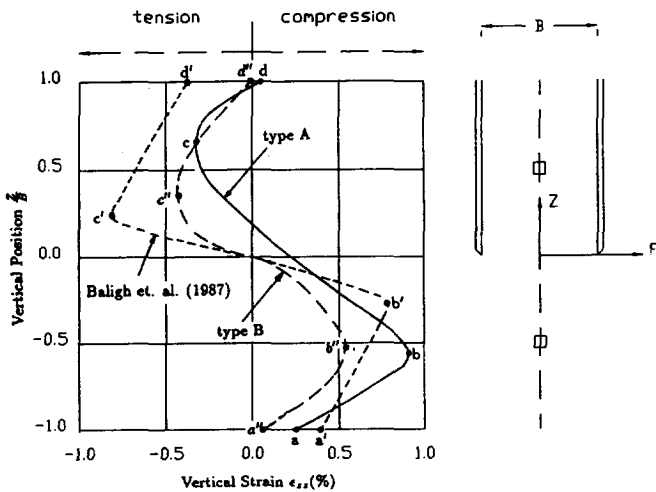


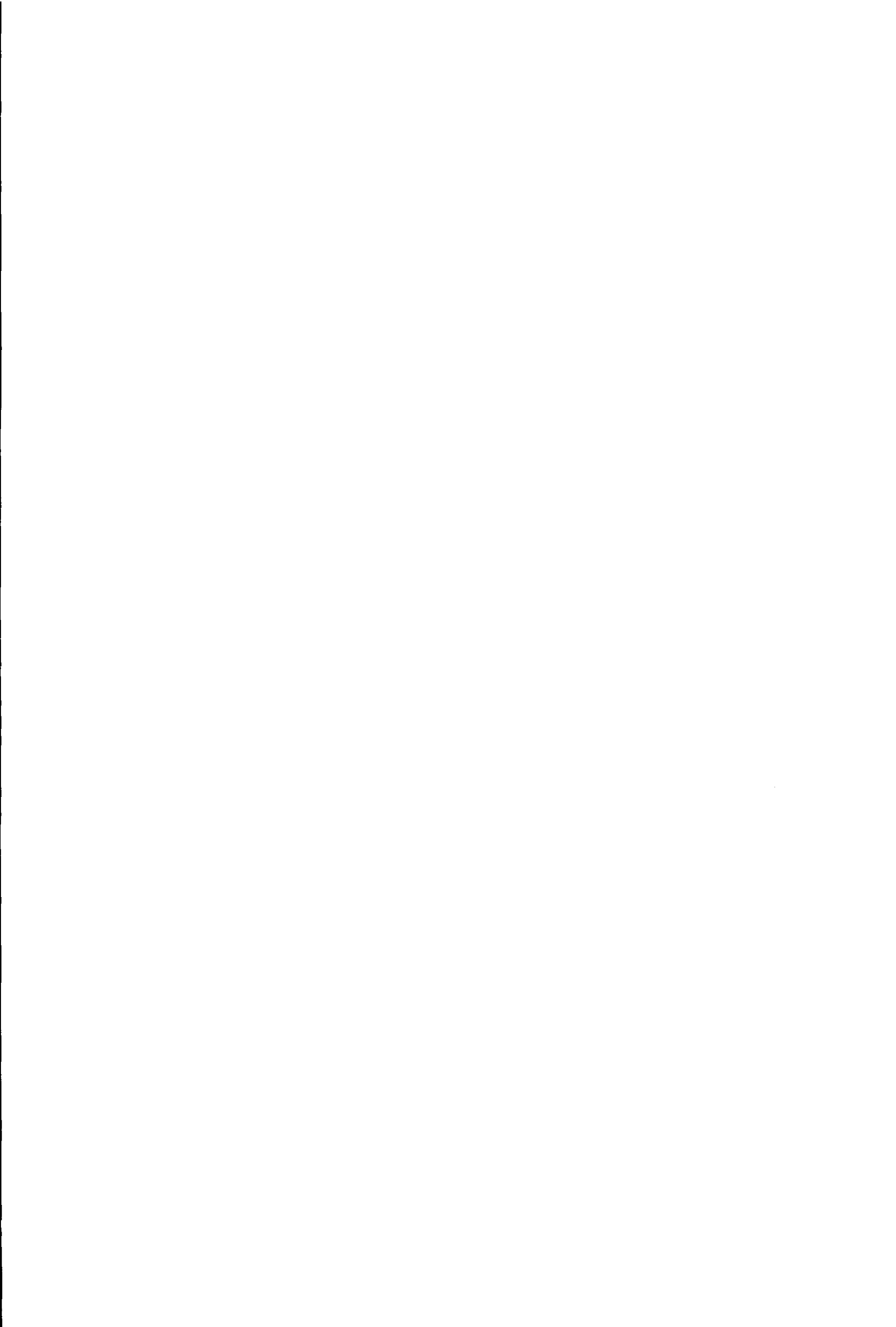
Figure 5.11 Straining history at center-line of sampler (Budhu and Wu, 1992).

5.5 Conclusions

In this chapter it is demonstrated that the numerical model can be used adequately to study the sampling process. The same effects as observed during full scale tests can be reproduced by the numerical model.

Sampling disturbances are mainly caused by the level of interface friction between sampler and soil. The contribution of the area-ratio to the amount of disturbance is negligible, at least for an 11° cutting angle, which is standard for the Delft Sampler.

The present model can be applied as a basic tool to assess the straining history of a sample. However, in order to achieve ultimate judgement about the sample quality fundamental knowledge about the constitutive behaviour of soft soils has to be involved.



References

- Abramowitz, H., Stegun, I.A. (1970).
Handbook of mathematical functions, Dover Publ. Inc., New York.
- Acar, Y.B., Tumay, M.T. (1986).
Strain fields around cones in steady penetration. *J. Geot. Eng.*, Vol. 112, No. 2., pp. 207-213.
- ASTM Designation D3443 (1979).
Standard method for deep quasi-static cone and friction-cone penetration tests in soil.
- Atkinson, J.H., Bransby, P.L. (1978).
The mechanics of soil, an introduction to critical state soil mechanics. McGraw-Hill.
- Atzema, E.H. (1994).
Formability of sheet metal and sandwich laminates. Ph.D. Thesis, University of Twente.
- Baligh, M.M. (1975).
Theory of deep static cone penetration resistance. Publication No. R75-56 of Dept. Civil Eng. of MIT, Cambridge.
- Baligh, M.M. (1985).
The strain path method. Lecture I, MIT Special Summer Course, MIT, Cambridge, MA 02139.
- Baligh, M.M. (1986).
Undrained deep penetration, I, shear stresses. *Geotechnique*, 36, No. 4.
- Baligh, M. M., Azzouz, A. S., Chin, Chung-Tien. (1987).
Disturbances due to "ideal" tube sampling. *J. Geot. Eng.*, Vol. 113, No. 7, July.
- Barends, F.B.J. (1980).
Nonlinearity in groundwater flow. Ph.D. Thesis, Delft University of Technology.
- Bathe, K.J., Ramm, E., Wilson, E.L. (1975).
Finite element formulations for large deformation dynamic analysis. *Int. J. Num. Meth. Eng.*, Vol. 9, pp. 353-386.
- Becker, E. and Burger, W. (1975).
Kontinuumsmechanik. Teubner, Stuttgart.
- Begemann, H.K.S.Ph. (1966).
The new apparatus for taking a continuous sample. *LGM-mededelingen*, 10, No. 4, Delft Geotechnics.
- Been, K., Jefferies, M.G., (1985).
A state parameter for sands. *Geotechnique*, 35, No. 2, pp. 99-112.
- Been, K., Crooks, J.H.A., Becker, D.E., Jefferies, M.G., (1986).
The cone penetration test in sands: part I, state parameter interpretation. *Geotechnique*, 36, No. 2, pp. 239-249.
- Been, K., Jefferies, M.G., Hachey, J. (1991).
The critical state of sand. *Geotechnique*, 41, No. 3, pp. 365-381.
- Bent Hansen, C.E. (1958).
Line ruptures regarded as narrow rupture zones - basic equations based on kinematic considerations. *Proc. Brussels Conf. on earth pressure problems*, Vol. 1, pp. 39-48.
- van den Berg, P., Vermeer, P.A. (1988).
Undrained strength from CPT and finite element computations. *Proc. 6th Int. Conf. on Num. Meth. in Geom.*, Innsbruck, pp. 1095-1100.

- van den Berg, P. (1991a).
Numerical model for cone penetration. Proc. IACMAG 91 Conf., Vol. 3, pp. 1777-1782, Cairns, Australia.
- van den Berg, P., Visschedijk, M.A.T. (1991b).
Numerical analysis of soil-structure interaction. HERON, Vol. 36, No. 2, pp. 73-85.
- van den Berg, P. (1991c).
Effects of surface loading behind earth retaining walls. Proc. 10th ISSMFE Conf., Florence, pp. 767-770.
- van den Berg, P., de Borst, R., Huétink, J. (1992a).
Numerical model for penetration in frictional material. Proc. of 3rd Int. Conf. on Comp. Plast. (COMPLAS III), Barcelona, pp. 971-982.
- van den Berg, P. (1992b).
Soil stresses after installation of driven piles. Proc. 4th Stress-Wave Conf. (F.B.J. Barends, ed), The Hague, pp. 43-49.
- van den Berg, P., Teunissen, J.A.M., Huétink, J. (1994).
Penetration in layered media, an ALE finite element model. Proc. IACMAG 94 Conf., Morgantown, West Virginia. Submitted for publication.
- Besseling, J.F. (1958).
A theory of elastic, plastic and creep deformations of an initially isotropic material. J. of Appl. Mech., 25, pp. 529-536.
- Besseling, J.F. (1985).
Models of metal plasticity; theory and experiment. Plasticity Today, edited by A. Sawczuk and G. Bianchi, Elsevier, pp. 97-113.
- Bolton, M.D. (1986).
The strength and dilatancy of sands. Geotechnique, 36, No. 1, pp. 65-78.
- de Borst, R. (1982).
Calculation of collapse loads using higher order elements. Proc. IUTAM Symp. Deformation and Failure of Granular Materials (eds. P.A. Vermeer and H.J. Luger), pp. 503-513.
- de Borst, R., Vermeer, P.A. (1984).
Possibilities and limitations of finite elements for limit analysis. Geotechnique, 34, No. 2, pp. 199-210.
- de Borst, R. (1987).
Integration of plasticity equations for singular yield functions. Computers and Structures, Vol. 26, No. 5, pp. 823-829.
- de Borst, R., Pankaj, Bicanic, N. (1991).
A note on singularity indicators for Mohr-Coulomb type yield criteria. Comp. and Struct., Vol. 39, No. 1/2, pp. 219-220.
- de Borst, R., Mühlhaus, H.-B. (1992).
Gradient-dependent plasticity: formulation and algorithmic aspects. Int. J. Num. Meth. in Eng., Vol. 35, pp. 521-539.
- de Borst, R., Groen, A.E. (1994).
Some observations on element performance in isochoric and dilatant plastic flow. Submitted for publication.
- Boulon, M. (1989).
Basic features of soil structure interface behaviour. Comp. and Struct., 7, pp. 115-131.
- Budhu, M., Wu, C.S. (1991).
Mechanics of sample disturbances in a soft clay. Proc. IACMAG 91 Conf., Vol. 1, pp. 231-236, Cairns, Australia.

- Budhu, M., Wu, C.S. (1992).
Numerical analysis of sampling disturbances in clay soils. *Int. J. Anal. Num. Meth. Geot.*, Vol. 16, pp. 467-492.
- Buisman, A.S.K. (1935).
De weerstand van paalpunten in zand. *De Ingenieur* 50, pp. 25-35 (in Dutch).
- Caquot, A. (1934).
Equilibre des massive et frottement interne, Paris, Gauthiers-Villars.
- Carter, J.P., Booker, J.R., Yeung, S.K. (1986).
Cavity expansion in cohesive frictional soils. *Geotechnique*, 36, No. 3, pp. 349-353.
- Casagrande, A. (1936).
Characteristics of cohesionless soils affecting the stability of earth fills. *Contributions to Soil Mechanics, 1925-1940*, Boston Society of Civil Eng.
- Castro, G. (1969).
Liquefaction of sand. Ph.D. Thesis, Harvard University.
- Chapman, G.A. (1974).
A calibration chamber for field test equipment. *Proc. ESOPT I, Stockholm*, Vol. 2.2, pp. 59-66.
- Cheng, Y.M., Tsui, Y. (1992).
Limitations to the large strain theory. *Int. J. Num. Meth. in Eng.*, Vol. 33, pp. 101-114.
- Collins, I.F., Pender, M.J., Wang, Yan (1992).
Cavity expansion in sands under drained loading conditions. *Int. J. Num. Anal. Meth. Geom.*, Vol. 16, pp. 3-23.
- Cox, A.D., Eason, G., Hopkins, H.G. (1961).
Axially symmetric plastic deformations in soil. *Transactions, Royal Society of London*, Vol. 254A.
- Cividini, A., Giorda, G. (1988).
A simplified analysis of pile penetration. *Proc. 6th Int. Conf. on Num. Meth. in Geom.*, Innsbruck, pp. 1043-1049.
- Donea, J. (1983).
Arbitrary Lagrangean-Eulerian finite element method. *Comp. Meth. for transient analysis*, Vol. 1, in: *Comp. Meth. in Mech.* (Belytschko and Hughes, eds), North Holland.
- Durgunoglu, H.T., Mitchell, J.K. (1975).
Static penetration resistance of soils. *Proc. ASCE Spec. Conf. on in-situ measurement of soil parameters*, Raleigh.
- van Eekelen, S.J.M. (1991).
Numeriek model voor het steken van grondmonsters, de kwaliteit van het Begemann steekapparaat. M.Sc. Thesis, Delft University of Technology (in Dutch).
- van Eekelen, S.J.M., van den Berg, P. (1994).
Sample disturbance, numerical model and experiments. In: *Geotechnical Engineering, emerging trends in design and practice* (ed. K.R. Saxena), Oxford & IBH Publ. Co., New Delhi, pp. 1-32.
- Gelten, C.J.M., Konter, A.W.A. (1982).
Application of mesh-rezoning in the updated Lagrangean method to metal forming analysis. *Proc. NUMIFORM* (eds. Pittman et al.), Pineridge Press, pp. 511-521.
- Gibson, R.E., Anderson, W.F. (1961).
In situ measurements of soil properties with the pressuremeter. *Civ. Eng. and Public Works Review*, Vol. 56, pp. 615-618.

- Griffiths, D.V. (1982).
Elasto-plastic analysis of deep foundations in cohesive soil. *Int. J. Num. Meth. Geomech.*, No. 6, pp. 211-218.
- Harder, H. (1989).
Numerische modellierung des "Cone Penetration Tests" in wassergesättigten bindigen Böden. *Mitteilungen IGBE, Universität Hannover, Heft 25.*
- Hibbit, H.D., Marcal, P.V., Rice, J.C. (1970).
A finite element formulation for large strain and large displacement. *Int. J. Solids Struct.* 6, pp. 1069-1086.
- Hill, R. (1950).
The mathematical theory of plasticity, Oxford University Press, London.
- Hill, R. (1968).
On constitutive inequalities for simple materials. *J. Mech. Phys. Solids*, Vol. 16, pp. 229-242.
- Houlsby, G.T., Hitchman, R. (1988).
Calibration chamber tests of a cone penetrometer in sand. *Geotechnique*, 38, No. 1, pp. 39-44.
- Huétink, J. (1982).
Analysis of metal forming processes based on a combined Eulerian-Lagrangian finite element formulation. *Proc. Int. Conf. Num. Meth. Industr. Forming Processes*, Pineridge Press, Swansea U.K., pp. 501-509.
- Huétink, J. (1986).
On the simulation of thermomechanical forming processes. Ph.D. Thesis, University of Enschede, The Netherlands.
- Huétink, J., van der Helm, P. (1992).
On Euler-Lagrange finite element formulation in forming and fluid problems. *Proc. NUMIFORM* (eds.: Chenot et al.), Balkema, Rotterdam, pp. 45-54.
- Hughes, T.J.R. (1987).
The finite element method, linear static and dynamic finite element analysis. Prentice Hall Int., Englewood Cliffs, New Jersey.
- Hughes, T.J.R., Liu, W.K., Zimmermann, T.K. (1981).
Lagrangean-Eulerian finite element formulation for incompressible viscous flow. *Comp. Meth. Appl. Mech. Eng.*, Vol. 29, pp. 329-349.
- van Impe, W.F. (1986).
Evaluation of deformation and bearing capacity parameters of foundations from static CPT results. *Proc. 4th NTI Int. Geot. Seminar, Singapore*, pp. 51-70.
- ISSMFE (1977).
Report of subcommittee on standardization of penetration testing in Europe. *Proc. 9th ISSMFE Conf., Tokyo*, Vol. 3, pp. 95-152.
- Janbu, N. (1963).
Soil compressibility as determined by oedometer and triaxial tests. *Proc. ESSMFE, Wiesbaden*, Vol. 1, pp. 19-25.
- Janbu, N., Senneset, K. (1974).
Effective stress interpretation of in situ penetration test. *Proc. ESOPT I, Stockholm*, pp. 181-193.
- Johnson, G.C., Bammann, D.J. (1984).
A discussion of stress rates in finite deformation problems. *Int. J. Solids Structures* Vol. 20, No. 8, pp. 725-737.

- Kiouis, P.D., Voyiadjis, G.Z., Tumay, M.T. (1988).
A large strain theory and its application in the analysis of the cone penetration mechanism. *Int. J. Num. Anal. Meth. in Geom.*, Vol. 12, pp 45-60.
- Ko, H.-Y., Scott, R.F. (1967).
Deformation of sand in shear. *J. Soil Mech. Found. Div., ASCE*, 93, pp. 283-310.
- Koumoto, T., Kaku, K. (1982).
Three-dimensional analysis of static cone penetration into clay. *Proc. ESOPT II*, 2, pp. 635-640, Amsterdam.
- Laboratorium voor Grondmechanica (1979).
Triaxiaalproeven op Oosterschelde zand. Report CO-405334/10 (in Dutch).
- Lade, P.V. (1977).
Elasto-plastic stress-strain theory for cohesionless soil with curved yield surfaces. *J. Solids Struct.*, Vol. 13, pp. 1019-1035.
- Lade, P.V., Nelson, R.B. (1987).
Modelling the elastic behaviour of granular materials. *Int. J. Num. Anal. Meth. in Geom.*, Vol. 11, pp. 521-542.
- van Langen, H. (1991).
Numerical analysis of soil-structure interaction. Ph.D. Thesis, Delft University of Technology, Delft, the Netherlands.
- van Langen, H., Vermeer, P.A. (1991).
Interface elements for sigular plasticity points. *Int. J. Num. Anal. Meth. in Geom.*, Vol. 15, pp. 301-315.
- Levadoux, J.N. (1980).
Pore pressures in clays due to cone penetration. Ph.D. Thesis, MIT, Cambridge.
- Liu, W.K., Belytschko, T, Chang, H. (1986).
An arbitrary Lagrangean-Eulerean finite element method for path dependent materials. *Comp. Meth. Appl. Mech. Eng.*, Vol. 58, pp. 227-245.
- Lorenz, H., Heinz, W.F. (1969).
Changes of density in sands due to loading. *Proc. ISSMFE Conf. Mexico*, pp. 267-273.
- Luger, H.J. (1982a).
Voorspelling en interpretatie van penetratieweerstand in zand. Inpassing en analyse van de ruimte-expansietheorie. Report BAGT 347, CO-256401, Delft Geotechnics (in Dutch).
- Luger, H.J., Lubking, P., Nieuwenhuis, J.D. (1982b).
Aspects of penetrometer tests in clay. *Proc. ESOPT II*, 2, pp. 683-687, Amsterdam.
- Meyerhoff, G.G. (1951).
The ultimate bearing capacity of foundations. *Geotechnique*, Vol. 2, No. 4, pp. 301-332.
- Meyerhoff, G.G. (1961).
The ultimate bearing capacity of wedge-shaped foundations. *Proc. 5th ICSMFE, Paris*, Vol. 2, pp. 103-109.
- Mc.Meeking, R.M., Rice, J.C. (1975).
Finite element formulation for problems of large elasto-plastic deformation. *Int. J. Solids Struct.*, 11, pp. 611-616.
- Mühlhaus, H.-B., Vardoulakis, I. (1987).
The thickness of shear bands in granular materials. *Geotechnique*, 37, pp. 271-283.
- Mühlhaus, H.-B., Aifantis, E.C. (1991).
A variational principle for gradient plasticity. *Int. J. Sol. Struct.*, 28, pp. 845-858.
- Myslivec, Kysela (1978).
The bearing capacity of building foundations, Elsevier, Amsterdam.

- Nagtegaal, J.C., Parks, D.M., Rice, J.C. (1974).
On numerical accurate finite element solutions in the fully plastic range. *Comp. Meth. Appl. Mech. Eng.*, 4, pp. 153-177.
- Nagtegaal, J.C., de Jong, J.E. (1981).
Some computational aspects of elastic-plastic large strain analysis. *Int. J. Num. Meth. Eng.*, Vol. 17, pp. 15-41.
- Needleman, A. (1985).
On finite element formulations for large elastic-plastic deformations. *Comput. Struct.*, Vol. 20, pp. 247-257.
- Nemat-Nasser, S. (1979).
Decomposition of strain measures and their rates in finite deformation elasto-plasticity. *Int. J. Solids Struct.*, 15, pp. 155-166.
- Pastor, M., Zienkiewicz, O.C., Chan, A.H.C. (1990).
Generalized plasticity and the modelling of soil behaviour. *Int. J. Num. Anal. Meth. in Geom.*, Vol. 14, pp. 151-190.
- Prandtl, L. (1921).
Über die Härte plastischer Körper. *Nachrichten der Gesellschaft der Wissenschaften zu Göttingen*.
- Reynolds, O. (1885).
On the dilatancy of media composed of rigid particles in contact. *Phil. Mag. 5th Series*, 20, pp. 469.
- Robertson, P.K., Campanella, R.G. (1986).
Guidelines for use and interpretation of the electric cone penetration test. Hogentogler & Company, Inc., Manual, 3rd Edition.
- Roscoe, K.H., Scofield, A.N., Wroth, C.P. (1958).
On the yielding of soils. *Geotechnique*, 8, No. 1, pp. 22-53.
- Rowe, P.W. (1962).
The stress-dilatancy relation for static equilibrium of an assembly of particles in contact. *Proc. Royal Soc.*, Vol. 269, pp. 500-527.
- Rowe, P.W. (1971).
Theoretical meaning and observed values of deformation parameters of particles in contact. *Proc. Roscoe Memorial Symp. on stress-strain behaviour of soils*, Cambridge, pp. 143-194.
- de Ruiter, J., Beringen, F.L. (1979).
Pile foundations for large North Sea structures. *Marine Geotechnology*, Vol. 3, No. 3, pp. 267-314.
- de Ruiter, J. (1982).
The static cone penetration test - state of the art. *Proc. ESOPT II*, 2, pp. 389-405, Amsterdam.
- Sanglerat, G. (1972).
The penetrometer and soil exploration. Elsevier Scientific Publishing Company, Amsterdam-Oxford-New York.
- Satyanarayana, B., Garg, R.K. (1980).
Bearing capacity of footings on layered $c-\phi$ soils. *ASCE Journal of Geot. Eng. Div. 106, GT7*, No. SM2, pp. 83-99.
- Schellekens, J.C.J. (1992).
Computational strategies for composite structures. Ph.D. Thesis, Delft University of Technology.

- Schmertmann, J.H. (1978).
Guidelines for cone penetration test, performance and design. Federal Highway Adm. Report FHWA-TS-78-209, Washington.
- Schnaid, F., Housby, G.T. (1992).
Measurement of the properties of sand in a calibration chamber by the cone pressuremeter test. *Geotechnique*, 42, No. 4, pp. 587-601.
- SCW (1978).
Various properties of natural sands for Netherlands Highway Engineering. Study Centre for Road Construction, the Netherlands.
- Simo, J.C., Meschke, G. (1992).
New algorithms for multiplicative plasticity that preserve the classical return mappings: applications to soil mechanics. Proc. of 3rd Int. Conf. on Comp. Plast. (COMPLAS III), Barcelona, pp. 765-790.
- Sloan, S.W., Randolph, W.F. (1982).
Numerical prediction of collapse loads using finite elements methods. *Int. J. Num. Anal. Meth. Geom.*, 6, pp. 47-76.
- Sluys, L.J. (1992).
Wave propagation, localization and dispersion in softening solids. Ph.D. Thesis, Delft University of Technology.
- Stroud, M.A. (1971).
The behaviour of sand at low stress levels in the simple shear apparatus. Ph.D. Thesis, University of Cambridge, U.K.
- Szabo, L., Balla, M. (1989).
Comparison of some stress rates. *Int. J. Solids Struct.* Vol. 25, No. 3, pp. 279-297.
- Smith, I.M., Chow, Y.K. (1987).
Three-dimensional analysis of pile drivability.
- Smits, F.P. (1977).
Sonderingen in zand - een theoretische basis voor analyse van de conusweerstand. FUGRO Sondeersymposium, 5 oktober 1977, pp. 31-42 (in Dutch).
- Stolle, D.F.E., Schad, H. (1992).
An updated reference configuration formulation for large-strain problems. *Int. J. Num. Anal. Meth. Geom.*, Vol. 16, pp. 295-306.
- Teh, C.I., Housby, G.T. (1991).
An analytical study of the cone penetration test in clay. *Geotechnique*, 41, No. 1, pp. 17-34.
- Teunissen, J.A.M. (1982).
Mechanics of a fluid-gas mixture in a porous medium. *Mech. Mater.*, 1, pp. 229-237.
- Teunissen, J.A.M. (1991).
Analysis of plasticity and non-coaxiality in geomaterials, Ph.D. Thesis, Delft University of Technology, The Netherlands.
- Treadwell, D.D. (1975).
The influence of gravity, prestress, compressibility and layering on soil resistance to static penetration. Ph.D. Thesis. Berkeley.
- Vermeer, P.A. (1978).
A double hardening model for sand. *Geotechnique*, 28, No. 4, pp. 413-433.
- Vermeer, P.A., van den Berg, P. (1988).
Analysis of CPT for undrained clays. Proc. First Int. Symposium on Penetration Testing, Orlando, USA, March 20-24.

- Vesic, A.S. (1967).
 Ultimate loads and settlements of deep foundations in sand. In: Proc. of symposium on bearing capacity and settlement of foundations, Duke University, pp. 53-68.
- Vesic, A.S. (1972).
 Expansion of cavities in infinite soil mass. *Int. J. Soil Mech. Found. Div. ASCE*, 98, pp. 265-290.
- Vesic, A.S. (1975).
 Principles of pile design. Lecture series on deep foundations. MIT, Cambridge, 46 pp.
- Weismanis, A. (1974).
 Laboratory investigations of electrical friction-cone penetrometers in sand. *Proc. ESOPT I*, Stockholm, Vol. 2.2, pp. 407-420.
- Whittle, A.J. (1992).
 Constitutive modelling for deep penetration problems in clay. *Proc. of 3rd Int. Conf. on Comp. Plast. (COMPLAS III)*, Barcelona, pp. 883-894.
- Willson, S.M. (1985).
 Finite element analysis of piles and penetrometers. Ph.D. Thesis, University of Manchester, U.K.
- Wood, D.M. (1990).
 Soil behaviour and critical state soil mechanics. Cambridge University Press.
- Yu, H.S., Houlsby, G.T. (1991).
 Finite cavity expansion in dilatant soils: loading analysis. *Geotechnique*, 41, No. 2, pp. 173-183.
- Zienkiewicz, O.C., Paul, D.K., Chan, A.H.C. (1988).
 Unconditionally stable staggered solution procedure for soil - pore fluid interaction problems. *Int. J. Num. Meth. Eng.*, 26, pp. 1039-1055.
- Zytynski, M., Randolph, M.F., Nova, R., Wroth, C.P. (1978).
 On modelling the unloading-reloading behaviour of soils. *Int. J. Num. Anal. Meth. in Geom.*, Vol. 2, pp. 87-94.

List of symbols

a	adhesion
a	dummy parameter
b	width
b	dummy parameter
c	cohesion
c_u	undrained cohesion
d	rate of deformation
d	distance
e	void ratio
f	yield function
f_s	skin friction
f	function
f_r	friction ratio
g	plastic potential function
h	height
h	hardening modulus
h	indicator whether one or two yield functions are active
h	hydraulic head
k	permeability
k	discrete force vector
k	parameter Drucker-Prager model
l	length
m	dummy parameter
n	porosity
n	dummy parameter
p_a	atmospheric pressure
p	bearing capacity of deep foundation
p	isotropic stress
p	pore water pressure
q_c	cone resistance
q	deviatoric stress
r	radius
s	shape factor
s	deviatoric stress
t	time
t	traction
u	elongation
u	pore water pressure
u	displacement
v	velocity
w	water content

x	position vector in current state
x	direction
y	direction
z	depth
z	direction
A	cross section
B	width of foundation
B	strain operator
D_r	relative density
D	constitutive tensor
D	(cone) diameter
E	Youngs' modulus
E	elasticity tensor
F	deformation gradient
F	force
G	shear modulus
H	history of plastic deformation
I_r	rigidity index
I_r	reduced rigidity index
I	unit tensor
I_1	first invariant of stress tensor
J	determinant of gradient of deformation
J_2	second invariant of stress tensor
K	modulus number non-linear elasticity
K	bulk modulus
K_0	lateral pressure ratio
L	strain operator
M	modulus number non-linear elasticity
M	dummy tensor
N_q	bearing capacity factor
N_c	cone factor
N_p	partial cone factor
N	dummy tensor
Q	rate of discharge
R	radius
R	ratio "strength interface - strength continuum"
S	boundary surface
S	stiffness matrix
S	surface force
V	volume
W	power
Y	plasticity tensor

α	adhesion
α	parameter Drucker-Prager model
α	angle
β	parameter Drucker-Prager model
β	angle
β	parameter non-linear elastic model
γ	volumetric weight
γ	Green-Lagrange strain
δ	Kronecker delta tensor
δ	interface friction angle
δ	(displacement) increment
ε	Eulerian strain
λ	plastic intensity
λ_{ss}	slope of critical state line
μ	dummy parameter
ν	Poissons' ratio
ξ	position vector in reference state
ξ	hardening/softening parameter
ρ	density
σ	Cauchy stress
τ	2nd Piola Kirchhoff stress
τ	shear stress
ϕ	friction angle
ψ	shape function
ψ	dilatancy angle
ω	rate of rotation
Ψ	state parameter
Δ	increment
Δ	volume change
Λ	parameter of critical state model

subscripts

c	compression
conv	convected
cr	critical
cv	constant volume
d	drained
dr	dry
e	extension
el	elastic
h	horizontal
i	initial
i	position number

max	maximum
min	minimum
n	new
n	normal
o	initial
o	old
p	plastic
p	pores
pl	plastic
s	shear
u	ultimate
u	undrained
v	vertical
v	volume
w	water

superscripts

'	effective
-1	inverse
c	constitutive
el	elastic
m	material
N	nodal point
N	new
n	nodal point
o	objective
o	old
pl	plastic
T	transpose
t	trial
w	water

Summary

Penetration of rigid devices into soil is a large deformation process. A soil particle initially located at a position in the undisturbed soil mass is pushed aside to make room for the device, resulting into a horizontal stress build-up around the apparatus. The finite element models commonly used to analyse soil penetration problems are Lagrangean type models. In this type of models the same material remains inside the same element throughout the complete calculation. The application of such models indicates that the total vertical displacement of the device, which can be simulated, is limited and, therefore, a steady state stress distribution around the device cannot be predicted accurately. During continued penetration the elements distort too much and divergency of the iteration procedure occurs. To overcome these problems a Eulerean approach is followed in this thesis. In contrast to a Lagrangean approach, the material is not coupled to the elements. The finite element discretization including the penetrating device is fixed in space and the soil flows through the fixed mesh. Using this kind of models the length of penetration is unlimited.

The finite element program DIEKA is extended in the sense that penetration of rigid devices into frictional material can be simulated adequately. Therefore non-associated Drucker-Prager and Mohr-Coulomb type plasticity models were implemented. Since during penetration very large shear strains occur, it is necessary to introduce a hardening/softening relation. A strain independent value for the dilatancy angle would lead to an unrealistic build-up of stresses. For the definition of this relation the critical density theory is employed, which states that during enlarged shearing the density of the material tends to go to a constant value. This implies that the dilatancy angle tends to zero, while the friction angle goes to the friction angle at constant volume deformation.

The subsoil normally consists of layered deposits. Therefore, in order to simulate real soil penetration, it is essential to introduce different soil layers into the model. A method is described by which boundaries between two layers can be dealt with in a Eulerean context. The displacement path of a material particle including its constitutive behaviour can be followed in a fixed finite element mesh. An example is given concerning a pile penetrating out of one layer into another layer. It is shown that under the tip of the pile soil coming from the upper layer penetrates with the pile into the deeper layer.

The model can be used to analyse a large number of different penetrating devices. First, the attention is focussed on the cone penetration test in homogeneous material. Since the penetration process in clay can be regarded as fully undrained, the behaviour is assumed to be purely cohesive. It is concluded that the cone resistance in clay is highly determined by the undrained shear strength. The influence of the amount of interface friction, the lateral pressure ratio and the stiffness are limited to

less than 25%. The cone resistance in frictional material, however, depends on a lot of parameters: stiffness, friction and dilatancy, interface friction, initial vertical stress and, to a somewhat smaller extent, the lateral pressure ratio. At least one additional measurement, especially focussed on the stiffness of the material, is needed to reduce the uncertainties in the translation from cone results to mechanical properties of the soil. For that purpose, for instance, penetration tests can be performed using cones with different shapes. The cone pressuremeter, too, is a powerful tool to get information about the stiffness.

An alternative way to derive an estimation of the soil stiffness is to analyse the gradient of the cone resistance with depth when a cone passes from one layer to another layer. This is demonstrated in the final section of the chapter on the cone penetration test. Numerical and experimental results are shown for two particular cases, referred to as "clay on sand" and "sand on clay". The results indicate that a cone in frictional material senses a soft layer at a distance of 4-5D. And, to reach the full steady state cone resistance in a frictional layer, about 6-7D penetration into that layer is needed. These values, however, depend on the stiffness ratio between the layers. The results imply that the thickness of interbedded stiff frictional deposits to ensure full tip resistance is at least 12D or 40-50 cm. For undrained clay layers, however, the minimum thickness is considerably lower. Both the numerical model and the experiments indicate that a thickness of only a few diameters (10-15 cm) is enough to generate full resistance.

The final chapter deals with sample disturbance in clayey soils. The numerical model is applied to analyse soil deformation underneath, inside and around a penetrating Delft Continuous Sampler and a thin-walled Piston Sampler. The results are compared to results of full scale experiments carried out under controlled conditions in the laboratory. Concluding it can be said that the area ratio of the Delft Sampler, which is relatively large when compared to the Piston Sampler, hardly influences the quality of the sample. The interface friction between soil and sampler is highly responsible for the quality.

Samenvatting

Het wegdrücken van starre lichamen in de grond gaat gepaard met grote lokale vervormingen. Een gronddeeltje, dat zich eerst ergens in de onverstoorde ondergrond bevindt, wordt opzij gedrukt om ruimte te maken voor het penetrerende lichaam. De eindige-elementen modellen, die gewoonlijk gebruikt worden om dit type problemen op te lossen, zijn gebaseerd op een Lagrangeaanse aanpak. Dit houdt in, dat hetzelfde materiaal zich gedurende de gehele berekening in hetzelfde element bevindt. De toepassing van dit type modellen laat echter zien dat bij deze aanpak de penetratieafstand beperkt is. De eindige-elementen vervormen te veel en het numerieke iteratie proces gaat divergeren. Om deze problemen te voorkomen, wordt in dit proefschrift gebruik gemaakt van een Eulerse aanpak. In tegenstelling tot de Lagrangeaanse aanpak is het materiaal niet meer gekoppeld aan het element. De eindige-elementen schematisering inclusief het penetrerende lichaam is gefixeerd in de ruimte en de grond stroomt als het ware door de elementen heen. Hierdoor is de penetratielengte in feite onbeperkt geworden.

Het eindige-elementen programma DIEKA is uitgebreid met als doel de simulatie van penetratie in wrijvingsmaterialen mogelijk te maken. Daartoe zijn niet-geassocieerde plasticiteits-modellen (Drucker-Prager en Mohr-Coulomb) geïmplementeerd. Omdat tijdens het penetratieproces lokaal zeer grote schuifvervormingen optreden, is het voor dit type problemen noodzakelijk een vorm van hardening/softening te introduceren. Een dilatantiehoek, die onafhankelijk is van de grootte van de rek, zou leiden tot een sterke overschatting van de spanningsopbouw. Bij de definitie van de hardening/softening regel is uitgegaan van de "kritieke dichtheid" theorie, die inhoudt dat bij toenemende schuifvervorming de dichtheid van het materiaal naar een constante waarde gaat. In het model betekent dit dat de dilatantiehoek naar nul gaat en de wrijvingshoek naar de "wrijvingshoek bij constant volume".

Over het algemeen heeft de ondergrond een gelaagde opbouw. Om de praktische waarde van het model te vergroten is het daarom essentieel, dat ook verschillende grondlagen kunnen worden gemodelleerd. Een methode wordt beschreven waarmee een scheiding tussen twee lagen behandeld kan worden in een Eulerse context. Daartoe wordt de afgelegde weg van een gronddeeltje met het bijbehorende constitutieve gedrag gevolgd in de eindige-elementen verdeling, die gefixeerd is in de ruimte. Een voorbeeld wordt gegeven van het penetreren van een paal uit de ene laag in een volgende laag, waarbij onder de paalpunt grond van een hoger gelegen laag wordt meegenomen in de diepere laag.

Met het model kan het penetreren van willekeurige starre lichamen worden gesimuleerd. Eerst wordt aandacht besteed aan de sondering in homogeen materiaal. Omdat penetreren in klei beschouwd kan worden als een ongedraineerd proces, is puur cohesief materiaalgedrag verondersteld. Geconcludeerd wordt dat de conusweerstand

in klei voornamelijk bepaald wordt door de ongedraineerde schuifsterkte. De invloed van de mate van wrijving tussen de conus en de grond, de verhouding tussen de initiële horizontale en verticale spanning in de grond en de stijfheid van de grond spelen geen grote rol van betekenis. De conusweerstand in zand is echter afhankelijk van een groot aantal parameters: de stijfheid, de sterkte (wrijvingshoek en dilatatiehoek), de wrijving tussen conus en grond, de initiële verticale spanning en, in mindere mate, de verhouding tussen de horizontale en verticale spanning. Geconcludeerd wordt dat tenminste één extra meting, speciaal gericht op de stijfheid van de grond, nodig is om de onzekerheid bij de vertaalslag van gemeten conuswaarden naar mechanische eigenschappen van de grond te reduceren. Daartoe zouden bijvoorbeeld conussen met verschillende geometriën kunnen worden weggedrukt. Ook de conus-pressuremeter is in staat inzicht te verschaffen in de stijfheid van de grond.

Een andere manier om een idee te krijgen van de stijfheid van een grondlaag is na te gaan wat de toename van de conusweerstand over de diepte is ter plaatse van een laagovergang. De onderbouwing voor een dergelijke aanpak wordt gegeven in de laatste paragraaf van hoofdstuk 4. Numerieke en experimentele resultaten worden gegeven voor twee specifieke situaties, namelijk "klei op zand" en "zand op klei". De resultaten geven aan dat een conus in zand een slappe laag voelt op een afstand van 4-5D. Verder is een afstand van ongeveer 6-7D nodig, voordat in een zandlaag de bij die laag behorende conusweerstand volledig is opgebouwd. Deze waarden blijken overigens afhankelijk te zijn van de stijfheidsverhouding tussen de beide lagen. De resultaten geven aan dat de dikte van een tussen-zandlaag, die minimaal nodig is om de gehele conusweerstand op te bouwen, 12D of 40-50 cm bedraagt. Voor ongedraineerde klei is deze dikte echter veel kleiner. Zowel de resultaten van de berekeningen als van de experimenten tonen aan dat een dikte van 10-15 cm voldoende is.

Het laatste hoofdstuk gaat over monsterverstoring in klei-achtige gronden. Het Eulerse eindige-elementen model is gebruikt om de vervormingen, die onder, in en rond een monstersteekapparaat optreden te kwantificeren. Een vergelijking is gemaakt tussen de vervormingen, die plaatsvinden bij het steken van een monster met het Delft Continu Steekapparaat en de internationaal bekende Piston Sampler. De berekeningsresultaten worden vergeleken met resultaten van experimenten, die zijn uitgevoerd in het laboratorium onder gecontroleerde omstandigheden. Aangetoond wordt, dat de dikte van het steekapparaat, die bij het Delft Steekapparaat relatief groot is, nauwelijks invloed heeft op de kwaliteit van het gestoken monster. De wrijving tussen de grond en het steekapparaat speelt hierbij een veel grotere rol.

Curriculum Vitae

Peter van den Berg werd op 12 augustus 1961 in Gouda geboren. Van 1973 tot 1979 volgde hij de gymnasium- β opleiding van het Chr. Lyceum-Havo te Gouda. Van 1979 tot 1987 studeerde hij Civiele Techniek aan de Technische Universiteit te Delft. In februari 1987 behaalde hij het diploma binnen de vakgroep Constructieleer. Het afstudeerwerk, dat tussen 1984 en 1986 in dienst van het toenmalige TNO-IBBC werd uitgevoerd, lag op het gebied van de numerieke simulatie van kruip en scheurvorming van beton. Aan dit werk is de studieprijz van de Betonvereniging toegekend. Sinds november 1985 is hij werkzaam bij Grondmechanica Delft. Zijn werkgebied omvat de ontwikkeling, validatie en toepassing van geavanceerde geotechnische rekenmodellen, speciaal op het gebied van grond-constructie-interactie, grote vervormingen en drie-dimensionale analyses. De laatste jaren is hij vanuit de hoofdafdeling Ontwikkeling aangewezen als wetenschappelijk begeleider van ontwikkelingswerk op het gebied van geotechnische rekenmodellen. Verder is hij secretaris van CUR-onderzoekcommissie C 94 "drie-dimensionale effecten bij ondergrondse constructies", lid van CUR-COB commissie C 100 "praktijkonderzoek boortunnels", lid van het bestuur van de Stichting DIANA, lid van verschillende STW gebruikerscommissies en afstudeercommissies vanuit zowel de Technische Universiteit Delft als die van Twente, en werkt hij samen met Universiteiten in de Verenigde Staten en Japan. Hij schreef circa 30 wetenschappelijke publicaties.